12-2010

MOLECULAR PHYSICS OF ELECTRICAL DOUBLE LAYERS IN ELECTROCHEMICAL CAPACITORS

Guang Feng
Clemson University, gfeng@clemson.edu

MOLECULAR PHYSICS OF ELECTRICAL DOUBLE LAYERS IN ELECTROCHEMICAL CAPACITORS

A Dissertation
Presented to
the Graduate School of
Clemson University

In Partial Fulfillment
of the Requirements for the Degree
Doctor of Philosophy
Mechanical Engineering

---

by
Guang Feng
December 2010

Accepted by:
Dr. Rui Qiao, Committee Chair
Dr. Bruce Z. Gao
Dr. Richard S. Miller
Dr. John R. Saylor

ABSTRACT

At present, electrochemical capacitors (ECs) are emerging as a novel type of energy storage devices and have attracted remarkable attention, due to their key characteristics, such as high power density and excellent durability. However, the moderate energy density of ECs restricts their widespread deployment in everyday technology. To surmount this limitation, four strategies are adopted: (1) to reduce the total system mass, (2) to increase the specific surface area of electrodes, (3) to enhance normalized capacitance, and (4) to expand the range of potentials applied on electrodes. The implementation of these approaches critically relies on the fundamental understanding of physical processes underlying the energy storage mechanisms hinging on the electrical double layers (EDLs) in ECs.

In this dissertation, to gain the fundamentals of EDLs in ECs, based on the strategies described above, we studied the structure, capacitance, and dynamics of EDLs in different electrolytes near electrodes featuring different pores using atomistic simulations. The pores of electrodes are categorized into macropores, mesopores, and micropores, following the decreasing order of pore size. The chosen electrolytes fall into aqueous electrolytes, organic electrolytes, and ionic liquids (ILs), listed by the increasing order of their decomposition voltages.

For the aqueous electrolytes, we explored the water and ion distributions inside electrified micropores (< 2nm) using molecular dynamics (MD) simulations. The results showed that the ion distribution differs qualitatively from that described by classical EDL theories. Based on such exceptional phenomenon, a new sandwich capacitance model

was developed to describe the EDLs inside micropores, which is capable of predicting the sharp increase of capacitance that has been experimentally observed in micropores.

For the organic electrolytes, we examined the ion solvation and the EDL structure, capacitance, and dynamics in the electrolyte of tetraethylammonium tetrafluoroborate ($TEABF_4$) in the aprotic solvent of acetonitrile (ACN). Firstly, the solvation of TEA^+ and BF_4^- ions is found to be much weaker than that of small inorganic ions. This characteristic accounts for the rich structure of EDLs near the electrodes. In particular, near charged electrodes, the ion distribution cannot be explained by the traditional EDL models. Secondly, the computed capacitances of EDLs agree well with those inferred from experimental measurements. Finally, we probed the dynamics of EDLs in organic electrolytes by analyzing the rotational dynamics of solvent and the self diffusion coefficients of ion/solvent.

For the ILs, we performed the MD simulations of EDLs at the interface between an IL of 1-butyl-3-methylimidazolium nitrate ([BMIM][NO_3]) and planar electrodes. The results revealed that the structure of the EDL is significantly affected by the liquid nature of the IL, the short-range ion−electrode and ion−ion interactions, and the charge delocalization of ions. We showed that the differential capacitance is a quantitative measure of the response of the EDL structure to a change of electrode surface charge density, and the concave-shaped capacitance−potential ($C-V$) curve is in good agreement with that in the literature.

To further acquire the theoretical understanding of EDLs in ILs, we investigated the effects of ion size and electrode curvature on the EDLs in ILs of 1-butyl-3-

methylimidazolium chloride ([BMIM][Cl]) and 1-butyl-3-methylimidazolium hexafluorophosphate ([BMIM][PF_6]). The results indicated that the ion size considerably affects the ion distribution and orientational structure of EDLs, and the EDL capacitances follow a certain order of the ion size. It was also found that the EDL capacitance increases as the electrode curvature increases. Based on the insights gained from the EDL structure and capacitance, a "Multiple Ion Layers with Overscreening" (MILO) model was proposed for EDLs in ILs. The capacitance predicted by the MILO model agrees well with that computed from the MD simulation.

DEDICATION

I would like to dedicate my dissertation to my wife, Dr. Jingai Shao. Her love, support, and encouragement allowed me to focus on my research and accomplish this work. I also would like to dedicate this dissertation to my dear father and mother and my sisters, and express my deepest gratitude for their loves and devotions which supported me to overcome challenges and accomplish my dreams in my life.

ACKNOWLEDGMENTS

I would like to express my gratitude first and foremost to my advisor Prof. Rui Qiao for his supervision, guidance, advice, and encouragement during my doctoral study. His faith of “to be the best” inspired me to be the best that I can be. Getting hands-on training and learning from him for four years, I obtained some achievements not only in the scientific research but also in how to behave decently and efficiently with a good attitude, which would be impossible without his patience, understanding, and support.

I would like to sincerely acknowledge the other members of my advisory committee, Prof. Bruce Z. Gao, Prof. Richard S. Miller, and Prof. John R. Saylor, for their advice on my research and for their time and efforts to my proposal, dissertation, and defenses. I would like to thank Prof. Steven J. Stuart for his helping me understand the fundamentals of atomistic/quantum calculations. I would like to thank Prof. Lin Ma for his good attitude of “due”, Prof. Gang Li for his training of finite element analysis and Prof. David Zumbrunnen for his teaching me how to have a good organization on solving problems.

I would like to genuinely thank our collaborators in Oak Ridge National Laboratory, Dr. Jingsong Huang, Dr. Bobby G. Sumpter, and Dr. Vincent Meunier, for their advice and help. I did and do benefit a lot from the communication and cooperation with them.

I would like to greatly thank my research group members, Ping He, Clint William Cagle, Peng Wu, and Ying Liu, for their very friendly help and the time we spent together on doing research and having a happy daily life. Especially, I appreciate Ping He

for his efforts to help me develop my computer skills. I would like to thank Jian Cai, Jie Kou, Junjie Zhu, and Yan Zhao, for their useful communications on the research.

I would like to acknowledge the researchers, David van der Spoel, Erik Lindahl, Berk Hess, etc., who developed the molecular dynamics package Gromacs. They made such great and powerful package as an open resource and gave guidance of how to use it. Without their kind share, it would be very hard for me to obtain all the results in this dissertation. I would like to acknowledge the Clemson-CCIT office providing computer time on the Palmetto Cluster.

TABLE OF CONTENTS

Page

TITLE PAGE i

ABSTRACT ii

DEDICATION v

ACKNOWLEDGMENTS vi

LIST OF TABLES x

LIST OF FIGURES xi

CHAPTER

1. INTRODUCTION 1

2. PRIOR STUDIES OF EDLS 11

    2.1 Theoretical Models of EDLs 11
    2.2 EDLs in Aqueous Electrolytes 14
    2.3 EDLs in Organic Electrolytes 16
    2.4 EDLs in Ionic Liquids 17

3. METHOD AND METHODOLOGY 22

    3.1 Molecular Dynamics Simulation 22
    3.2 Data Analysis 25

4. EDLS IN AQUEOUS ELECTROLYTES FILLED MICROPORES 29

    4.1 MD Simulation Setup 29
    4.2 Water/Ion Distributions inside Micropores 31
    4.3 Physical Origins of the Water/Ion Distributions 33
    4.4 The Sandwich Model 43
    4.5 Conclusions 47

Table of Contents (continued) Page

5. EDLS IN ORGANIC ELECTROLYTES NEAR OPEN ELECTRODES 49

5.1 Simulation Setup 49
5.2 Ion Solvation in Bulk Organic Solvents 53
5.3 Structure and Capacitance of EDLs 57
5.4 Dynamics of EDLs 75
5.5 Conclusions 81

6. EDLS IN IONIC LIQUIDS NEAR PLANAR ELECTRODES 84

6.1 MD Simulation Setup 84
6.2 EDL Microstructure 85
6.3 EDL Capacitance 93
6.4 Conclusions 110

7. EFFECTS OF ION SIZE AND ELECTRODE CURVATURE ON EDLS IN IONIC LIQUIDS 112

7.1 Simulation System and Methods 112
7.2 Ion Distribution at EDLs 116
7.3 Ion Size and Curvature Effects on EDL Capacitance 123
7.4 A New Capacitance Model for EDLs in ILs 130
7.5 Conclusions 136

8. CONCLUSIONS 138

REFERENCES AND NOTES 143

LIST OF TABLES

Table Page

4.1 Properties of K^+ ion located at different positions inside slit pores and the properties of their hydration water molecules. 39

5.1 Self diffusion coefficients of molecules (in unit of 10^{-9} m^2/s) in the region of 0.56 nm from the electrode. 79

7.1 The EDL thickness based on different choices described in the text and comparison of curvature-induced capacitance enhancement predicted by Equation 7.6 and MD simulations..... 128

7.2 Key parameters of the MILO model measured in MD simulations and comparison of curvature-induced capacitance enhancement predicted by Equation 7.11 and MD simulations. 135

LIST OF FIGURES

Figure Page

1.1 Ragone plot for basic electrical energy storage devices. The time for charging-discharging is also indicated on the plot. 2

1.2 A schematic of an EC. Reproduced from Ref. [13]. 5

1.3 Different types of pores on the electrode: (a) macropore, (b) mesopore, (c) slit-shaped micropore, (d) cylindrical micropore, and (e) cylindrical pore with ourside electrolytes. (a), (b), (d) and (e) are reproduced from Ref. [15]. 6

2.1 Models of the EDLs: (a) Helmholtz model, (b) Gouy-Chapman model, (c) Gouy-Stern model, and (d) general representation of EDL. Reproduced from Ref. [2]. 12

3.1 Simulations as a bridge between (a) microscopic and macroscopic; (b) theory and experiment. Reproduced from Ref. [66]. 24

3.2 Results from MD simulations of NaCl in water near a neutral electrode: (a) number density, where the water number density has been divided by a factor of 30, (b) the total space charge density, and (c) potential distribution. 26

4.1 A snapshot of MD simulation. The yellow, red, and blue colors represent the electrode, ions and the solvent molecults, respectively. Z=0 corresponds to the lower electrode. 30

4.2 (a) Concentration profiles of water and K^+ ions inside slit pores with various widths. For clarity, the water concentration has been divided by a factor of 30. The concentric circles denote the size of bare and hydrated K^+ ions. The hemi-circles in the leftmost figure denote the van der Waals radius of the wall atom and the dashed lines denote the effective boundary of the lower wall. (b) Hydration number of K^+ ions across slit pores with various widths. All slit walls have the same surface charge density of $\sigma = -0.055 C/m^2$ 32

List of Figures (Continued)

Figure Page

4.3 Schematic diagrams of the five factors, as described in the text, governing the distributions of the K^+ counter-ions in electrified slit-shaped micropores: a) the long-range electrostatic ion-ion repulsion which drives ions toward the slit walls (factor 1) and the non-electrostatic ion-slit wall attraction (factor 2), indicated by the red and green double-headed arrows, respectively (color codes also applicable in the following); b) the hydration of ions (factor 3), which drives ions toward positions to maximize their interactions with the hydration water molecules (the blue dashed circle indicates the primary hydration shell of one ion; compared to the ions in the slit center, the ion near the slit wall has smaller number of hydration water molecules); c) the interaction between an ion's hydration water molecules with their surrounding water molecules (factor 4); and d) entropic effects that drive the ordered distribution shown on the left toward a uniform/disordered distribution on the right (factor 5). 35

4.4 Variation of counter-ion (K^+ ion) concentration scaled by the slit wall charge density (cion/|σ|) in 9.36 Å-wide slits with different surface charge densities. (a) Prediction by the PB equation. The closest approach of the K^+ ion to the slit wall was taken as 3.3 Å. The solution dielectric constant was taken as 3.33, same as the result of fitting the sandwich capacitor model (in Figures 4.5 and 4.6) to the capacitance data obtained from micropores immersed in 6 M KOH electrolytes.[16] (b) Predicted by the MD simulations. 37

4.5 Distribution of water molecules around K^+ ion located at different positions in slit pores (shown as different colors) and the coordination number of these water molecules (shown as contour lines). (a) K^+ located at z = 6.03 Å inside a 12.03 Å-wide slit pore, (b) K^+ located at z = 3.30 Å inside a 12.03 Å-wide slit pore, (c) K^+ located at z = 4.68 Å inside a 9.36 Å-wide slit pore, (d) K^+ located at z = 3.30Å inside a 9.36 Å-wide slit pore. 41

List of Figures (Continued)

Figure Page

4.6 (a) Schematic of a sandwich capacitor formed by a layer of counter-ions located exactly midway between two electrodes with the same polarity and separated by W = 2*b*. (b) The equivalent system shown with the electric field lines. The locations of the dashed lines indicate the effective ion radius a_0 of the counter-ions, which is dictated by the spread of electron cloud (Ref. [15]). The effective separation between the electrode surface and the counter-ions is d_{eff}. 44

4.7 Experimental data in Ref. [16] of microporous activated carbon electrode materials in a 6 M aqueous KOH electrolyte fit by the sandwich capacitance model shown in Equation 4.3..... 46

5.1 (a) A schematic of the simulation system. (b) Molecular models of the TEA^+, BF_4^-, and ACN molecules. 50

5.2 (a) Ion−ACN and ion−ion radial distribution function (RDF) in 1.2 M bulk $TEABF_4$/ACN solution. The radial distance is between the ion center, either N or B, and the center of mass of ACN molecules. (b) Distribution of the angle θ formed between the NC vector of the ACN molecules in the first solvation shell of TEA^+ and BF_4^- ions and the vector from the ion center, either N or B, to the N atom of the ACN molecules. 55

5.3 (a) Concentration distribution of ACN molecules near a neutral electrode. The position of ACN molecules is based on their center-of-mass. (b) Orientational distribution of the NC vector of ACN molecules (defined as the vector pointing from the N atom of an ACN molecule to the C atom of its methyl group) with respect to the normal direction of the electrode for ACN molecules at different distance from the electrode. 58

5.4 (a) and (b) Concentration distributions of ACN, TEA^+ and BF_4^- near a neutral electrode. Circles are bare ion diameters of the TEA^+ and BF_4^- ions. 60

List of Figures (Continued)

Figure Page

5.5 Potential energy of the TEA^+ cation and BF_4^- anion at different position above a neutral electrode due to non-electrostatic ion-electrode interactions. 62

5.6 Schematic of the arrangement of ACN molecules, TEA^+, and BF_4^- ions near a neutral electrode. The ellipses denote ACN molecules. 63

5.7 (a) Space charge density of ACN molecules, TEA^+ cations and BF_4^- anions. (b) Electrostatic potential distribution near a neutral electrode. 64

5.8 Concentration profiles of TEA^+ cations and BF_4^- anions near electrodes with charge densities of -0.04 C/m^2 (panel a) and -0.105 C/m^2 (panel b). 65

5.9 Variation of the effective ion accumulation (EIA) factor (panel a) and the charge screening factor (C_f) (panel b) near an electrode with $\sigma = -0.105$ C/m^2. 68

5.10 (a) Concentration distribution of ACN molecules near electrodes with various charge densities. (b) Orientation distribution of the NC vector (defined in the caption of Figure 5.3) of ACN molecules within 0.56 nm of the electrode with respect to the normal direction of electrodes. 70

5.11 Concentration distribution of TEA^+ and BF_4^- ions near electrodes with charge densities of $+0.04$ C/m^2 (panel a) and $+0.105$ C/m^2 (panel b). 71

5.12 (a) Concentration distribution of ACN molecules near electrodes with various charge densities, (b) Orientation distribution of the NC vector of ACN molecules within 0.56nm of the electrode with respect to the normal direction of electrodes. 72

List of Figures (Continued)

Figure Page

5.13 (a) Relation between electrode charge density and potential drop across the EDLs adjacent to the electrodes, (b) Capacitance C_{edl} of the EDLs adjacent to the electrodes with different surface charge densities. 74

5.14 Dipole autocorrelation function for ACN molecules at different locations from the electrodes. (a): ACN molecules in region z < 0.56 nm; (b): ACN molecules in region 0.56 nm < z < 1.12 nm. 76

6.1 Number density of the $[NO_3]^-$ (panel a) and $[BMIM]^+$ (panel b) ions near neutral and negatively charged electrodes. (c) Space charge density profiles near the electrodes. (d, e) Orientational order parameter $P_2(\cos\theta)$ of $[NO_3]^-$ (panel d) and $[BMIM]^+$ (panel e) ions near neutral and negatively charged electrodes. 87

6.2 Number density of $[BMIM]^+$ (panel a) and $[NO_3]^-$ (panel b) ions near neutral and negatively charged electrodes. 88

6.3 (a) Number density profiles of the $[BMIM]^+$ ions near the negatively charged electrode with a surface charge density of -0.09 C/m^2. (b) Mean electrical field near the electrode. (c) The space charge density due to the presence of a $[BMIM]^+$ ion centered at a position 0.34 nm away from the electrode (this position is indicated by a vertical dash line in panel a). 91

6.4 Distribution of the electrical potential across the channel (channel wall charge density: ± 0.03 C/m^2). Because the electrical potential in the central portion of the channel is flat, the potential drop across the EDLs, ϕ_{EDL}, near the upper and lower channel walls can be evaluated from the electrical potential profile shown here. 94

List of Figures (Continued)

Figure Page

6.5 (a) Correlation between the electrode charge density and the electrical potential drop across the EDLs at the interface of [BMIM][NO_3] and planar electrodes. (b) Correlation between the effective EDL capacitance, $C_{\text{eff}} = \sigma / \phi_{EDL}$, and the electrical potential drop across the EDL for systems studied in this paper. (c) Correlation between the EDL differential capacitance, $C = d\sigma / d\phi_{EDL}$, and the electrical potential drop across the EDL. 95

6.6 Response of the EDL structure at operating points 1 and 2 (see Figure 6.5c) as the electrode charge density increases by 0.01 C/m^2 100

6.7 Response of the EDL structure at operating points 3 and 4 (see Figure 6.5c) as the electrode charge density decreases by 0.01 C/m^2. 107

7.1 Snapshots of simulation system with graphene sheets (panel a) and CNT (panel b) as electrodes. The blue, green, and yellow spheres represent $BMIM^+$ ions, PF_6^- ions, and electrode atoms. 114

7.2 Ion number density profile in [BMIM][Cl] (panel a) and [BMIM][PF_6] (panel b) near neutral planar electrodes. The position of the cation and the anion are represented by the geometrical center of the imidazolium ring and the entire anion, respectively. 118

7.3 Ion number density profile in [BMIM][Cl] (panels a and c) and [BMIM][PF_6] (panels b and d) near positive and negative planar electrodes. 119

7.4 Distribution of the angle θ formed between the normal of imidazolium ring in the twin-peaks of $BMIM^+$ ion (see Figures 7.3c and 7.3d) and the normal direction of the electrode with $\sigma = -0.112$C/m^2. 120

List of Figures (Continued)

Figure Page

7.5 Ion number density profile in [BMIM][Cl] (panels a, c) and [BMIM][PF_6] (panels b, d) near positive (panels a, b) and negative (panels c, d) CNT electrodes. 122

7.6 The capacitance of EDLs near planar and CNT electrodes with $\sigma = \pm 0.112$ C/m^2 in contact with different ILs. 123

7.7 Change of ion number densities (panels a and c) and space charge densities (panels b and d) in [BMIM][Cl] near planar electrodes as the electrode charge density is changed from zero to ± 0.112 C/m^2. 128

7.8 The charge screening factor β in [BMIM][Cl] (panel a) and [BMIM][PF_6] (panel b) near negative planar/cylindrical electrodes. The electrode charge density is -0.112C/m^2 in all cases. 132

7.9 A schematic of the "multiple ion layers with overscreening" (MILO) model. The charge of the electrode ($A\sigma$), the first counter-ion layer ($-\beta A\sigma$), and the adjacent co-ion layer ($(\beta-1)A\sigma$) are assumed to be localized at positions 0, 1 and 2. 132

CHAPTER 1

INTRODUCTION

Electrical energy storage devices play a critical role in many high-profile energy technologies. For instance, they can not only store the electricity generated from renewable sources but also power all-electric vehicles as their key components [1]. As a new class of energy storage devices, electrochemical capacitors (ECs), also called electrical double layer capacitors or supercapacitors, have attracted considerable attention in current electrical energy community.

Generally, the device construction of ECs, similar to that of batteries, includes electrodes and electrolytes. When a potential is applied on the electrodes, the ions in electrolytes will be separated to different electrodes, i.e., the cations will be attracted on the negatively charged electrode and anions on the positively charged electrode to form electrical double layers (EDLs). Unlike batteries that store electrical energy in chemical bonds, ECs store energy in such double layers.[2] Essentially, the EDL, with its thickness of only a few nanometers, determines the effective separation of charge and thus the performance of an EC, in other words, the energy storage mechanism of ECs relies on the EDL established at their electrode/electrolyte interface.

Compared with the traditional energy storage devices, such as batteries and conventional capacitors, ECs have several key characteristics. Such comparisons among energy storage devices can be further understood by examining the Ragone plot [3-4] in Figure 1.1, where energy density measures how much energy is stored while power

density indicates how fast the energy can be released from (or replenished into) the system.

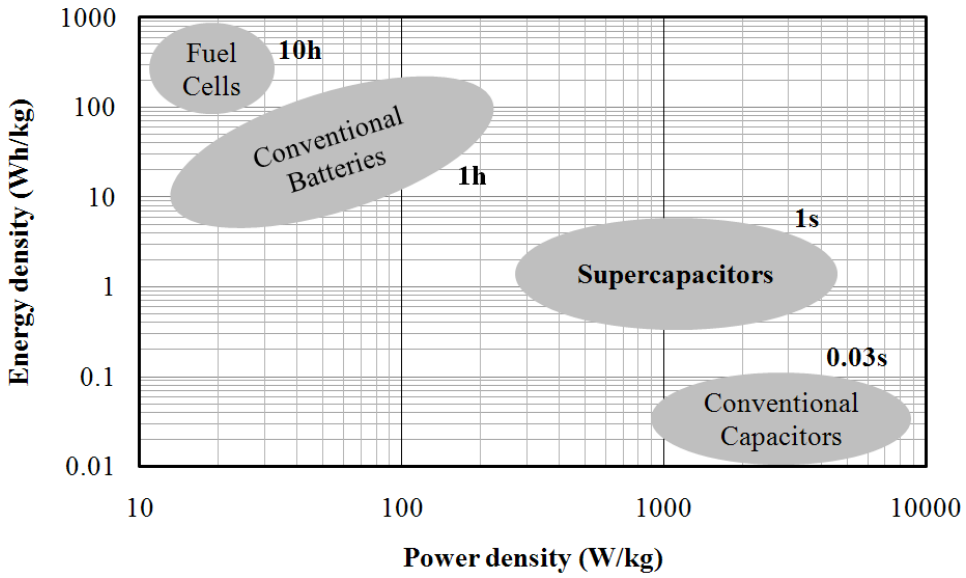

Figure 1.1: Ragone plot for basic electrical energy storage devices. The time for charging-discharging is also indicated on the plot.

Firstly, due to slow bulk diffusion and slow kinetics in chemical reactions, the batteries have a high energy density but suffer from poor power density. In contrast, as an EC is charged, the oppositely charged electrolyte ions migrate towards the electrode and the reverse process during the discharge. Such processes are rapid, usually on the order of a few seconds (cf. Figure 1.1). Accordingly, ECs have a high power density, which makes them ideal for the rapid storage and release of energy. Secondly, chemical reactions (e.g., oxidation-reduction reactions), taking place on the electrode surface, make the charging and discharging processes inside batteries not fully reversible. Thus, batteries have generally several thousand charging-discharging cycles. Impressively, ECs, in theory, can be cycled unlimitedly, because energy is stored electrostatically

between solid electrodes without chemical or phase changes [5]. Thirdly, as shown in Figure 1.1, conventional capacitors are usually working fast (e.g., they are used in many electronic switching devices) but have limited energy density, because they store energy on two metallic conductors separated by inside dielectric medium through moving the charge carriers from one conductor to the other, whereas the potential between their conductors is confined by the dielectric breakdown. Contrastively, ECs, without any insulator, have no danger of the dielectric breakdown, and also no full-charge detection is needed in ECs compared with batteries. Finally, ECs have good performance at relatively low temperature, since there are no compositions and chemical phase changes during the discharging/recharging process [6]. Because of these valuable properties, ECs are being considered as an ideal solution to applications of many hybrid electrical energy storages.[7-9]

However, the primary limitation of ECs is their moderate energy density (ρ_E), which is typically less than 10 Wh/kg, whereas batteries have the energy density on the order of 100 Wh/kg [8-9]. Here, the energy density can be obtained by

$$\rho_E = W_{stored} / M \tag{1.1}$$

where W_{stored} is the energy stored in a system and M is the total system mass majorly coming from electrodes and electrolytes. It is well known that the energy stored in a capacitor is determined by its total capacitance and the applied potential between its cathode and anode, i.e.,

$$W_{stored} = C_{tot} V^2 / 2 \tag{1.2}$$

where C_{tot} is the total capacitance, and V is the applied potential. C_{tot} can be further decomposed as

$$C_{tot} = AC \tag{1.3}$$

where A is the total electrode surface area, and C is the normalized capacitance (the total capacitance divided by the total electrode surface area, unit: $\mu F/cm^2$ or F/m^2). Based on equations 1.1~1.3, to overcome the limitation of ECs, four strategies can be implemented: (1) reduction of the system mass , (2) improvement of the electrode surface area, (3) enhancement of the normalized capacitance, and (4) increase of the working voltage of the applied potential on the electrodes.

Prior researchers have invested much time to develop porous electrodes to improve the electrode surface area and thus the energy density. The idea is that decreasing the size of the pores on the electrode can increase the number of pores per unit volume and the specific surface area as well. Typically, activated carbon is chosen as the electrode, because it has not only tunable porosity but also high electrical conductivity, relatively low production cost and small specific weight.[10-12] Figure 1.2 shows a schematic of an EC with activated carbons as porous electrodes immersed into the electrolytes. The activated carbons are clusters of carbon particles, and the separator, made of a porous membrane of paper, polymer, or glass fiber, is used to avoid the cathode mixing with the anode but allow the electrolyte to freely go through. A close examination of the electrode topographic feature reveals that each carbon particle in the activated carbon electrode contains a large amount of pores with different structures.

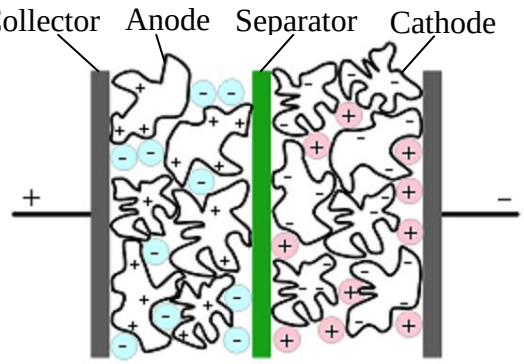

Figure 1.2: A schematic of an EC. Reproduced from Ref. [13].

In terms of topology, pores belonging to the electrodes can be classified as cylindrical pore and slit-shaped pore. Based on their size (here, the diameter of cylindrical pores and the distance between two solid surfaces in slits are characterized as their size), the pores are categorized into three types by IUPAC [14]: the macropore has the size larger than 50nm, the size of a mesopore is between 2nm and 50nm, and micropores are less than 2nm. Specifically, (1) in a macropore, the curvature effect from the pore walls can be neglected, because their radius of curved surface is much larger than the EDL thickness so that the EDL near the electrode can be treated as that near the planar electrode. This situation is sketched in Figure 1.3a, which exhibits an EDL near the planar electrode and beyond the EDL region there is nothing but the electrolyte bulk. (2) In the slit-shaped mesopore, the EDL near each pore wall may overlap, if the EDL is more than one nanometer thick. In the cylindrical mesopore (see Figure 1.3b), the ions (mostly counter-ions) get in the pore and form an electric double-cylinder capacitor (EDCC) [15]. (3) In the slit-shaped micropore (see Figure 1.3c), two pore walls might share one EDL between them due to the quite small inside space. In the cylindrical

micropore (see Figure 1.3d), counter-ions stay at/around the pore center to form an electric wire-in-cylinder capacitor (EWCC) [15]. According to where is the EDL, an endohedral EDL represents the one formed by the electrolytes entering the pores (cf. Figure 1.3b~d), while an exohedral EDL is constructed by the electrolytes accumulated on the outside surfaces of the pores or solid entities (e.g., cylinders) as shown in Figure 1.3e. Typically, an EC can have all three types of the pores above and corresponding EDLs formed inside/outside pores.

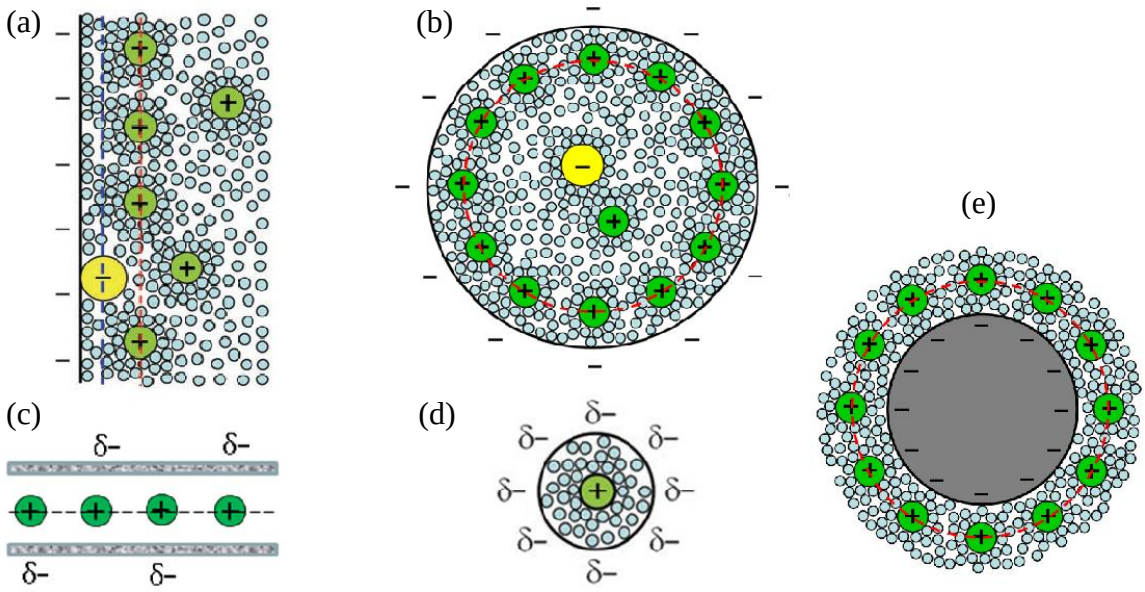

Figure 1.3: Different types of pores on the electrode: (a) macropore, (b) mesopore, (c) slit-shaped micropore, (d) cylindrical micropore, and (e) cylindrical pore with ourside electrolytes. (a), (b), (d) and (e) are reproduced from Ref. [15].

The pores on electrodes are used to improve the energy density of ECs not only by enlarging the electrode surface area but also by enhancing the normalized capacitance. For example, the area-normalized capacitance has been found to have a sharp increase when the pore size of activated carbon electrodes decreases into the micropore

region.[16] Hence, four approaches to improve ECs' energy density are not independent at all. In fact, the research and development of ECs may involve both, three or all of them.

Excepting the porous electrodes, the capacitance of an EC is also determined by its inside electrolytes, because the charge separation mainly takes place in the EDL that is essentially a packing of electrolytes. Therefore, making a choice of the electrolyte is definitely a good way to achieve a large capacitance as well as to increase the energy density. Moreover, the small density of electrolytes would also facilitate high energy density by lessening the system mass. Importantly, different electrolytes have different decomposition voltages, which provides us the probability that the EC can afford a high working voltage and thus the high energy density based on Equation 1.2.

Generally, the electrolytes used in ECs are aqueous electrolytes, molten salts, organic electrolytes and ionic liquids (ILs). Currently, molten salts are limited to use because such ECs work under very high temperature. Typically, aqueous electrolytes are widely used, such as sulfuric acid and KOH solution in carbon-type ECs. Although ECs using aqueous electrolytes benefits from their good conductivity, the "working voltages" of aqueous electrolytes restrict their wide employment due to their key limitation that the decomposition voltage is rather small (theoretically 1.23V, or practically, in kinetic terms, 1.3-1.4V) [2]. Besides, the corrosion of the hardware components of ECs is a problem that cannot be neglected for their reliability and safety. To have a larger decomposition voltage, non-aqueous electrolytes are chosen in ECs: (1) Organic electrolytes have a larger operating potential (typically ~ 2.7 V), which helps increase the

energy density of ECs. (2) Recently, room-temperature ILs have attracted significant attention in industry and academia. Because of their wide electrochemical windows, excellent thermal stability, non-volatility, and good ionic conductivity, ILs are used in diverse electrochemical devices [17]. In particular, IL is a promising candidate of the electrolytes in ECs.

In a word, electrolytes used in an EC have an intimate relation with the system mass, the normalized capacitance of their formed EDLs, and the potential they can sustain, and thus the selection of the electrolyte is very important to optimize the EC's energy density.

Essentially, the implementation of four approaches above for improving ECs' energy density critically hinges on the fundamental understanding of their EDLs in different electrolytes in/near different porous electrodes. To probe the underlying energy storage principles of ECs, in this dissertation, we address the following issues:

1) Although the EDLs in aqueous electrolytes near the planar electrodes have been studied extensively, EDLs in aqueous electrolytes inside the microporous electrodes are limited to study. Fundamental understanding is still lacking. For instance, how would the solvent/ion distribute in the micropores? What's the difference from those near the planar electrodes? Especially, what's the mechanism of the sharp increase of capacitance in micropores?
2) For the electrodes with macropores, what would be the structure of EDLs formed by large size ions near the planar electrodes, e.g., ions in organic electrolytes or ILs? Although both organic electrolytes and aqueous

electrolytes consist of cations, anions, and solvent, their ions and solvent molecules have different natures. Hence, what's such difference between aqueous and organic electrolytes? Will the solvent/ion nature change when the electrolytes are close to the planar electrodes? Would the EDL formed by organic electrolytes also be similar with that in aqueous electrolytes?

3) For the ILs, without any solvent, what would be the structure of the EDL near the planar electrode? How would the nature of ILs (i.e., the "ionic" nature and "liquid" nature) play the role in shaping EDLs? Could such EDL structures be explained by the conclusions drawn from EDLs in aqueous electrolytes? What's the EDL capacitance, and would such capacitance change as the potential applied on the electrodes changes?
4) Taking a further step, since ILs can be composed with different ion pairs, would ion size affect the EDL structure and capacitance? When the ILs form EDLs near the exohedral surface of the pores on electrodes, would the pore curvature impact the structure and capacitance of EDLs?

The rest of this dissertation is organized as follows: in Chapter 2 we review the prior work on EDLs in ECs; in Chapter 3, we describe the model and methodology used in this dissertation; Chapter 4 presents the ion distribution in electrified micropores and its role in the anomalous enhancement of capacitance; Chapter 5 delineates the structure, capacitance and dynamics of EDLs in organic electrolytes; we explore microstructure and capacitance of the EDLs at the interface of ILs and planar electrodes in Chapter 6; we

reveal the importance of ion size and electrode curvature on EDLs in ILs in Chapter 7; the conclusions are drawn in Chapter 8.

CHAPTER 2

PRIOR STUDIES OF EDLS

In the past decades, myriads of experiments have been done to explore the performance of various ECs. Coupled with experimental results, theoretical studies have provided important insights into the electrode/electrolyte interfacial behavior that is crucial for the understanding of the capacitance performance of ECs and subsequently for their optimization. In this chapter, we review the theories and experimental work on EDLs in ECs. Following on the prior studies done for ECs, we point out the work we plan to do for the investigation of EDLs in ECs.

2.1 Theoretical Models of EDLs

EDLs, especially those in aqueous electrolytes, have been extensively studied since one century ago, and many models have been proposed to describe the structure of the interface of electrolyte/electrode. The models are reviewed following the time when they were first proposed.

The earliest model (see Figure 2.1a) for the description of EDLs near electrodes came from Helmholtz who introduced the concept of "electrical double layer" in his model for the first time. Helmholtz model[18] states that due to the electrical attraction resulting from the charged surface, counter-ions are absorbed on the electrode and form an EDL in which there is only one layer of counter-ions and the charge of EDL

compensates exactly the surface charge. Although this simple model can explain some experimental results of EDLs, it contradicts most electrokinetic experiments.

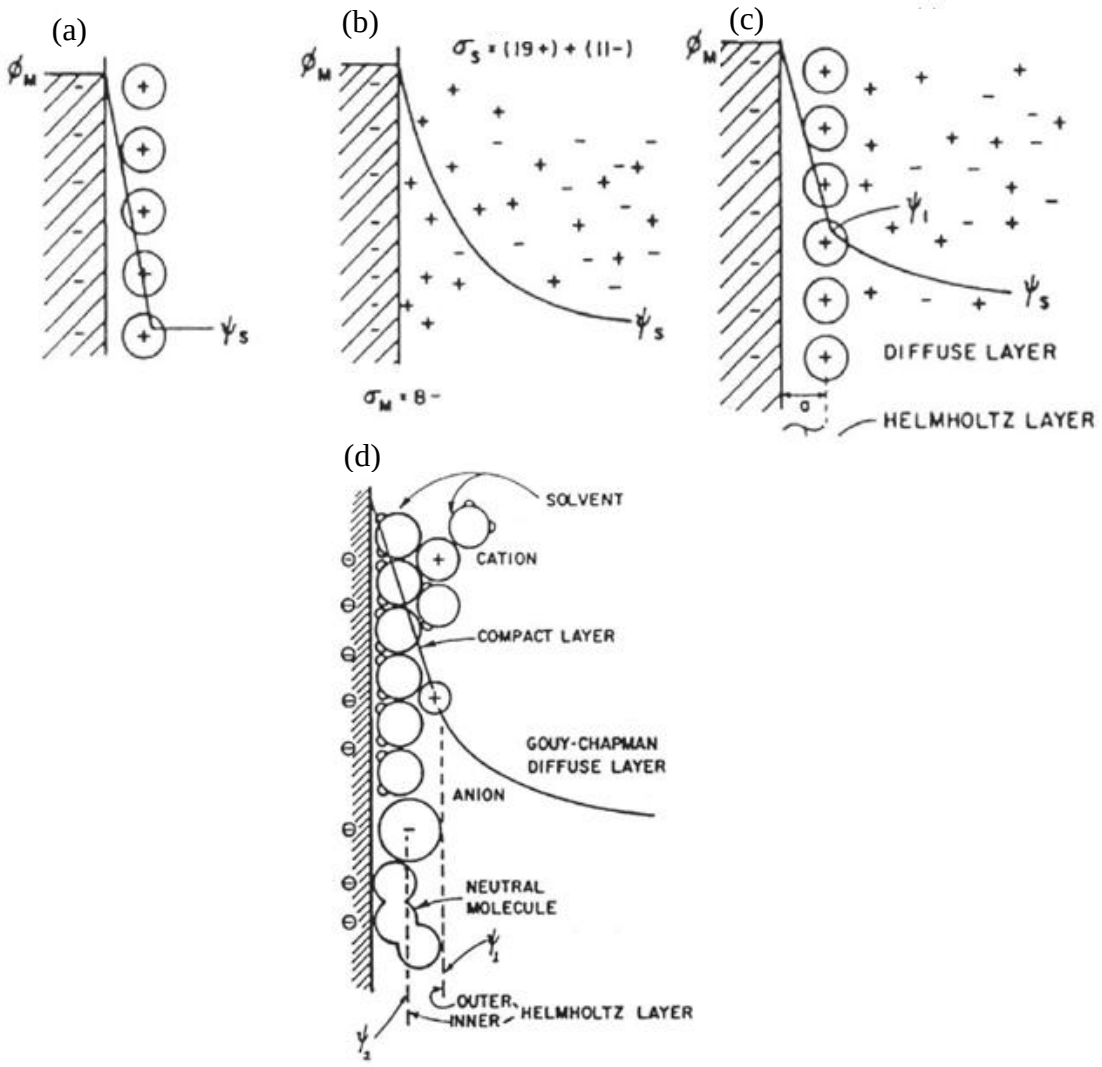

Figure 2.1: Models of the EDLs: (a) Helmholtz model, (b) Gouy-Chapman model, (c) Gouy-Stern model, and (d) general representation of EDL. Reproduced from Ref. [2].

Gouy and Chapman took a further step to consider that the counter-ions together with co-ions form a diffusive layer near the electrode due to the thermal fluctuation in electrolytes [2]. They derived the Poisson-Boltzmann (PB) equation to calculate the

potential distribution inside the EDL by assuming that ions are point charges [19]. Neglecting the discretization of the surface charge, Gouy-Chapman theory can predict well for monovalent ions at low concentration (< 0.2M) and potential (< 80mV). However, ignoring the finite ion size causes PB equation to predict an unrealistically high concentration of ions very close to the electrode and an overestimation of EDL capacitance.[19]

The limitation in the Gouy-Chapman theory was partially addressed by the Gouy-Stern model (see Figure 2.1c). In this model, the EDL region is divided into two parts. The inner region consists of a layer of counter-ions absorbed on the charged surface, which is essentially the Helmholtz layer. Beyond such compact layer, a "diffuse" layer is observed. The overall EDL capacitance is dictated by the capacitance of the compact layer and the diffuse layer in series. However, in practice, the interfacial position between Helmholtz layer and diffusive layer is very difficult to measure, especially, taking into account of the local interactions among surface, ions, or solvent molecules.

Considering the nature of cation/anion in electrolytes (such as their size, polarizability, and adsorption on solid surface) and solvation effects, a more complicated EDL model was proposed by Grahame as shown in Figure 2.1d. Grahame divided the Helmholtz layer further into two sub-layers: an inner layer consists of specifically adsorbed ions and their solvation solvent molecules, and an outer layer consists of solvated ions. The inner Helmholtz layer is between the charged surface and the inner Helmholtz plane (IHP). Usually, the solvation molecules in the inner Helmholtz layer will strongly be oriented compared with those in electrolyte bulk. Beyond the inner

Helmholtz layer, the region extending to the outer Helmholtz plane (OHP) is the outer Helmholtz layer. The part beyond the outer Helmholtz layer is the Gouy-Chapman diffuse layer due to the thermal motion of electrolytes.

The fundamental understanding of the structure, capacitance, and dynamics of EDLs in different electrolytes can benefit from the above EDL models, and vice versa.

2.2 EDLs in Aqueous Electrolytes

The EDLs in aqueous electrolytes have been studied extensively, since the aqueous electrolytes are most widely used in ECs [20-24]. For example, in NaCl solution, Na^+ concentration has double peaks near the electrode. Some I^- and Cl^- ions can be adsorbed on the open surface electrode so that a peak of their concentration distributions appears even near the electrode with zero surface charge density.[25] To analyze the origins of shaping EDLs, people found that ions are strongly hydrated by water molecules, and such hydration plays a key role in determining the structure of EDLs in aqueous electrolytes [26-28]. For the EDL capacitance, the typical value of EDLs in NaCl solution with the carbon electrode is *ca.*10 $\mu F/cm^2$ [2]. However, numerous researches on EDLs in aqueous electrolytes are almost for ECs with open surface electrodes (see Figure 1.3a). Current knowledge of the EDLs in micropores (see Figure 1.3c and d) is still rudimentary but quite needed, because electrodes featuring micropores are increasingly being used and impressive improvement in energy density has been made recently [8-9]. For example, the area-normalized capacitance of activated carbon

electrodes immersed in 6 M KOH solution has been found to increase from ~6 $\mu F/cm^2$ to ~12 $\mu F/cm^2$ as the mean pore size of the electrode decreases from 14.5 Å to 10.6 Å [16]. However, such scaling between the capacitance and the electrode pore size cannot be explained even qualitatively by the classical EDL theories based on the PB equation [29-30].

To rationalize the anomalous enhancement of capacitance in micropores, the EWCC model has recently been proposed, which captures two key effects: (1) confinement and (2) curvature.[15] The main idea is that counter-ions form a wire along the axis of small diameter cylindrical micropores, resulting in a different capacitance regime from that of mesopore structures where curvature effects are also needed for a quantitative description, even though they display smaller mean curvature as compared to micropores. The EWCC model has been shown to fit remarkably well to available experimental data [15]. Although this model sheds light on the anomalous enhancement of capacitance in micropores, many issues remain open. First, it is often thought that micropores are slit-shaped instead of cylindrical, and thus the EWCC model may not always be applicable, depending on electrode materials synthesis and processing. Second, while the assumption that ions accumulate along the center of electrified micropores seems reasonable from a purely geometric confinement standpoint, details on the confining processes remains largely unproven in the complex electrolyte-electrode interface structure. In fact, because the classical EDL theories were developed for relatively large pores, the second assumption is against the prediction of the classical EDL theories [29], which state that counter-ions accumulate primarily in separate layers

near each slit wall. However, classical EDL theories are mostly based on the assumption that the ion-distribution is governed only by the electrostatic ion-ion interactions, and thus predictions based on classical theories may not be accurate.

In relation to the above-mentioned issues, many fundamental questions remain to be studied. For example, how will the solvent and ions distribute inside micropores and what are their origins? What are the hydration characteristics of ions at different positions in electrified micropores, and how and to what extent do they affect the ion distribution? At present, most molecular simulations of EDLs deal with mesopores [31-35] and few studies have been reported for the ion distribution in micropores [36]. The limited molecular studies of micropores are focused on neutral pores and the average ion hydration characteristics in such pores [37-38], and how the hydration of ions across the pore affects the ion distribution have not been studied extensively.

2.3 EDLs in Organic Electrolytes

Unlike the aqueous electrolyte, notably less effort has been devoted to understand the EDL structure in the organic electrolyte, in spite of the breakthrough made in experiments recently.[8] Mostly, the work on organic electrolytes centers on the electrolytic conductivity, a stable potential window, and the dielectric constant.[39-43] Comparatively, atomistic level studies of such EDLs are relatively scarce.[44-45] The current understanding of EDLs in organic electrolytes is either inferred from capacitance measurements of carbon electrodes in organic electrolytes or is based on insights gained

from the extensive studies of EDLs in aqueous electrolytes.[20-24] A recent study by Pratt and co-workers examined EDLs formed at the outer surface of carbon nanotubes (CNTs) immersed into organic electrolytes of 1.0 M tetraethylammonium tetrafluoroborate ($TEABF_4$) with propylene carbonate as solvent.[46] They computed the ion and electrical potential distributions near the CNT (radius = 1.17 nm) and showed that, under high electrode charge density ($|\sigma|$ = 0.23 C/m^2), organic ions are contact-adsorbed on the CNT surfaces. Although that study revealed important aspects of the EDLs in organic electrolytes, many key questions remain unanswered: (1) how will the structure and the capacitance of the EDLs change as the electrode charge density (or potential) changes? (2) how will the structure and dynamics of the interfacial solvents change as the electrode becomes electrified? (3) will organic ions become contact-adsorbed on electrodes with small curvature or moderate charge density? (4) what is the role of ion solvation in determining the structure of the EDLs? (5) can the ion distribution in EDLs be accurately described by the classical EDL models?

2.4 EDLs in Ionic Liquids

In recent years, room-temperature ionic liquids (RTILs) have attracted significant attention in fundamental and applied research. The extensive interest is in part due to their wide electrochemical windows, excellent thermal stability, non-volatility, relatively inert nature, and good ionic conductivity, which make ILs exceptionally useful in diverse electrochemical devices (e.g., as a promising type of electrolytes in ECs). [17, 47-48]

Unlike organic electrolytes having solvent, ILs are composed entirely of organic cations and organic/inorganic anions,[47, 49] and often feature a complex shape, generally, with charge delocalized among many atoms of their polyatomic ions.[24] Most of ILs have very low vapor pressure and excellent thermal stability. These properties offer distinct advantages for the utility of ECs, in which the microstructure and capacitance of the EDLs at the interface of ILs/electrodes play an essential role in determining the system performance.

Given the solvent-free nature of the ILs and the complex shape of the ions in ILs, it is expected that the classical theories for the EDLs in dilute aqueous electrolytes and high-temperature molten salts cannot accurately describe the structure and properties of the EDLs at the interface of ILs and electrified surfaces. [50-51] During the past decade, the structures of EDLs have been studied by experimental and analytical methods. Experimental data suggest that the IL-electrode interface is one ion layer thick (typically 3-5 Å) [52], which supports the idea that the EDLs in ILs are essentially Helmholtz layers. Surface frequency generation data indicate that the interfacial cations exhibit orientational ordering and their orientation depends not only on the electrical potential of the electrode but also on the type of anions in the ILs.[52-53] Recently, several elegant analytical models have been proposed to describe the EDLs in ILs. [50-51] It was hypothesized that the EDLs in ILs consist of a compact inner layer and a "diffusive" outer layer. Although these new models are still mean-field theories and focus on the role of long-range electrostatic interactions in determining the EDL structure, the solvent-free nature of the ILs is accounted for. In general, the most extensively studied macroscopic

property of the EDLs in ILs is their differential capacitance.[52, 54-56] Several different trends of capacitance-electrode potential (*C*-*V*) curves have been reported. Whereas concave *C*-*V* curves were observed in many experiments,[52, 55-56] bell-shaped and camel-like *C*-*V* curves have also been reported.[54] Although none of the existing theories can rigorously explain these diverse and seemingly contradictory experimental observations, important progress has been made recently. For example, the bell-shaped and camel-like *C*-*V* curves can be explained by the EDL models proposed by Kornyshev and Oldham,[50-51] although rigorous justification of the model parameter remains a challenge.[54]

However, systematic study of the EDLs near an electrified surface by using atomistic simulations is rare. In Ref. [57], the density and orientation of IL ions near a structureless electrode with low surface charge density (± 0.02 C/m^2) were studied by using molecular dynamics (MD) simulations. In this study, a Helmholtz layer-like counter-ion layer near charged electrodes, consistent with that inferred from experimental studies, was, indeed, observed. However, the orientational ordering of the cation persists at a position $\sim$10Å from the electrode, which is far greater as compared to the EDL thickness inferred from experimental data.[52] In Ref. [58], the capacitance of a minimal-model IL was studied by MD simulations, and a quasi-bell-like *C*-*V* curve was observed, in qualitative agreement with some earlier experimental results.[54] Although the solvent-free nature of the IL and size asymmetry of the cations and anions are accounted for in this pioneering study, other important molecular details of the ILs (e.g., the complex shape and charge delocalization of the ions) are neglected. Despite these work,

many functional issues for EDLs in ILs remain pendent. For instance, (1) how the nature of ions will affect the EDL structure? (2) to what extent the classical EDL models are suitable for explaining the EDLs in ILs? (3) which type of *C*-*V* curves should the EDL capacitance obey for the specific type of ILs? Is there a universal trend of *C*-*V* curve? (4) why will the *C*-*V* curve for specific EDLs be bell-shaped, convex, concave-shaped, or camel-like?

Regardless of their trends, most published *C*-*V* curves [52, 54, 59] are not symmetric, because the EDL formed at the cathode side is different from that at the anode side, which essentially is accounted for the ion size. Fedorov and Kornyshev studied the EDLs in ILs modeled by charged Lennard-Jones spheres and found that the cation/anion size asymmetry affects the trend of differential capacitance.[58] Sedev and colleagues found experimentally that the differential capacitance increased in the order [HMIM][Cl] < [BMIM][Cl] < [EMIM][Cl] due to the different cation sizes.[54] These studies improved the understanding of how the nature of ILs affects the EDL. However, a systematic molecular level study of how ion size affects the EDL structure and capacitance is still lacking at present.

As well known, the characteristics of EDL are determined by both electrolytes and electrodes. For the electrode effects, most researches of EDLs are focused on the electrode material. For example, Islam and co-authors [59] reported that the minimum capacitance of EDLs in ILs near the highly oriented pyrolytic graphite (HOPG) was 2.2 $\mu F/cm^2$, which is significantly smaller than those at glassy carbon (GC) or metal

electrodes (>10 μF/cm^2). However, up to now, a detailed study of the influence of electrode curvatures on the EDLs in ILs has not been reported yet.

Without a doubt, the fundamental understanding of the effects of ion size and electrode curvature on EDLs in ILs can also benefit from a realistic model of EDLs. However, although the classical EDL models (e.g., Helmholtz model) seem to be supported by some experimental characterizations of EDLs, most MD simulations suggest that alternating layers of counter-ions and co-ions penetrate deep (> 1 nm) into the electrolyte.[60-62] More advanced models, e.g. the ones proposed by Kornyshev [50] and Oldham,[51] assumed that the EDLs in ILs are made of a Helmholtz-like inner layer and a "diffusive" outer layer. Although these elegant models capture some features of the EDL structure, and can predict qualitatively the experimentally observed *C*-*V* curves, they are mostly mean-field theories and cannot depict some key aspects of EDL in ILs, e.g. the overscreening of electrode charge in the EDL.[63-64] Thus, theoretical capacitance models, in which the key characteristics of EDL structure should be captured as well, are needed to develop for EDLs in ILs.

CHAPTER 3

METHOD AND METHODOLOGY

Using numerical simulations and experimental methods, EDLs in ECs have been studied in many different contexts. Compared with experiments, numerical simulation can provide detailed information of EDLs at microscopic level (e.g., the charge distribution across an EDL), which would be quite difficult to obtain from experiments. Since the thickness of EDLs in ECs typically spans less than a few nanometers, EDLs are amenable to both continuum and atomistic simulations. In comparison with continuum simulations, using atomistic simulations, the nature of electrolytes and electrodes can be modeled explicitly with fewer assumptions, e.g., the solvent and ions are treated as a continuous medium with continuous charge distributions in continuum simulations,[19] while they have finite size and the charge is distributed among their atoms in atomistic simulations. Hence, atomistic simulations are useful tools to investigate EDLs in ECs. Molecular Dynamics (MD) is one of the most widely used atomistic techniques. In this chapter, we present the details of MD simulations used to study the EDLs.

3.1 Molecular Dynamics Simulation

MD simulation is a technique for computing the equilibrium and transport properties of a classical many-body system.[65] Specifically, MD simulation, used for the atomistic system, consists of numerical solution of the classical equation of motion. Figure 3.1a shows the basic MD algorithm, which is very similar to real experiments in

many respects, i.e., in experiments, a sample was prepared and connected with measurement instruments, and then the property of interest would be measured during a certain time span.[65] In MD simulation, given initial condition of an atomic system with its atoms interacting following their intermolecular potentials, MD will do the force calculation to update the system configuration within the user required time. Meanwhile, useful information at the microscopic level, including atomic positions, velocities, forces, etc., would be output to further acquire the system properties related to the phases, the structure and the dynamics (cf. Figure 3.1a). The conversion of such microscopic information to macroscopic observables such as pressure, energy, heat capacities, etc., requires statistical mechanics theories, which behaves as the actual measurement in experiments. In fact, MD simulation serves as a powerful complement to traditional experiments, which has built a bridge not only between microscopic length/time and macroscopic world but also between the theories and experiments (cf. Figure 3.1b).[66]

Choosing proper model and force fields for the energy storage system, we can use MD simulation to model the ECs explicitly. We take the solid wall as the electrode and the electrolytes are modeled by atoms/molecules with the chemical details, such as finite atom size, partial charge, and bonds and band angles in polyatomic molecules or ions. In our research, two-body potentials, e.g., Lennard-Jones (LJ) potential, are suitably used to describe the non-electrostatic intermolecular interactions due to the following reason:

Many-body potentials are used in modeling metals, crystals and states involving faradic reactions, whereas our work is focused on the fluid side of EDLs. The interactions between/among the atoms/molecules do not rely on the bonds formed between ions or

molecules, i.e., there is no chemical bond created/broken between molecules, so that their interactions can be approximated by two-body potentials. Particularly, LJ potential is adopted by the MD community for its efficiency and generally acceptable performance. We also note that intermolecular many-body interactions are considered to some extent in MD by using bonded interactions including bond stretching (two-body), bond angle (three-body), and dihedral angle (four-body) interactions.

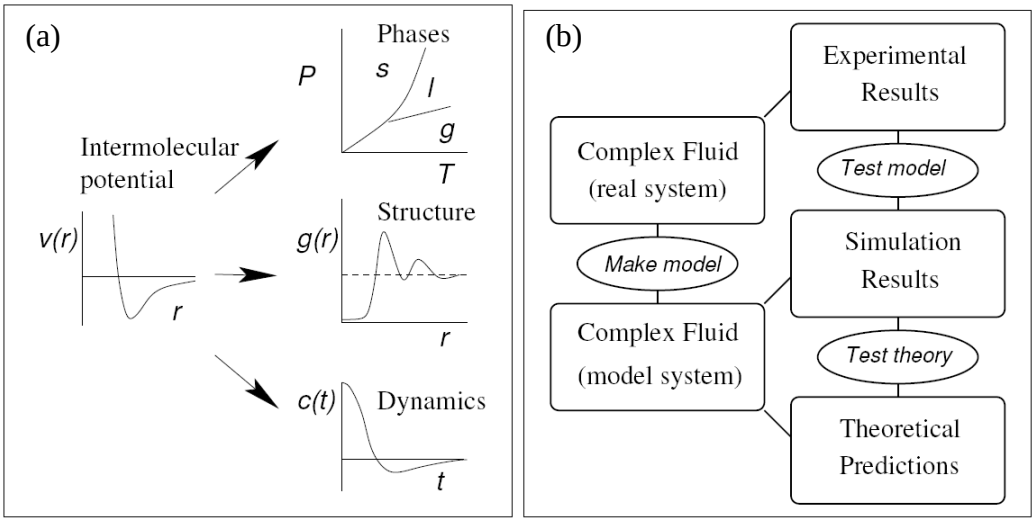

Figure 3.1: Simulations as a bridge between (a) microscopic and macroscopic; (b) theory and experiment. Reproduced from Ref. [66].

Hence, MD simulations of the electrode/electrolyte interface are an appropriate way to probe the EDLs at the molecular level, which is critical for the understanding of charge storage mechanism in ECs.

3.2 Data Analysis

Like in experiments, data analysis is decisive to gain the scientific insights behind the raw data from MD simulation. To obtain the properties of an atomistic system, the trajectories (including atomic positions, velocities, and forces on all system particles) generated by MD simulations can be analyzed during the simulation running or after the simulation is finished. For EDLs in ECs, the major properties are those related to the EDL structure and capacitance.

3.2.1 EDL Structure Description

Using the binning method [67] to analyze the data from MD trajectories, we can obtain the concentration/charge distributions of solvent/ions in the direction perpendicular to the electrode surface, which provide details of EDL structure. Figure 3.2a and Figure 3.2b show the number density distributions of water/ions and the total space charge density coming from the electrolytes near a neutral charged electrode with planar surface, respectively. The oscillation of both number density and space charge density is within ~1nm from the electrode, which is the span of the EDL in that simulation. If more knowledge of EDL structure (e.g., how water molecules and ions pack on the electrode) is of interest, the orientation of solvent and the ion solvation need to be analyzed in detail.

To explore the formation of EDLs during the charging process, the dynamic properties (e.g., the diffusion coefficient) are needed to gain by data analysis.[2]

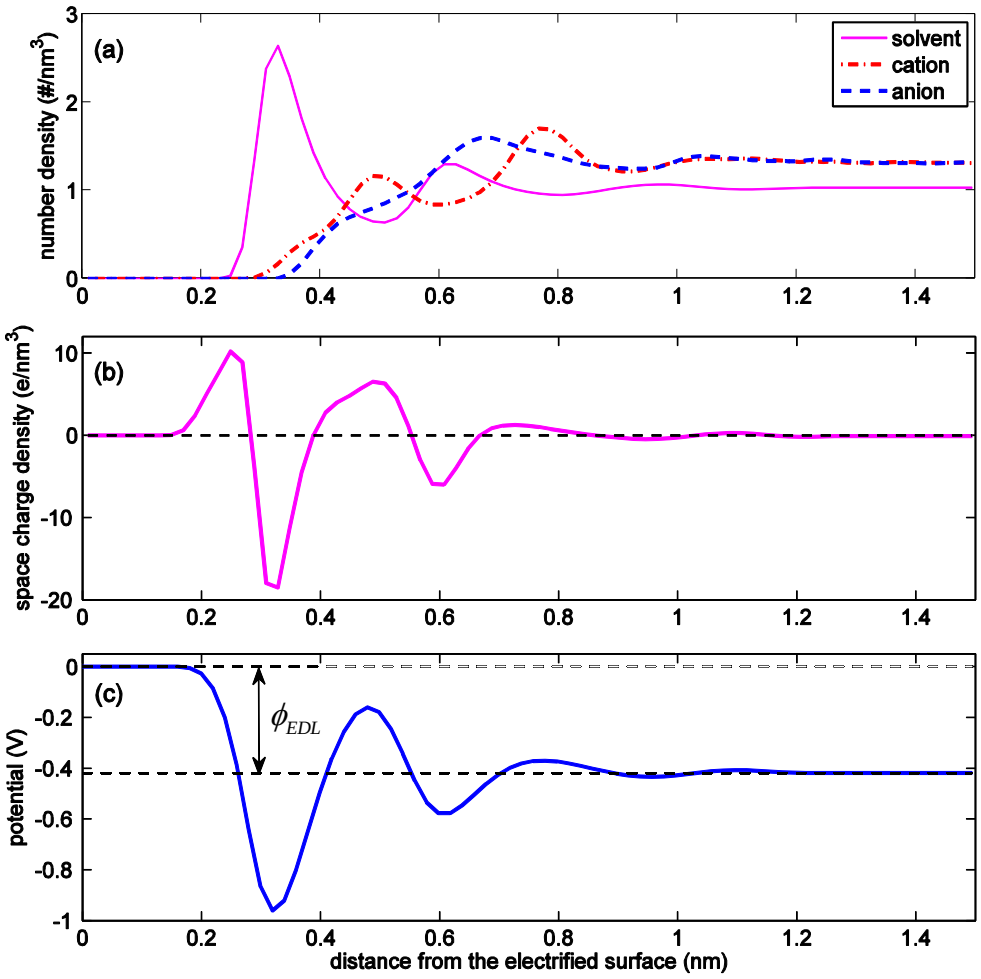

Figure 3.2: Results from MD simulations of NaCl in water near a neutral electrode: (a) number density, where the water number density has been divided by a factor of 30, (b) the total space charge density, and (c) potential distribution.

3.2.2 EDL Capacitance Calculations

EDL capacitance is the most important macroscopic property of an EC, which is crucial to determine the EC's energy density based on Equation 1.2. The capacitance of a capacitor can be calculated by, $C/A = Q/\Phi$, where A and Q are the area and the charge on the surface of the cathode, respectively, and Φ is the potential drop between the

anode and the cathode. It follows that if one wishes to compute the area normalized capacitance (C_{EDL}) of an EDL, the following equation can be used

$$C_{EDL} = \frac{\sigma}{\phi_{EDL} - PZC} \tag{3.1}$$

where σ is the surface charge density of the electrode on which such EDL is formed. If σ is unknown, it can be calculated by

$$\sigma = -\int_{EDL} \rho_e du \tag{3.2}$$

where ρ_e is the space charge density across an EDL (cf. Figure 3.2b), and u is along the normal direction of electrode surface. In Equation 3.1, ϕ_{EDL} is the potential drop across the EDL near the electrode with surface charge density of σ, and *PZC* is the potential of zero charge, i.e., ϕ_{EDL} at $\sigma = 0$ (Figure 3.2c shows the potential distribution and the potential drop across the EDL). Then, the term of $\phi_{EDL} - PZC$ represents the change of potential drop across the EDL, as the electrode is changed with its surface charge density varying from *zero* to σ. To obtain $\phi_{EDL} - PZC$, we need information of the potential distribution throughout the EDL near the electrode with surface charge densities of σ and *zero*. Such potential distribution, ϕ, can be achieved by Poisson equation as follows,

$$\nabla^2 \phi = -\frac{\rho_e}{\varepsilon_r \varepsilon_0} \tag{3.3}$$

where ε_r and ε_0 are dielectric constant of the EDL and the vacuum permittivity, respectively. Since the ions and/or solvent of electrolytes are explicitly modeled in MD simulations, we take $\varepsilon_r = 1$ (note that this is a rather strong assumption, which determines the magnitude of EDL capacitance but is independent of EDL structure and the scaling of *C*-*V* curve), so that Equation 3.3 is reduced to

$$\nabla^2 \phi = -\frac{\rho_e}{\varepsilon_0} \tag{3.4}$$

To solve Equation 3.4, two boundary conditions are required. Here, the potential on the electrode surface is always set as zero, i.e., $\phi\big|_{electrode} = 0$. The other boundary condition is prescribed at position away from the electrode. If the simulation system is wide enough, e.g., EDLs near the open electrode surface (cf. Figure 1.3a and e), we enforce $\nabla\phi = 0$ in the bulk electrolyte, since the potential is equivalent everywhere in the bulk region. If the system exhibits symmetry, e.g., the cylindrical meso/micropores (cf. Figure 1.1b and d) and the slit-shaped pore (cf. Figure 1.3c), we enforce $\nabla\phi = 0$ on the axis of a cylindrical pore or the symmetric plane of a slit-shaped pore, where the potential gradient is physically zero. With these two boundary conditions and ρ_e retrieved from MD simulation, we can solve Equation 3.4 to obtain the potential distribution across the EDL near the electrode with a surface charge density of σ.

CHAPTER 4

EDLS IN AQUEOUS ELECTROLYTES FILLED MICROPORES

As reviewed in Chapter 2, aqueous electrolytes near open surfaces have been studied comprehensively, while less work has been done to procure the fundamentals of EDLs in micropores. In this chapter, to gain insights on the structure and capacitance of EDLs in micropores filled with aqueous electrolytes, we investigate the distribution of K^+ ions inside electrified slit-shaped micropores using MD simulations with an emphasis on the role of ion hydration and ion-ion electrostatic interactions on the ion distribution inside the pore. K^+ ions were studied as they are frequently used in aqueous electrolyte-based ECs. Based on the insights gained, we aim to construct a new model for EDLs in slit-shaped micropores to predict the anomalous enhancement of capacitance observed experimentally in micropores [16].

4.1 MD Simulation Setup

The MD simulations, all MD simulations in this dissertation, were performed using a customized version of MD package Gromacs.[68] Figure 4.1 shows the snapshot of an MD simulation of a slit pore in ECs. The electrolytes (solvent + ions) are enclosed between two electrodes. To model the electrical field generated from the applied potential on the electrodes, the charge is uniformly distributed on the electrode. Essentially, if the electrodes carry the surface charge density with the same sign, the simulation system

contains two ECs in parallel. If the electrodes carry the surface charge density with the opposite sign, the simulation system contains two ECs in series.

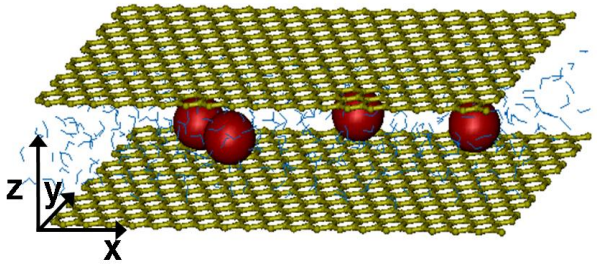

Figure 4.1: A snapshot of MD simulation. The yellow, red, and blue colors represent the electrode, ions and the solvent molecults, respectively. Z=0 corresponds to the lower electrode.

Near each electrified slit pore, we placed small partial charges on a plane at a position 0.7 Å away from the slit surface to produce the desired surface charge density, in accordance to the quantum mechanical calculations.[69] The number of K^+ ions inside the slits was chosen to ensure the overall electro-neutrality of the system. To obtain an MD system in which the chemical potential of water molecules inside the slit is equal to that in bulk solution, we first connected the slit to a large water bath whose one end was exposed to vacuum and performed NVT simulations (T = 300 K) for 3-10 ns for the number of water molecules inside the slit to allow for complete equilibration. During these simulations, "ghost" gate atoms, which do not interact with water molecules, were placed at the entrance/exit of the slit pore to prevent K^+ ions from leaving the slit. Next, the water bath was removed and periodical boundary conditions were enforced in all three directions. To remove the periodicity in the direction normal to the slit wall, the simulation box size in this direction was extended to be 3 times of the slit width, and the slab-PME method was used to compute the electrostatic interactions. The simulations

were performed for 100 ns and the trajectories were saved every 10 ps for analysis. The force fields for water and K^+ ions were taken from Ref. [70], and the force field for carbon atoms was taken from the sp^2 carbon of the force fields in Ref. [71]. Other simulation details can be found in Ref. [28].

4.2 Water/Ion Distributions inside Micropores

We investigated the distribution of water molecules and K^+ ions in electrified slit micropores with pore width (W) ranging from 9.36 Å to 14.7 Å. In each MD system, the pore wall is modeled by a single graphene layer, and the pore width is defined as the separation between the center planes of two graphene layers. The coordinate system is chosen so that $z = 0$ corresponds to the center plane of the lower wall. The surface charge density (σ) was fixed at -0.055 C/m^2, similar to that measured for microporous activated carbon electrodes immersed in aqueous electrolytes.[16, 72] Only counter-ions (K^+ ions) were included in the pores because co-ions are essentially rejected from these highly charged micropores.

Figure 4.2a shows the water and K^+ ion concentration profiles in negatively charged slit pores with various pore widths. The water distribution inside the slits changes as the width decreases: three layers of water molecules can be identified in slits with W > 10.7 Å while only two layers of water molecules develop in slits with W ≤ 10.7 Å. In the widest slit studied (W = 14.7 Å), the K^+ ion concentration profile resembles that expected from the classical EDL theories to some extent, i.e., counter-ions accumulate in

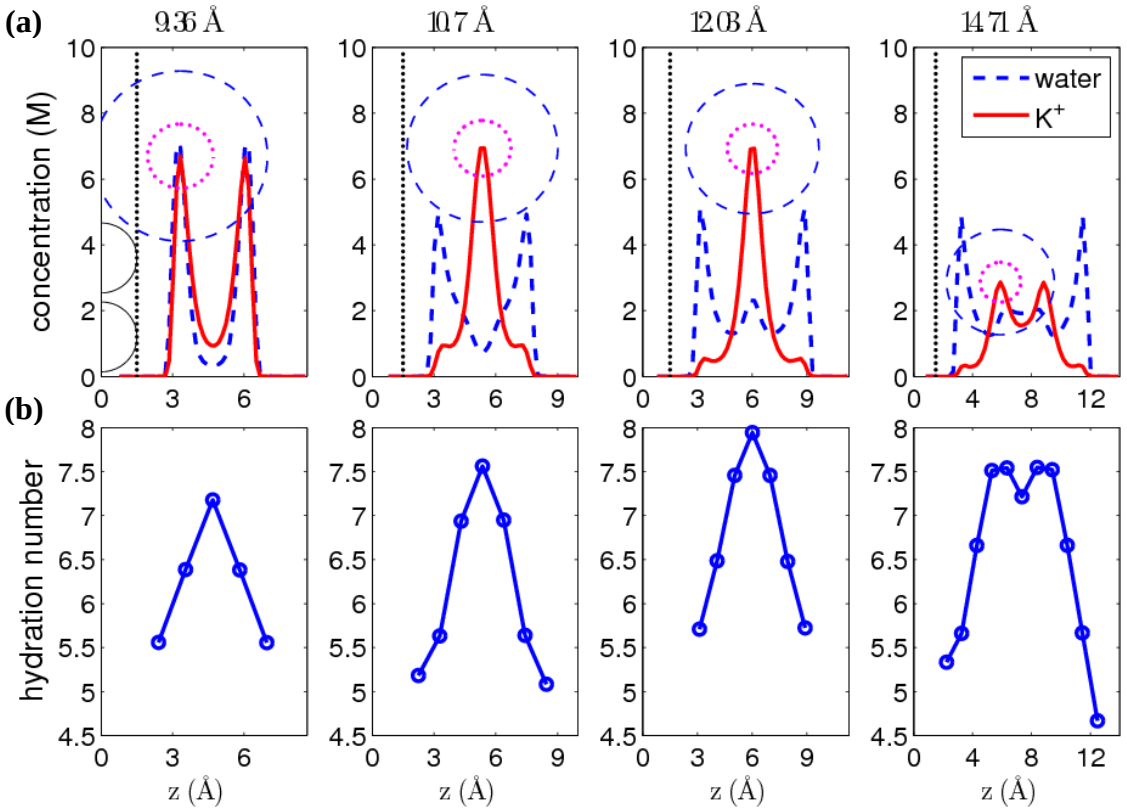

Figure 4.2: (a) Concentration profiles of water and K^+ ions inside slit pores with various widths. For clarity, the water concentration has been divided by a factor of 30. The concentric circles denote the size of bare and hydrated K^+ ions. The hemi-circles in the leftmost figure denote the van der Waals radius of the wall atom and the dashed lines denote the effective boundary of the lower wall. (b) Hydration number of K^+ ions across slit pores with various widths. All slit walls have the same surface charge density of $\sigma = -0.055 C/m^2$.

separate layers near *each* slit wall. However, in slits between 10 Å and 14.7 Å, K^+ ions accumulate primarily in the central plane of the slits, which is in disagreement with the classical EDL theories. Finally, in slits with W = 9.36 Å, the K^+ ion concentration profile shows one distinct peak near each slit wall, again in qualitative agreement with the classical EDL theories. However, K^+ ions in each peak adjacent to the slit wall is partly de-hydrated as inferred from the size of K^+ ion (shown as circles in Figure 4.2a) and from

the water concentration distribution in the slit. Therefore, the K^+ ions become contact-adsorbed in slits with W = 9.36 Å. The ion distribution in the pore size ranging from 10 to 14.7 Å is the focus of the present study.

4.3 Physical Origins of the Water/Ion Distributions

To understand the qualitatively different distributions of K^+ ions in different slits, we note that the distribution of counter-ions in electrified micropores free of co-ions are governed by mainly five factors:[73] (1) the long-range electrostatic ion-ion repulsion, which always drives ions towards the two slit walls (Figure 4.3a),[74] (2) the non-electrostatic ion-slit wall attractions that consist of the van der Waals and steric interactions between ion and wall atoms (Figure 4.3a), (3) the hydration of ions, which drives ions towards positions where they maximize interactions with their hydration water molecules (Figure 4.3b), (4) the interactions between an ion's hydration water molecules and their surrounding water molecules (Figure 4.3c),[75] and (5) entropic effects that drive the ion and water inside slit towards uniform distribution (Figure 4.3d). These factors insure that the free energy of the entire system (ion *and* water) is minimized at equilibrium. The significance of some of these factors in controlling the EDL structure has been recognized in the literature. For example, electrostatic ion-ion repulsion and the entropy of ions are accounted for in the classical EDL theories,[29] and recent theoretical and modeling works confirm that ion hydration and non-electrostatic ion-wall interactions cannot be neglected in describing the EDL.[31-35] However, many

details of these factors remain unexplored. First, ion hydration in electrified micropores remains rarely understood. Prior EDL studies were performed within the framework of a primitive model in which water is modeled as LJ atoms,[76] and thus ion hydration is not modeled with sufficient details. This limitation is avoided in the more recent atomistic studies of EDLs, but these studies deal with mesopores in which water layers from opposing walls do not interact, which is fundamentally different from the picture illustrated in Figure 4.2.[31-35] The hydration of ions in cylindrical micropores has been studied recently due to its relevance to biological ion channels.[37-38] However, how ion hydration across electrified slit pores varies as the slit shrinks, which is critical for understanding the EDL capacitance in micropores, has not been explored. Second, the enthalpic and entropic contributions of water to the free energy of the system and their role in controlling the EDL structure are often neglected. Several theoretical models have been proposed to account for these effects,[77-78] but these theories have not been applied to EDLs in micropores yet. Finally, the interplay and relative importance of the above-mentioned five factors in determining the EDLs in micropores have yet to be explored. For example, it is unclear whether the ion-ion electrostatic interactions or the ion hydration effects are the most important factor to determine the ion distribution in slit micropores. Below we show that these unexplored aspects of the EDLs are critical for understanding the different K^+ ion distributions in slits of different widths.

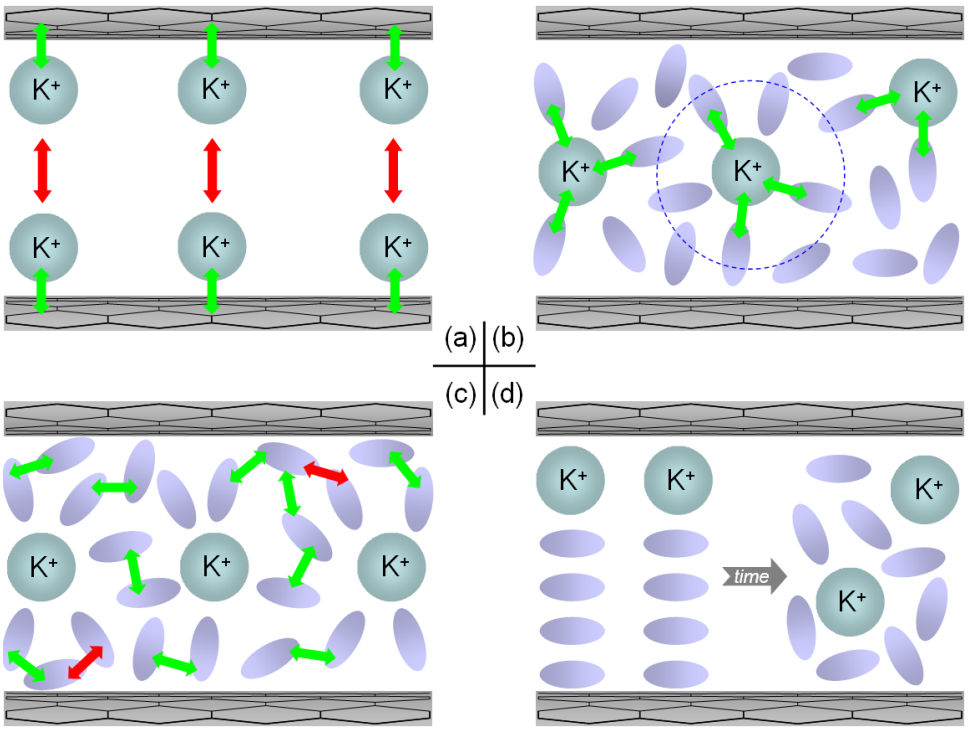

Figure 4.3: Schematic diagrams of the five factors, as described in the text, governing the distributions of the K^+ counter-ions in electrified slit-shaped micropores: a) the long-range electrostatic ion-ion repulsion which drives ions toward the slit walls (factor 1) and the non-electrostatic ion-slit wall attraction (factor 2), indicated by the red and green double-headed arrows, respectively (color codes also applicable in the following); b) the hydration of ions (factor 3), which drives ions toward positions to maximize their interactions with the hydration water molecules (the blue dashed circle indicates the primary hydration shell of one ion; compared to the ions in the slit center, the ion near the slit wall has smaller number of hydration water molecules); c) the interaction between an ion's hydration water molecules with their surrounding water molecules (factor 4); and d) entropic effects that drive the ordered distribution shown on the left toward a uniform/disordered distribution on the right (factor 5).

We examine the role of the above factors in determining the K^+ ion concentration shown in Figure 4.2a. To examine the role of ion hydration effects, we computed the number of hydration water molecules (hydration number, N_{hyd}) for K^+ ions across various slits (Figure 4.2b). Following established conventions, the water molecules belonging to the solvation shell of a given ion are defined as those within r_{min1} from the ion, where

r_{min1} = 3.65 Å corresponds to the first local minimum of the K^+-water pair correlation function.[70] In slits with W = 14.7 Å, as a K^+ ion moves away from the slit wall, N_{hyd} increases sharply and reaches a maximum of 7.5 at position 5.8 Å from the slit wall, exactly where the K^+ ion concentration peak is located. In slits with W = 10.7 and 12.03 Å, N_{hyd} increases monotonically from the slit wall to the slit center, and the K^+ peak again is located at a position where N_{hyd} is maximized. These results suggest that the ion hydration effects play an important role in determining the K^+ ion distribution in slit pores. For wide pores (or open electrodes) in which accumulation of ions occurs near each slit wall, the ion hydration effects are known to control the location of the concentration peak of small cations.[29] For pore widths in the 10 to 14 Å range, the ion hydration shells play an even more decisive role in the qualitatively breakdown of the classical EDL picture, i.e., they force K^+ ions to form a single layer at the midway between the slit walls. However, it is interesting that, in pores with W = 9.36 Å, the K^+ ion distribution shows an abrupt transition, i.e., K^+ ions form distinct layers near *each* slit wall, although the ion hydration effects should still drive them to the slit center. The most straightforward reason for this transition is that the electrostatic ion-ion repulsions dominate over the hydration effects for this pore since the ion-ion repulsion strengthens as the slit width decreases.

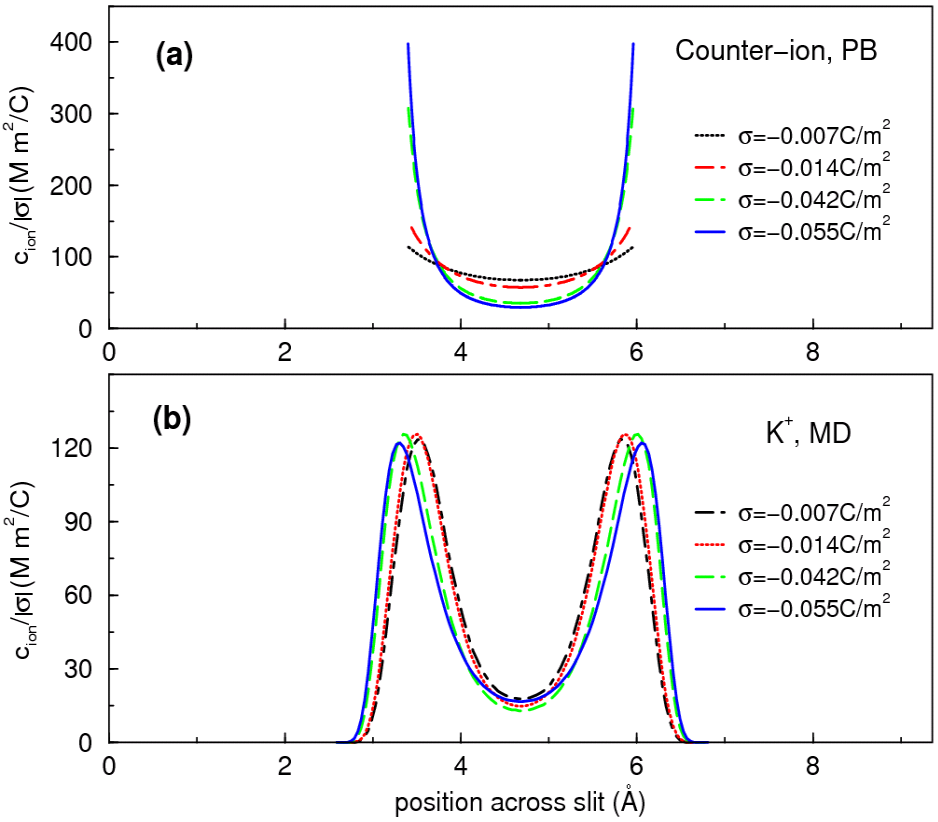

Figure 4.4: Variation of counter-ion (K^+ ion) concentration scaled by the slit wall charge density (cion/|σ|) in 9.36 Å-wide slits with different surface charge densities. (a) Prediction by the PB equation. The closest approach of the K^+ ion to the slit wall was taken as 3.3 Å. The solution dielectric constant was taken as 3.33, same as the result of fitting the sandwich capacitor model (in Figures 4.5 and 4.6) to the capacitance data obtained from micropores immersed in 6 M KOH electrolytes.[16] (b) Predicted by the MD simulations.

To elucidate whether the electrostatic ion-ion repulsion is indeed responsible for the formation of separate counter-ion layer near each wall instead of a single layer in the center of the 9.36 Å pore, it is desirable to compare the difference in electrostatic ion-ion interaction energy in the two different ion configurations. However, since the ion distribution is obtained in only one of these configurations, such a comparison is difficult to perform. Here we adopted a different approach, i.e., we performed PB and MD

simulations with different surface charge densities σ to probe the role of electrostatic ion-ion repulsion. If the electrostatic ion-ion repulsion dominates the ion distribution, as σ increases, the counter-ion concentration near the slit wall will increase more quickly than σ. For example, Figure 4.4a shows that, as σ increases from -0.007 C/m^2 to -0.055 C/m^2, the maximum ion concentration in the slit scaled by |σ|, i.e., $c_{max}/|\sigma|$, increases by a factor of 3.5, according to the classical PB simulations which contains mainly the electrostatic ion-ion repulsion. However, Figure 4.4b shows that for the same range of σ, MD simulations gave $c_{max}/|\sigma|$ values that are nearly independent of σ. More importantly, at σ = -0.007 C/m^2, our MD system contains only one K^+ ion in each simulation box, thus the electrostatic ion-ion repulsion does not even exist in such an MD system. These results indicate that the electrostatic ion-ion repulsion is not the reason for the contact-adsorption of K^+ ions on the slit wall in slits with W = 9.36 Å.

Since entropic effects are unlikely to cause the distinct K^+ ion peaks near slit walls,[79] we next examine whether non-electrostatic ion-electrode interactions and interactions between hydration water molecules (i.e., factors 2 and 4 above) dominate over the ion hydration effects so that K^+ ions prefer to become contact-adsorbed on the slit wall than accumulate in the slit center to maximize their hydration. Specifically, we calculate factors 2, 3, and 4 for the K^+ ions contact-adsorbed on the slit wall and located at the slit center in slits with W = 9.36 Å. To understand the interplay between these factors in larger pores, the same calculations were also performed in a slit with W = 12.03 Å. In all calculations, for an ion located at each position, we computed the interaction energy between the ion and its hydration water molecules or wall atoms, i.e., E_{hyd} and

$E_{ion\text{-}wall}$. We also computed $E_{water\text{-}water}$, the average interaction energy between each of an ion's hydration water molecules with its primary coordination water molecules (i.e., those water molecules within r_{min1} from the hydration water molecule being examined, where r_{min1} = 3.30 Å is the first local minimum of the water-water pair correlation function).[70] The results are summarized in Table 4.1.

Table 4.1: Properties of K^+ ion located at different positions inside slit pores and the properties of their hydration water molecules.

	In slit with W = 9.36 Å		**In slit with W = 12.03 Å**	
Ion location in slits	3.30 Å	4.68 Å	3.30 Å	6.02 Å
Interaction energy between K^+ ion and its hydration water (kJ/mol)	-294.4	-346.1	-296.0	-336.1
Non-electrostatic (LJ) ion-wall interaction energy (kJ/mol)	-7.42	-5.35	-6.55	-1.97
Coordination # of K^+ ion's hydration water	4.29	3.96	4.21	4.50
Interaction energy between each of K^+ ion's hydration water molecules with their coordinate water (kJ/mol)	-37.6	-32.1	-35.1	-42.5

Table 4.1 shows that in the slit with W = 9.36 Å, we observe that, as a contact-adsorbed K^+ ion moves to the slit center, E_{hyd} decreases by 51.7 kJ/mol. This is consistent with the increase of N_{hyd} shown in Figure 4.2b and indicates that the ion hydration effects favor the accumulation of ions in the slit center. At the same time, $E_{ion\text{-}wall}$ increases by

2.07 kJ/mol, which favors the contact-adsorption of K^+ ions. To test the significance of this effect, we performed a simulation in which the energy well depth, ε_{k^+-wall}, of the Lennard-Jones potential describing the non-electrostatic ion-wall interactions was reduced to 1/3 of its original value with all other interaction parameters unchanged. The K^+ ion concentration profile in the new simulation was similar to that shown in Figure 4.2a, indicating that the contribution of the non-electrostatic ion-wall interactions to the contact-adsorption of K^+ ion on the slit wall is modest. In the same slit, Table 4.1 also shows that, as a contact-adsorbed K^+ ion moves to the slit center, the average coordination number of its hydration water molecules reduces from 4.29 to 3.98, and the average interaction energy between each of the ion's hydration water molecules with its primary coordination water molecules increases by 5.5 kJ/mol. These results indicate that as a contact-adsorbed K^+ ion moves to the slit center, although it attracts more water molecules toward it to become better hydrated (thus lowering the system energy), it also causes its hydration water molecules to interact with fewer water molecules and therefore to weaken these interactions (thus increasing the system energy).

Summarizing the above discussions on the role of electrostatic ion-ion repulsion and non-electrostatic ion-wall attraction, we conclude that, for slit with W = 9.36 Å, the enthalpic effects associated with the interactions between hydration water molecules and their coordinate water dominate over the ion hydration effects and play a critical role in causing the contact-adsorption of K^+ ions on the slit wall. Similar analysis of Table 4.1's data for slit with W = 12.03 Å indicate that these enthalpic effects act *together* with the ion hydration effects to drive the K^+ ions from the slit wall to the slit center. Although the

$E_{ion\text{-}wall}$ difference works against this explanation, it is only a minor effect for K^+. It is noteworthy that the computed E_{hyd} for K^+ at the pore center for the 12.03 Å slit is close to the experimental value of K^+ in aqueous solution (331.8-338.1 kJ/mol).[80]

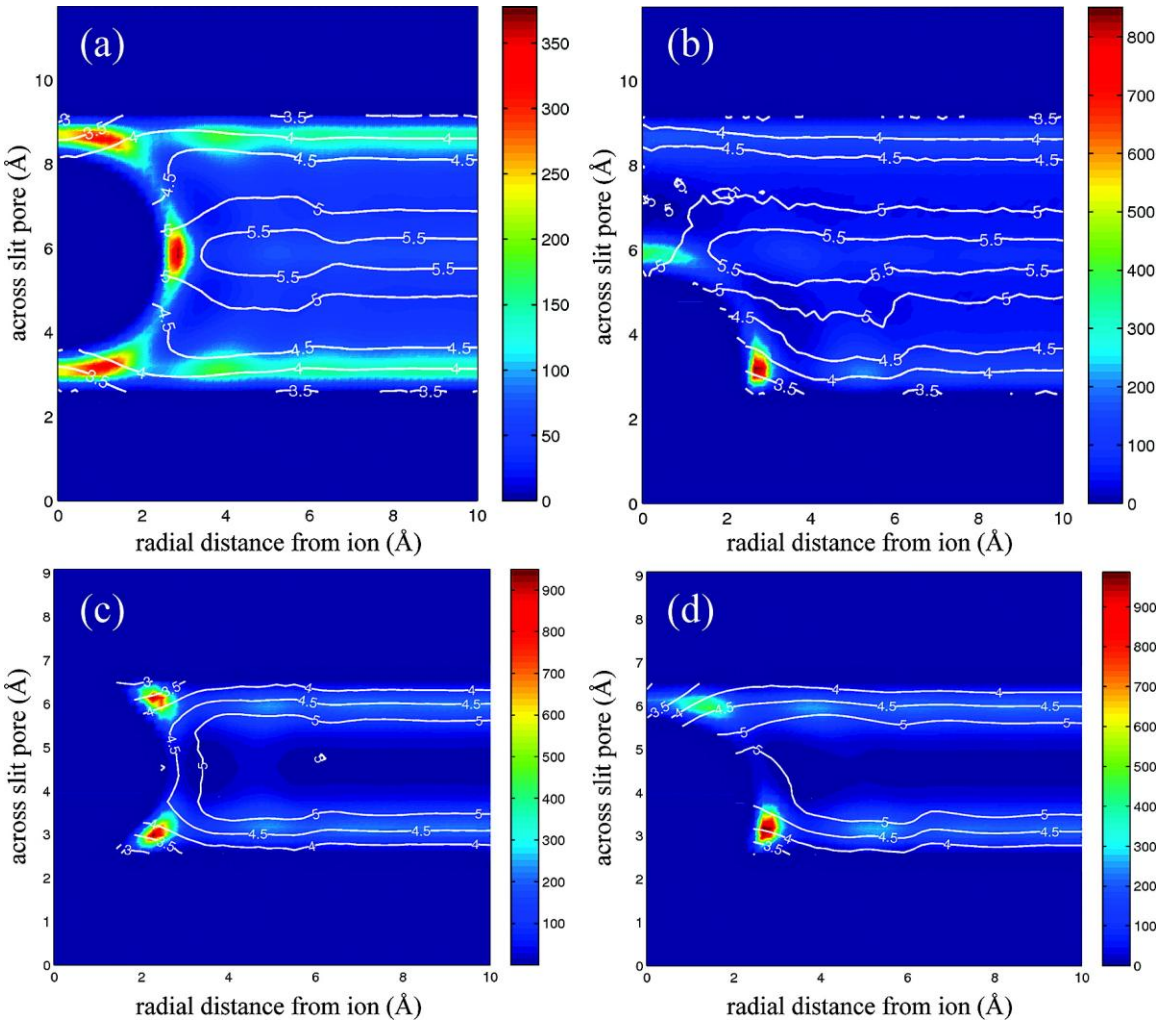

Figure 4.5: Distribution of water molecules around K^+ ion located at different positions in slit pores (shown as different colors) and the coordination number of these water molecules (shown as contour lines). (a) K^+ located at z = 6.03 Å inside a 12.03 Å-wide slit pore, (b) K^+ located at z = 3.30 Å inside a 12.03 Å-wide slit pore, (c) K^+ located at z = 4.68 Å inside a 9.36 Å-wide slit pore, (d) K^+ located at z = 3.30Å inside a 9.36 Å-wide slit pore.

To further understand the origins of the opposite role of these enthalpic effects on affecting the K^+ distribution in slits with different widths, we compute the distribution of water around K^+ ions located at the above two positions in the two slit pores. Parts a and b of Figure 4.5 show the concentration distribution (shown with different colors) of water molecules around K^+ ions contact-adsorbed on the slit wall and located at the slit center for a slit with W = 12.03 Å. The number of coordination water molecules for the water molecules located at different position from the K^+ ion is also shown in the same figure as contour lines. We observe that, when a K^+ ion is located at the slit center, its hydration water molecules are distributed near its equator and north/south poles. The hydration water molecules near its equator have a coordination number of 5-5.5, and those near its north/south poles have a coordination number of 3.5-4. As the K^+ ion becomes contact-adsorbed on the slit wall, its hydration water molecules accumulate mainly near its equator and their coordination number is ~3.5. The observed different solvation of the hydration water molecules of K^+ ion by other water molecules is consistent with that shown in Table 4.1, and is a result of the geometrical confinement and the layering of water inside slit. Specifically, when a K^+ ion is located in the slit center, there is enough space above/below it to accommodate a water layer between its north/south pole and the slit wall, and the hydration water molecules located there are not well solvated since there is no water above/below them. On the other hand, the hydration water molecules near the K^+ ion's equatorial plane are well solvated. When a K^+ ion is contact-adsorbed on the wall of the same slit, its hydration water molecules accumulate primarily near its equator because water concentration there is higher due to the layering of water shown in Figure

4.2a. Similar to the hydration water molecules near the north/south pole of the K^+ ions located at the slit center, these hydration water molecules are not well solvated. Overall, in slits with W = 12.03 Å, the solvation of K^+ ion's hydration water molecules is better when the K^+ ions are located in the slit center than when the K^+ ion is contact-adsorbed. Parts c and d of Figure 4.5 show the concentration distribution of water molecules around K^+ ions contact-adsorbed on the slit wall and located at the slit center for slit with W = 9.36 Å and their coordination number. When a K^+ ion is located in the center of this slit, essentially all its hydration water molecules are distributed near its north and south poles and are not well hydrated (average coordination number: 3.5-4). As the ion becomes contact-adsorbed on the wall, a large fraction of its hydration water molecules is distributed near its equator and it is not well hydrated (average coordination number: ~4). However, because the gap between the K^+ ion and slit wall is wide enough, some of its hydration molecules are distributed near its north pole and have an average coordination number of 4-4.5 due to the high water concentration near the upper slit wall. Therefore, in a slit with W = 9.36 Å, the solvation of K^+ ion's hydration water improves when the ion becomes contact-adsorbed.

4.4 The Sandwich Model

The above results indicate that, under slit surface charge density relevant to ECs based on microporous carbon electrodes, K^+ ions will form a single layer midway between the opposing slit walls in slit pores between 10 and 14.7 Å wide. Since the

micropore capacitance has been measured experimentally, it is desirable to compute the slit pore capacitance directly using MD simulations. A key difficulty associated with the present models for slit pores is that all charges are localized at different points determined by the atomic nuclei instead of being distributed continuously in the space according to the electron densities. This problem needs to be addressed to accurately predict the pore capacitance in pores where opposing pore surfaces share ions.[15] To circumvent this difficulty, here we propose a sandwich capacitance model to describe the capacitance of slit-shaped micropores and fit the experimental capacitance values of microporous carbons.

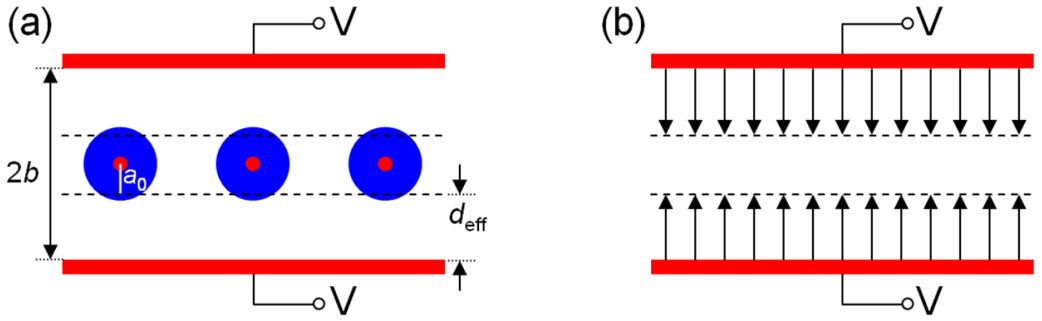

Figure 4.6: (a) Schematic of a sandwich capacitor formed by a layer of counter-ions located exactly midway between two electrodes with the same polarity and separated by W = 2*b*. (b) The equivalent system shown with the electric field lines. The locations of the dashed lines indicate the effective ion radius a_0 of the counter-ions, which is dictated by the spread of electron cloud (Ref. [15]). The effective separation between the electrode surface and the counter-ions is d_{eff}.

On the basis of the insight obtained from the above MD simulations, we derive a capacitance formula for a sandwich capacitor formed by a layer of counter-ions located exactly midway between two electrodes with the same polarity and separated by a pore width of 2*b* (Figure 4.6). Because the opposing electrodes share the net charge of the

counter-ions, one can approximate the slit capacitor as two capacitors in parallel as shown in Figure 4.6b. The total capacitance C_{tot} of the system shown in Figure 4.6b can thus be computed as

$$C_{tot} = 2C_s \tag{4.1}$$

where C_s is the capacitance of a single capacitor consisting of one electrode and one side of the counter-ions. Since the electric field lines effectively terminate at the electron cloud of the ions, C_s can be computed using the parallel-plate capacitor model

$$C_s = \varepsilon_r \varepsilon_0 A / d_{\text{eff}} \tag{4.2}$$

where ε_r is the electrolyte dielectric constant, ε_0 the permittivity of a vacuum, A the surface area of the electrode, and d_{eff} the effective separation between the electrode surface and the counter-ions. Counter-ions are not simply point charges and the ionic radii are determined by the location of the charge densities.[15] We stress that the corrections of charge separation by the locations of charge densities are extremely important in producing a reliable capacitance model, especially for micropores. Based on Figure 4.6b, d_{eff} is equal to (b-a_0), just as described in the EWCC model. However, the present model is derived for parallel plates, i.e. curvature is null. Therefore, the area-normalized total capacitance of the system shown in Figure 4.6 is obtained as

$$C_{tot}/2A = C_s/A = \varepsilon_r \varepsilon_0 / (b\text{-}a_0) \tag{4.3}$$

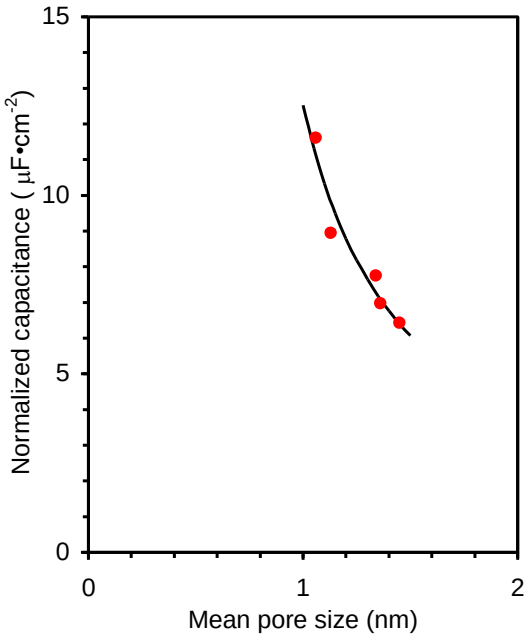

Figure 4.7: Experimental data in Ref. [16] of microporous activated carbon electrode materials in a 6 M aqueous KOH electrolyte fit by the sandwich capacitance model shown in Equation 4.3.

As can be seen in Figure 4.7, for the microporous activated carbon electrodes immersed in 6 M KOH electrolyte solution, the area-normalized capacitance of has been found to increase from ~6 to 12 μF/cm^2 as the mean pore size of the electrode decreases from 14.5 to 10.6 Å.[16] This pore size range is in rough agreement with that we found by MD simulations where fully hydrated K^+ ions accumulate primarily in the central plane of the slit pores. Using the sandwich capacitance model given by Equation 4.3, we were able to fit the experimental data with a R^2 value of 0.926, reproducing the experimental trend and giving two fitting parameters of $\varepsilon_r = 3.33 \pm 0.57$ and $a_0 = 2.65 \pm 0.54$ Å. That the ε_r value is larger than the vacuum value of unity implies that the electrolyte ions are hydrated in the pore width range studied, which is supported by

Figure 4.2a. The ε_r value is smaller than those in the Helmholtz layer near isolated electrodes (typically less than 10),[2] and may originate from the extreme confinement of water in the micropores.[81-82] Even with the standard error of 0.54 Å considered, the a_0 value is not in very good agreement with the ion radius of K^+ (1.38 Å).[83] A similar fit realized using the EWCC model yields a R^2 value of 0.921 as well. However, in this case a_0 (1.64 Å) is found to be much closer to the ionic radius of K^+. This indicates that confinement effects (use of a_0 explicitly) are key in a qualitative description of the capacitance behavior for small pores (i.e. sharp increase with decreasing width), as is described in detail here. However, our fits also indicate that curvature effects are very important for a quantitative description of the capacitance value, especially when pore geometry is closer to that of a cylinder rather than that of a slit.

4.5 Conclusions

In summary, we have studied the distribution of K^+ ions in electrified slit-shaped micropores with pore widths ranging from 9.36 Å to 14.7 Å using MD simulations. We have examined in detail the five main factors that govern the distribution of K^+ ions in electrified micropores: (1) the long-range electrostatic ion-ion repulsion, which always drives ions towards the two slit walls, (2) the non-electrostatic ion-slit wall attractions, (3) the hydration of ions, which drives ions towards positions where they maximize interactions with their hydration water molecules, (4) the interactions between an ion's hydration water molecules and their surrounding water molecules, and (5) entropic

effects that drive the ion and water inside slit toward uniform distribution. The highlight of our results is that K^+ ions form a well-hydrated single layer in the center of negatively charged slit pores with pore width between 10 Å and 14.7 Å. Such an ion distribution differs qualitatively from the prediction by the classical EDL theories, and is caused primarily by the ion hydration effects. In slits with a width of 9.36 Å, the K^+ ions form separate layers near each slit wall. We found that the electrostatic ion-ion repulsion plays a minor role in such a transition. Instead, the enthalpic effects associated with the interactions between the hydration water molecules of the K^+ ion with their surrounding water molecules were found to lead to this interesting behavior. Based on the K^+ ion distribution observed in electrified slits with 10 Å < W < 14.7 Å, we proposed a sandwich model to predict the scaling of the slit pore capacitance as a function of its pore width. This model is shown capable of predicting the anomalous enhancement of capacitance that has been experimentally observed in micropores with similar widths. However, curvature effects are indispensable for a quantitative description of the experimental capacitance values, further implying that the microporous carbons in Ref.[16] have a local pore geometry that is closer to a cylinder shape rather than a slit one.

CHAPTER 5

EDLS IN ORGANIC ELECTROLYTES NEAR OPEN ELECTRODES

Since aqueous electrolytes in micropores have been explored in Chapter 4, it is reasonable to similarly study organic electrolytes in micropores as well. However, we found that less research has been done for EDLs in organic electrolytes even near an open surface. Therefore, the objective of this chapter is to investigate the structure, capacitance, and dynamics of the EDLs in an organic electrolyte near *open* surfaces using MD simulations, with an emphasis on the following aspects: (1) the role of ion solvation in determining the structure of the EDLs, (2) the adsorption of organic ions on the neutral/charged electrodes and the structure and dynamics of the interfacial solvents change as the electrode becomes electrified (3) the applicability of the classical EDL models to describe the ion distribution in EDLs, and (4) the relations between the structure and the capacitance of the EDLs and the electrode charge density (or potential).

5.1 Simulation Setup

Figure 5.1a shows a schematic of the simulation setup. 1.2 M $TEABF_4$ solution in the solvent of acetonitrile (ACN) was taken as the organic electrolyte, since such an electrolyte was used in experiments discovering the anomalous increase of capacitance in micropores [84]. For ions and solvent molecule in this organic electrolyte, the sketches of their structures are shown in Figure 5.1b. The static graphene sheets were taken as the electrodes between which there was a slab of organic electrolyte enclosed as shown in

Figure 5.1a. The separation between the geometric planes of the two electrodes was chosen as 3.9 nm. Although such a separation is much smaller than that in typical experimental studies, it is much larger than the EDL thickness near each electrode and therefore enables the EDLs at the two electrodes to be studied separately. Periodic boundary conditions were applied in the *xy* plane beyond the simulation box. The coordinate system was chosen such that the geometrical plane of the lower electrode corresponds to $z = 0$. The image planes of the two electrodes were placed at a position 0.08 nm from their geometrical planes (see Figure 5.1a).[85]

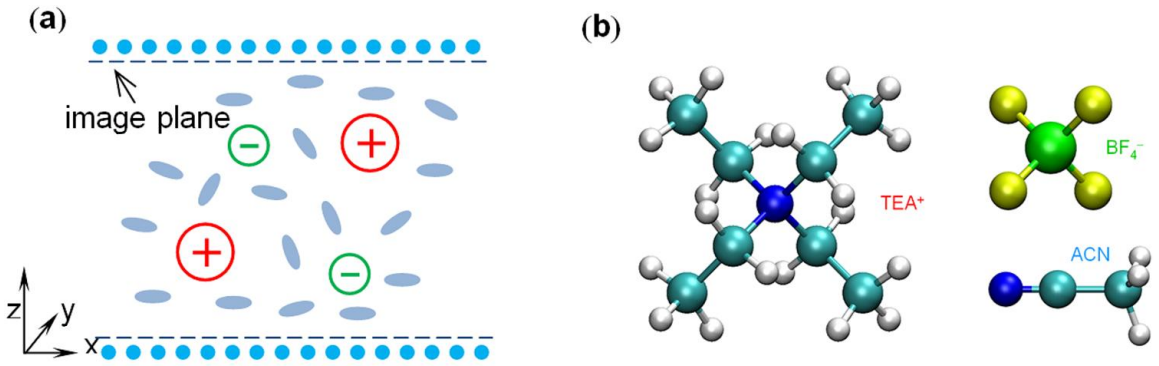

Figure 5.1: (a) A schematic of the simulation system. (b) Molecular models of the TEA^+, BF_4^-, and ACN molecules.

As described in Section 4.1, the partial charge uniformly distributed among the electrode atoms is a relatively easy way to model the charged electrode using MD simulation, which is according to the fact that the surface charge on the electrode surface results from the potential drop between the cathode and anode in an EC. However, this method neglects the polarizability of electrode surface, which is a strong assumption, because the polarizable electrode surface may make the charge inhomogenously

distributed on the electrode surface by changing the local interactions between electrodes and electrolytes due to the image charge effects. The method developed in Ref. [86] can be used to model the electrode with polarizable surface in MD simulation where the applied electrical potential can be enforced on the electrodes. However, this method of putting charge on electrodes needs quite less computational cost than that of directly applying potential on electrodes. Hence, the former technique is more often used for polarizable surface little affecting the EDL structure and capacitance, although the later was chosen in the work shown in this Chapter.

As shown in Figure 5.1a, the electrical potential on the lower electrode wall was fixed to zero, and an electrical potential was ramped up from 0.0 V to 2.7 V with a 0.3 V increment and applied on the upper electrodes in separate simulations. The largest potential difference, 2.7 V, is similar to the maximum operating voltage of ECs using similar electrolytes.[87-92] The number of ACN molecules in the system was chosen such that the ACN density at the central portion of the system did not differ by more than 5% from 14.5 M, i.e., the ACN density in a 1.2 M bulk electrolyte with the same composition. The number of ions in the system was tuned such that the ion concentration in the central portion of the MD system differs less than 15% from the target concentration of 1.2 M. Additional simulations at selected potential differences in which the ion concentration at the central position of the system was varied by up to 30% indicated that the EDL structure and capacitance are insensitive to the ion concentration in the central portion of the MD system. The force field for the electrode atoms (carbon) was taken from Ref. [71]. The force fields for the TEA^+ cations were taken from the

General AMBER force field (GAFF),[93] with atomic partial charges from Ref. [94]. The force fields for the BF_4^- anions and ACN molecules were taken from Ref. [95]. The force fields for ACN molecules yield a dielectric constant of 26.3 ± 0.3 at 298 K, in reasonable agreement with the experimental value of 35.8 at room temperature.[96]

Simulations were performed in the NVT ensemble. The system temperature was maintained at 298 K using the Berendsen thermostat with a time constant of 1.0 ps. The electrostatic interactions were computed using the PME method.[97] An FFT grid spacing of 0.11 nm and cubic interpolation for charge distribution were used to compute the electrostatic interactions in the reciprocal space. A cutoff distance of 1.2 nm was used in the calculation of electrostatic interactions in the real space. The non-electrostatic interactions were computed by direct summation with a cutoff length of 1.2 nm. The bond lengths of the TEA^+ and BF_4^- ions were maintained by using the LINCS algorithm,[98] while the bond angles and the dihedral angles were allowed to change. For each applied potential on the upper electrode, five simulations with independent initial configurations were performed. In each simulation, we started the simulation at 1000 K and then annealed the system gradually to 298 K in 2 ns. Following annealing, the system was simulated at 298 K for 3 ns to reach equilibrium. Finally, a 9-ns production run was performed.

As described in Section 3.2.2, getting the space charge density from MD simulations, we can obtain the potential distribution along the z-direction inside the channel solving Equation 3.4. Since we directly apply the potential, V, on the upper electrodes, the boundary conditions would be that (1) the potential on the lower image

plane was set as zero, i.e., $\phi(0)=0$, and (2) $\phi(L)=V$ on the upper image plane. Taking these two boundary conditions into Equation 3.4., the formula for calculating the potential distribution inside the channel is

$$\phi(z)=-\frac{1}{\varepsilon_0}\int_0^z (z-u)\rho_e(u)du+\frac{V}{L}z \qquad (5.1)$$

in which L is the distance between two opposite image planes where the upper and lower potentials are applied on, and is 3.74 nm in all channel simulations in this chapter.

5.2 Ion Solvation in Bulk Organic Solvents

Ion solvation plays a key role in determining the structure of EDL in aqueous electrolytes. It affects the position of the counter-ion concentration peak near the electrodes [28] and the dynamics of interfacial ions. It is reasonable to expect that ion solvation in organic electrolytes plays a similar role. Therefore, it is useful to first quantify the solvation of TEA^+ and BF_4^- ions in bulk solutions.

Explicit ion solvation is first quantified by the density distribution of ACN molecules around the ions. Figure 5.2a shows the ion−ACN and ion−ion radial distribution functions (RDFs) in a bulk solution of 1.2 M $TEABF_4$ in ACN. The TEA^+−ACN RDF indicates that the first peak is rather broad and the second peak is barely distinguishable from the first peak. This suggests that the solvation of TEA^+ cations by ACN molecules lacks a distinct structure of solvation shells compared to that observed for solvation of small inorganic ions in aqueous solutions.[26] The low value

and broadness of the first peak is caused by (1) the large size of the TEA^+ cations, which leads to weak electrostatic ion-ACN interaction, (2) the charge de-localization (i.e., the net charge of a TEA^+ cation is distributed among its many atoms) that weakens the electrostatic attraction between the ion and the ACN molecules near it, and (3) the irregular shape of the TEA^+ cations that prevents a dense packing of ACN molecules around them with a uniform distance to the center of TEA^+. The RDF for BF_4^-−ACN shows similar features, although the first peak becomes more distinct because of the smaller size and more spherical shape of the BF_4^- anions. The RDF radius of *ca.* 0.5 nm for the first solvation shell of BF_4^- anion indicates that the solvated ion diameter of BF_4^- is *ca.* 1 nm. When compared to the bare ion diameter of BF_4^- (4.6 Å),[83, 99-100] this solvated ion diameter yields a solvation shell thickness of *ca.* 0.5 nm, which is comparable to the dimension of one shell of ACN molecules according to a radial distribution of solvent molecules (see below). In addition, the solvated ion diameter of 1 nm is also in good agreement with the pore width of ≤ 1 nm necessary for the desolvation of BF_4^- anions in ACN according to the anomalous increase in capacitance in microporous carbons.[84, 101] The solvation numbers of the TEA^+ and BF_4^- ions, defined as the number of ACN molecules within the first solvation shell of the ions, were found to be 15.5 and 6.75, respectively. We note that, following traditional conventions, the extension of the first solvation shell is determined by the position of the first local minimum of the ion−ACN RDFs shown in Figure 5.2a.

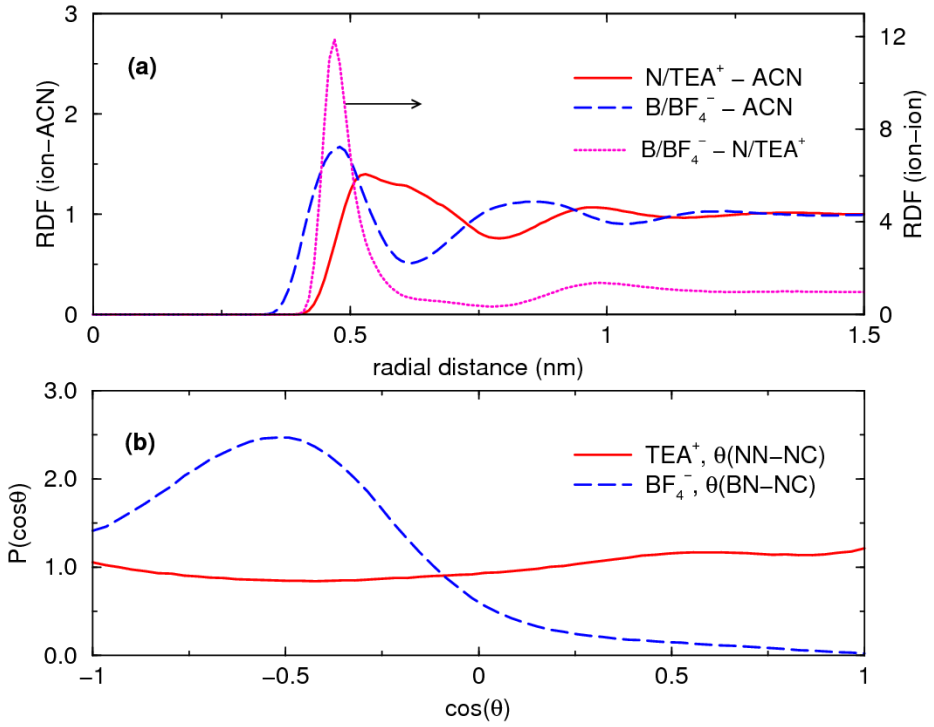

Figure 5.2: (a) Ion−ACN and ion−ion radial distribution function (RDF) in 1.2 M bulk $TEABF_4$/ACN solution. The radial distance is between the ion center, either N or B, and the center of mass of ACN molecules. (b) Distribution of the angle θ formed between the NC vector of the ACN molecules in the first solvation shell of TEA^+ and BF_4^- ions and the vector from the ion center, either N or B, to the N atom of the ACN molecules.

Figure 5.2a also shows the RDF for the TEA^+−BF_4^- ion pair, which has essentially one main peak located at 0.47 nm. On the basis of the bare ion diameter of TEA^+ (6.8 Å) and BF_4^- (4.6 Å) [83, 99-100] and the first peak location of the BF_4^-−ACN and TEA^+−ACN RDF curves, we can infer that TEA^+ and BF_4^- ions constitute a so-called "contact ion pair" in the solution. This is not surprising since the solvent does not effectively screen the electrostatic attraction due to the relatively small dielectric constant of ACN. The high RDF peak suggests that the correlation between TEA^+ and BF_4^- ions is

strong in ACN solutions. This correlation should affect the ion distribution inside the EDLs.[102]

The ion solvation is further quantified in Figure 5.2b by examining the orientational ordering of the ACN molecules in the first solvation shell of the TEA^+ and BF_4^- ions. We computed the distribution of the angle (θ) formed between the NC vector of ACN molecules within an ion's first solvation shell and the vector from the ion center, either N or B, to the N atom of the ACN molecules. The NC vector points from the N atom to the methyl group's C atom. Figure 5.2b shows that ACN molecules are nearly randomly oriented in the first solvation shell of TEA^+ cation, which is in sharp contrast with the strongly oriented water molecules near small inorganic ions.[26] The weak orientational ordering of ACN molecules around the TEA^+ cation originates from the large size and irregular shape of the TEA^+ cations. Figure 5.2b shows that the orientational ordering of ACN near BF_4^- anions, although still weaker than those of the water molecules near small inorganic ions, is stronger than that near the TEA^+ cations. Specifically, ACN molecules tend to align their NC vectors away from the BF_4^- anion at an angle of 60 º. The average NC vector orientation angle $cos\theta$ was found to be −0.51, which is close to that observed for ACN molecules near model anions with a net charge of −0.75 e and van der Waals diameter of 0.31 nm.[103]

In summary, the above results show that the solvation of TEA^+ and BF_4^- ions in ACN is characterized by the weak packing/orientational ordering of ACN molecules around the ions and a moderate solvation free energy. The solvation of both ions in ACN is much weaker compared to the solvation of small inorganic ions in aqueous solution.

Hence it is possible that organic ions can become partially desolvated at much weaker electrode polarization compared to that in aqueous electrolytes.

5.3 Structure and Capacitance of EDLs

5.3.1 EDLs near Electrodes at Potential of Zero Charge

Understanding the structure of the EDLs near electrodes at potential of zero charge (*PZC*) provides a baseline for describing EDLs near polarized electrodes. In addition, the insight gained from studying such EDLs facilitates the understanding of EDLs near weakly polarized electrodes, which is important in applications such as electrochemical sensing.

Figure 5.3a shows the concentration distribution of ACN molecules near the neutral electrode. We note that throughout this chapter, the positions of solvent molecules and ions are based on their center of mass. A significant layering of ACN molecules is observed near the electrode. The first layer of ACN molecules is found to occupy the region z = 0 to 0.56 nm (zone 1 in Figure 5.3a), and additional layers of ACN molecules are observed in region z = 0.56 to 1.1 nm (zone 2). At positions beyond about 1.1 nm from the electrode, the structure of ACN becomes bulk-like. The rich structure of ACN observed is caused mainly by the short-range solvent−solvent and solvent−electrode interactions and resembles the water structure near solid surfaces reported in numerous studies.[28, 104]

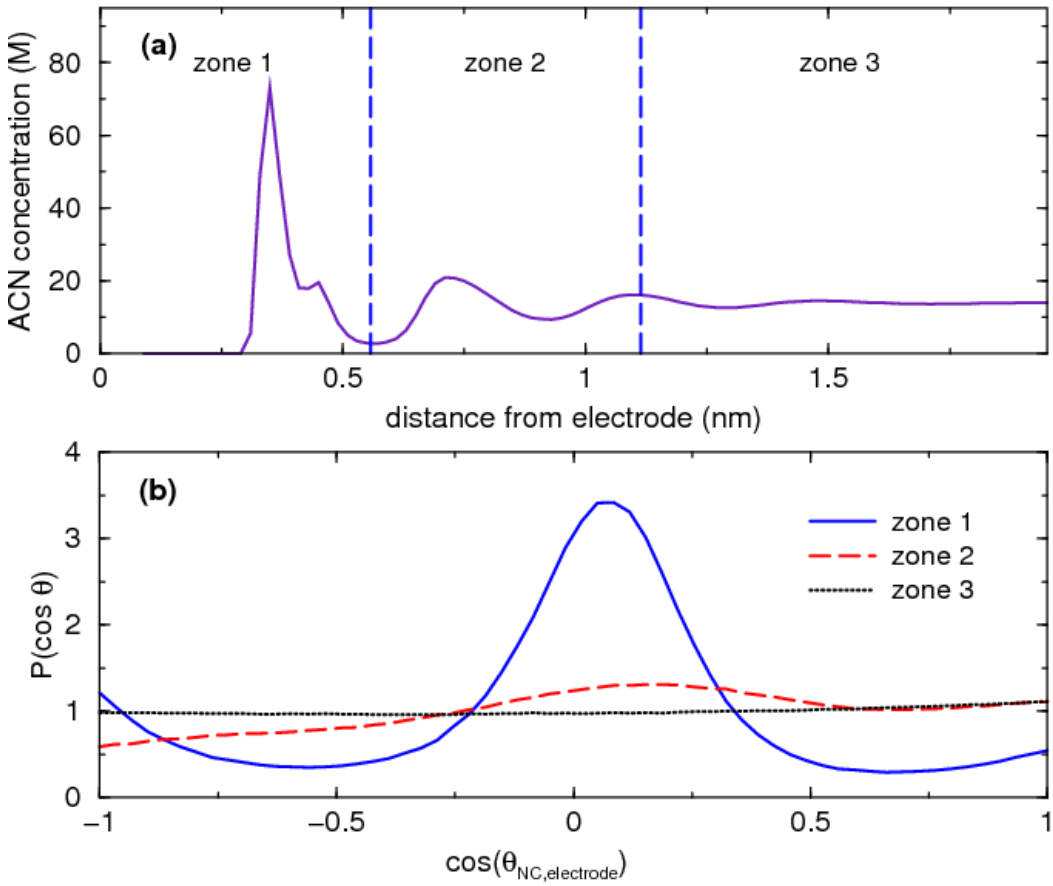

Figure 5.3: (a) Concentration distribution of ACN molecules near a neutral electrode. The position of ACN molecules is based on their center-of-mass. (b) Orientational distribution of the NC vector of ACN molecules (defined as the vector pointing from the N atom of an ACN molecule to the C atom of its methyl group) with respect to the normal direction of the electrode for ACN molecules at different distance from the electrode.

Figure 5.3b shows the distribution of the angle formed between the NC vectors of ACN molecules and the normal direction of the electrode for ACN molecules at different distances from the electrode. We observe that a majority of ACN molecules in the first ACN layer (zone 1) orient with their molecular axis parallel to the electrode surface. Since quantum processes such as bonding between ACN molecules and electrode atoms are not taken into account in our classical MD simulations, such an orientation is adopted

by the ACN molecules mainly to maximize their van der Waals interactions with the electrode. This preferential orientation is similar to the side-on adsorption mode of ACN molecules on an uncharged Pt surface, which are energetically more favorable than the end-on adsorption modes with the CN group pointing towards or away from the Pt surface.[105] Our results also complement the experimental findings inferred from the sum frequency generation (SFG) measurements of ACN orientation on Pt(111) surface.[106] In the experimental study, it was found that ACN molecules adopt an orientation with the CN group directed towards or away from the surface when the surface is positively or negatively charged, respectively. In comparison, ACN molecules do not have such preferred orientations at *PZC*,[106] and our simulations indicate that there is a preference for side-on orientations under this condition. Figure 5.3b also shows that the orientational ordering of ACN molecules is already weak beyond the first ACN layer. At a distance of 1.1 nm beyond the electrode, the ACN orientation approaches a random distribution. The penetration of ACN orientational ordering into the bulk electrolyte is *ca.* 0.3-0.6 nm shorter compared to that for ACN molecules near TiO_2 anatase (101) surfaces.[107] The shallower penetration in our system originates mainly from the weaker interactions between ACN molecules and the electrode atoms, which induce weaker ACN orientational ordering in the first ACN layer and thus weaker orientational ordering beyond the first ACN layer.

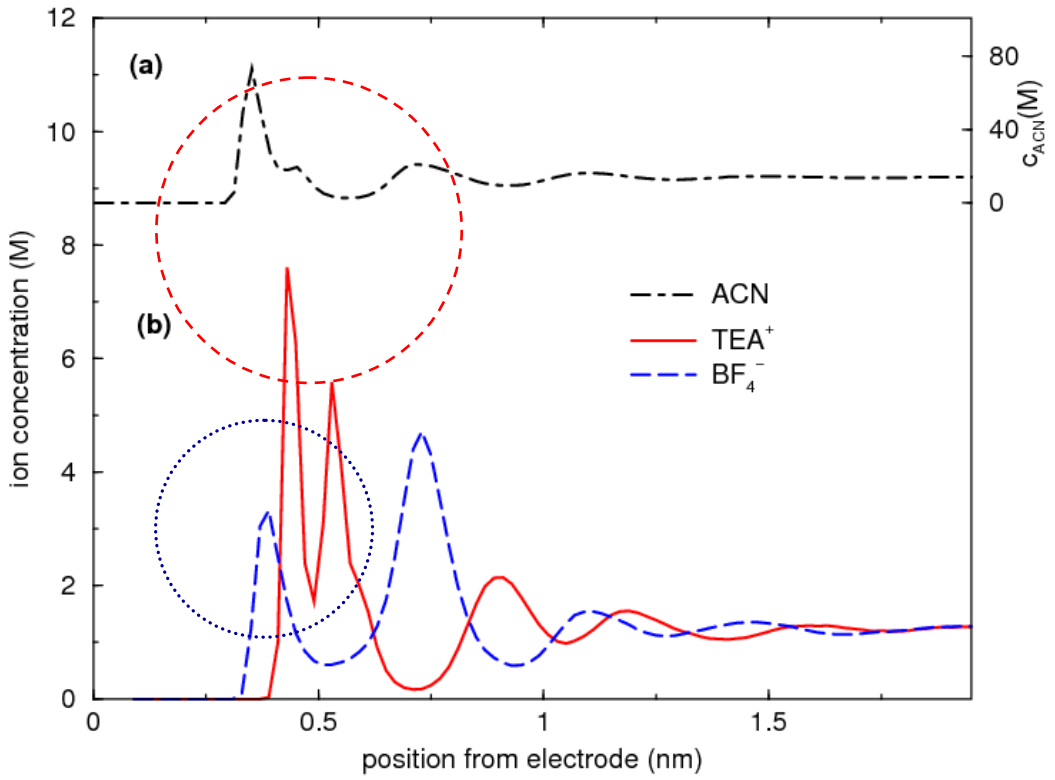

Figure 5.4: (a) and (b) Concentration distributions of ACN, TEA^+ and BF_4^- near a neutral electrode. Circles are bare ion diameters of the TEA^+ and BF_4^- ions.

Figure 5.4b shows the concentration distribution of TEA^+ and BF_4^- ions near a neutral electrode, and the circles in the figure illustrate the size of bare TEA^+ and BF_4^- ions (0.68 nm and 0.46 nm, respectively [83, 99-100]). For reference, the ACN concentration profile is shown in Figure 5.4a. As indicated by the twin-peaks located at z = 0.48 and 0.52 nm for the TEA^+ cation and the peak located at z = 0.46 nm for the BF_4^- anions, a large amount of TEA^+ and BF_4^- ions are adsorbed on the electrode. Based on the size of bare TEA^+ and BF_4^- ions (cf. the two circles in Figure 5.4) and the ACN concentration profile shown in Figure 5.4a, there are no ACN molecules between ions located in these peaks and the electrode, i.e., these ions are contact-adsorbed on the

electrode. This suggests that, even at zero electrode charge density, some ions can be adsorbed on the electrode and become partly desolvated. This phenomenon is similar to the adsorption of I^- and Cl^- ions onto a neutral electrode as observed in aqueous solutions,[25] but the contact adsorption of TEA^+ and BF_4^- ions is more noteworthy than for those small ions. The significant contact adsorption of the organic ions is due to several different factors.[86] First, the solvation free energies of these ions are not as high as those of the small inorganic ions, and thus it is easier for the ions to lose part of their solvation shell and become contact-adsorbed. Second, because of the large size of these ions, they will not lose a large fraction of their solvation shell, even upon contact adsorption. The TEA^+ and BF_4^- ions in the first peak near the electrode are found to lose *ca.* 30% and *ca.* 40% of their solvation shell, respectively. Finally, because of the large ion size and a large number of atoms in each ion, the non-electrostatic ion−electrode interactions (essentially the van der Waals attractions) are strong, which facilitates the adsorption of ions on the electrode.

Typical examples of the ubiquitous van der Waals forces are seen in nano-confined systems, such as the encapsulation of organic molecules in carbon nanotubes.[108-109] Figure 5.5 shows the potential energies of the TEA^+ and BF_4^- ions at different positions above a neutral electrode due to such interactions. The valleys of these potential profiles are deep (–89.3 and –17.8 kJ/mol for the TEA^+ and BF_4^- ions, respectively). For TEA^+ cation, the valley of potential energy profile even becomes comparable to the ion's solvation free energy, which means that the energy cost for the desolvation can be compensated by the non-electrostatic ion−electrode interaction. In

most double layer theories, the non-electrostatic ion-electrode interactions are neglected. However, the above results suggest that, for bulky ions, such interactions are major driving forces for the partial desolvation of ions as they move toward electrode, and must be considered in order to accurately predict the ion adsorption on the electrode. Figure 5.4b also shows that TEA^+ and BF_4^- ions form alternating layers near the electrode, which is not typically observed in aqueous media but is prevalent in RTILs.[62, 104] The alternating layers of cations and anions are caused by the strong correlation between these ions, as is evident in Figure 5.2a. Figure 5.6 summarizes the arrangement of ACN molecules, TEA^+, and BF_4^- ions near a neutral electrode.

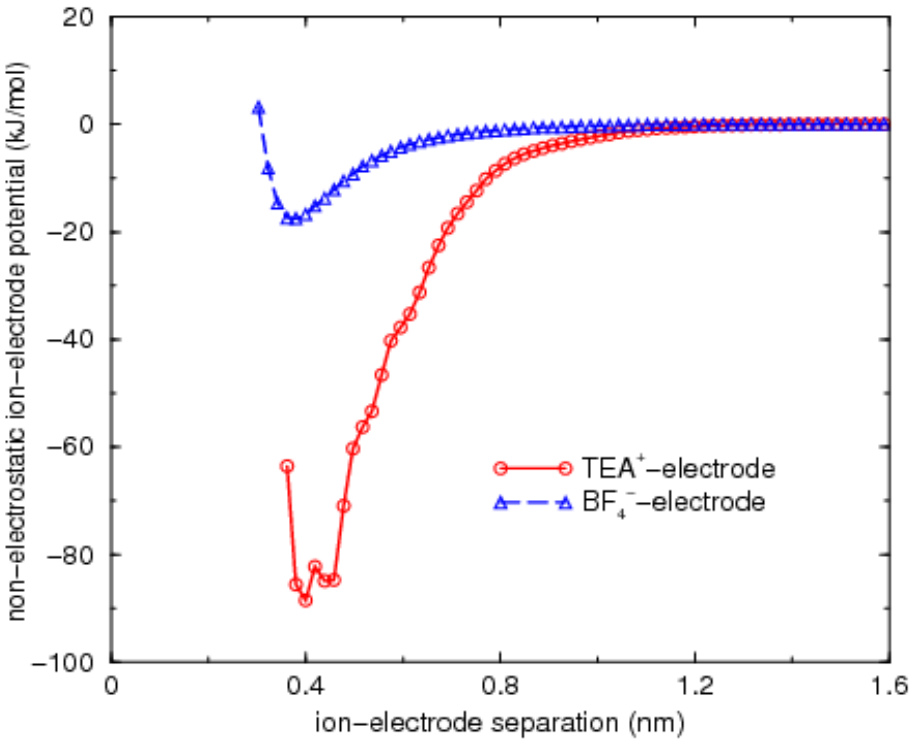

Figure 5.5: Potential energy of the TEA^+ cation and BF_4^- anion at different position above a neutral electrode due to non-electrostatic ion-electrode interactions.

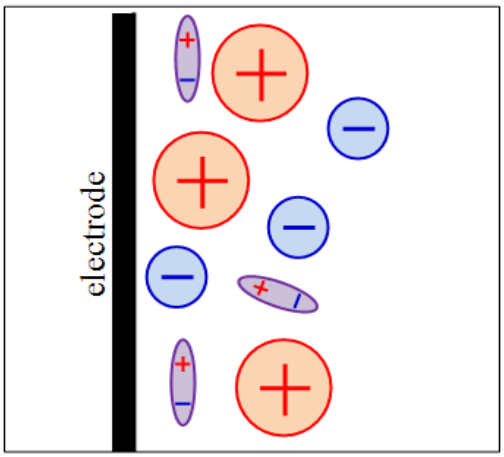

Figure 5.6: Schematic of the arrangement of ACN molecules, TEA^+, and BF_4^- ions near a neutral electrode. The ellipses denote ACN molecules.

We next study the charge separation and electrical potential distribution of the above EDLs. The space charge density profiles were computed from an MD trajectory and the electrical potential distribution was obtained by solving Poisson equation with the space charge density as input.

Figure 5.7 shows the space charge density and the electrical potential distribution near the neutral electrode. Although the alternating ion layers (see Figure 5.4b) suggest that there may be significant charge separation near the electrode, a careful examination of the space charge density near the electrode (see Figure 5.7a) shows that the space charge density due to the TEA^+ and BF_4^- ions largely cancels each other out in the 0.3−1.0 nm region. This is mainly due to the fact that, unlike simple ions such as Na^+ and Cl^-, the net charge of complex organic ions is distributed among their multiple atoms rather than localized at their center of mass. Further examination of the space charge density profiles (see Figure 5.7a) indicates the local space charge density is dominated by

the ACN molecules at most locations. The non-zero local space charge due to ACN molecules is caused by their preferential orientation near the electrode. Overall, a small potential difference of 168 mV develops between the electrode and the bulk electrolyte, which represents the *PZC* of the electrode/electrolyte system studied here.

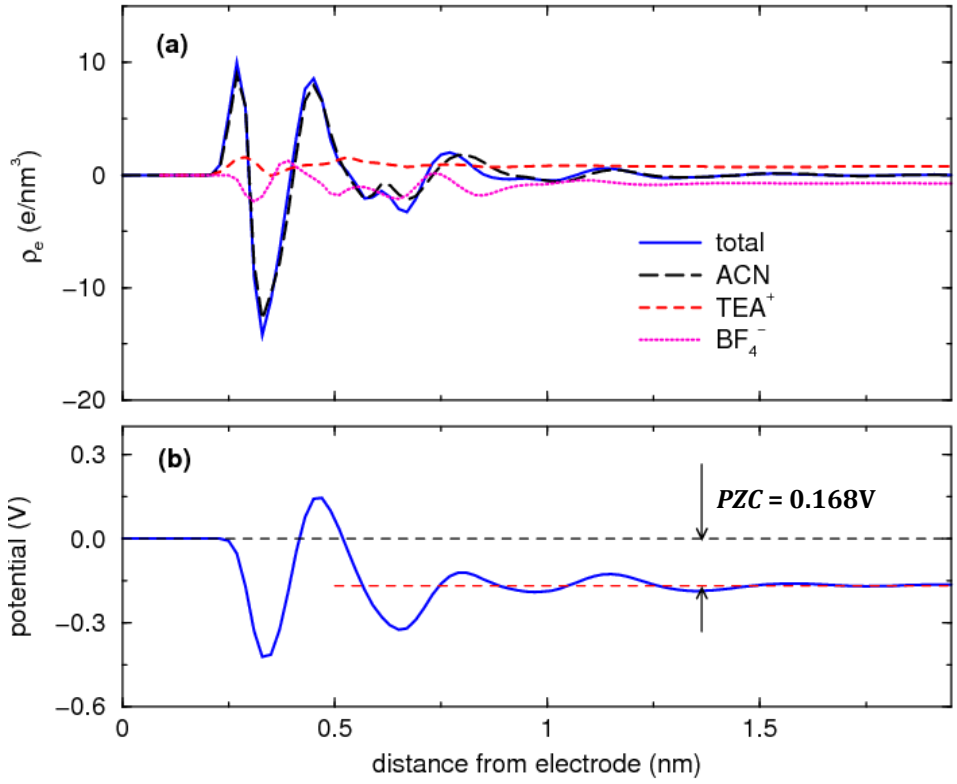

Figure 5.7: (a) Space charge density of ACN molecules, TEA^+ cations and BF_4^- anions. (b) Electrostatic potential distribution near a neutral electrode.

5.3.2 Structure of EDLs near Negative Electrodes

As the potential difference between the upper and lower electrodes increases, the electrode surface charge density increases. Here we focus on the EDLs adjacent to the

lower electrode at a potential difference of 0.9 V and 2.7 V, when the surface charge density on the lower electrode is −0.04 C/m^2 and −0.105 C/m^2, respectively.

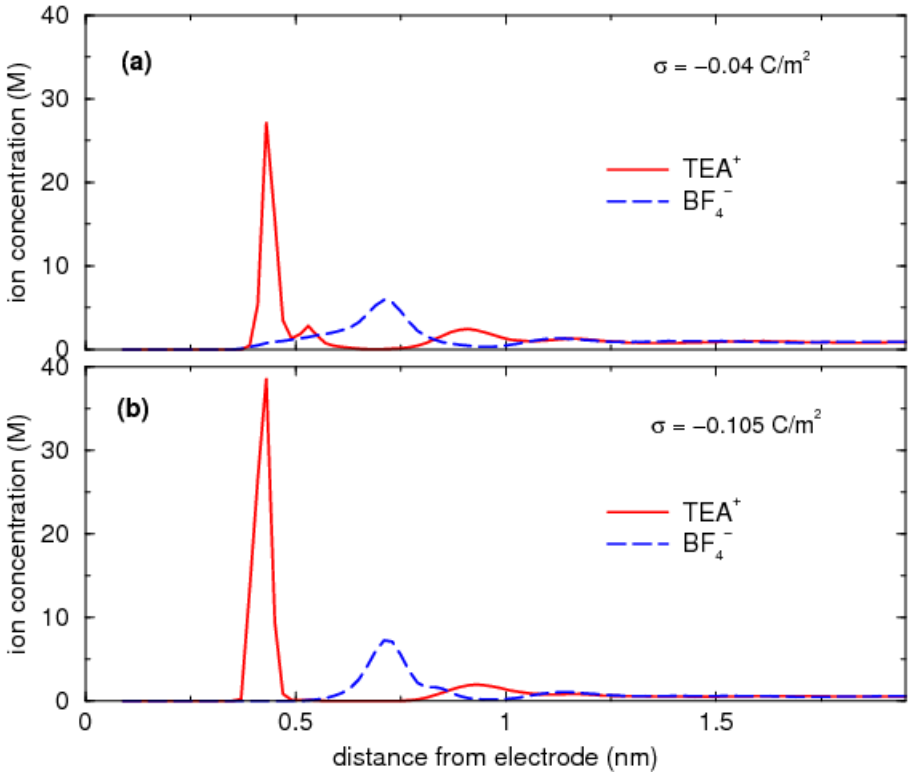

Figure 5.8: Concentration profiles of TEA^+ cations and BF_4^- anions near electrodes with charge densities of −0.04 C/m^2 (panel a) and −0.105 C/m^2 (panel b).

Figure 5.8a and Figure 5.8b show the concentration profiles of the TEA^+ cation and BF_4^- anions near the negative electrode at σ = −0.04 and −0.105 C/m^2, respectively. We observe that, as σ increases, more TEA^+ cations become contact-adsorbed, and the first TEA^+ concentration peak moves slightly towards the electrode. The accumulation of TEA^+ cations near the electrode is accompanied by the depletion of BF_4^- anions in the same region: contact adsorption of BF_4^- becomes minor at σ = −0.04 C/m^2 and vanishes at σ = −0.105 C/m^2. However, a large number of BF_4^- anions accumulate at a position of

0.72 nm from the electrode, and this BF_4^- peak is followed by a weak TEA^+ peak located at z = 0.92 nm. The alternating counter-ion/co-ion peaks are again caused by the strong association of BF_4^- and TEA^+ ions as shown in Figure 5.2a. The TEA^+ and BF_4^- ion concentrations become the same only when z > 1.1 nm.

The ion distributions shown in Figure 5.8 cannot be adequately described by the current classical EDL models. Even though the Helmholtz model predicts distinct counter-ion concentration peaks near the electrode similar to those found here, the Helmholtz model also indicates that the ion concentration becomes homogeneous beyond the first counter-ion peak, which contradicts the alternating counter-ion/co-ion peaks shown in Figure 5.8. In addition, the Helmholtz model specifies that the charge of the counter-ions within the Helmholtz plane exactly balances the net charge of the electrode, in sharp contrast to what we have found. To show this, we computed the "effective ion accumulation" (EIA) factor

$$EIA(z) = L_x L_y \int_0^z [\rho^n_{counter-ion}(s) - \rho^n_{co-ion}(s)]ds \qquad (5.2)$$

where *z* and *s* are the distance from the electrode, L_x and L_y are the size of the simulation box in the *x*- and *y*-directions, $\rho^n_{counter-ion}$ and ρ^n_{co-ion} are the number density of the counter-ion and the co-ion. *EIA*(*z*) indicates the difference between the number of counter-ions and co-ions in the space within position *z* from the electrode. The Helmholtz model predicts that *EIA*(*z*) reaches the number corresponding to the net charge (in unit of elementary charge) on the electrode at the Helmholtz plane and shows no change at other positions. The trend of *EIA*(*z*) is the same near electrodes with σ = −0.04 and −0.105

C/m^2, and we show only *EIA*(*z*) near the electrode with $\sigma = -0.105$ C/m^2 in Figure 5.9a. We observe that, at $z = 0.49$ nm (the right edge of the first TEA^+ concentration peak, see Figure 5.8b), EIA reaches 9.46, which is 1.64 times of the total number of electrons on the electrode. Since the BF_4^- anion concentration is zero for $z < 0.5$ nm, we conclude that the number of TEA^+ cations adsorbed on the electrode exceeds the total number of electrons on the electrode, in qualitative disagreement with the Helmholtz model. The above *EIA*(*z*) profile indicates that the electrode may be over-screened at $z = 0.49$ nm, but the delocalized nature of charge on the ions prevents a quantitative conclusion to be drawn.

To better quantify the charge screening, we introduce a charge screening factor

$$C_f(z) = \int_0^z [\rho^e_{co-ion}(s) - \rho^e_{counter-ion}(s)]ds / \sigma \qquad (5.3)$$

where $\rho^e_{counter-ion}$ and ρ^e_{co-ion} are the space charge density of the counter-ion and the co-ion, respectively. $C_f(z) = 1.0$ corresponds to a complete screening of the electrode charge at position *z*, and $C_f(z) > 1.0$ corresponds to an over-screening of the electrode charge. The Helmholtz model predicts that $C_f(z)$ reaches 1.0 at the Helmholtz plane and remains 1.0 at positions beyond that. The more sophisticated Poisson−Boltzmann (PB) or Stern/Helmholtz + PB models predict that $C_f(z)$ reaches 1.0 at several Debye lengths from the electrode but never exceeds 1.0. Figure 5.9b shows that the variation of $C_f(z)$ near the electrode with $\sigma = -0.105$ C/m^2. $C_f(z)$ is larger than 1.0 in the region $0.5 \text{ nm} < z < 0.86$ nm. This is not entirely surprising since strong correlation between the counter-ion and

co-ions, which is not accounted for in the classical PB model, is known to cause over-screening of the electrode (often termed "charge inversion").[102]

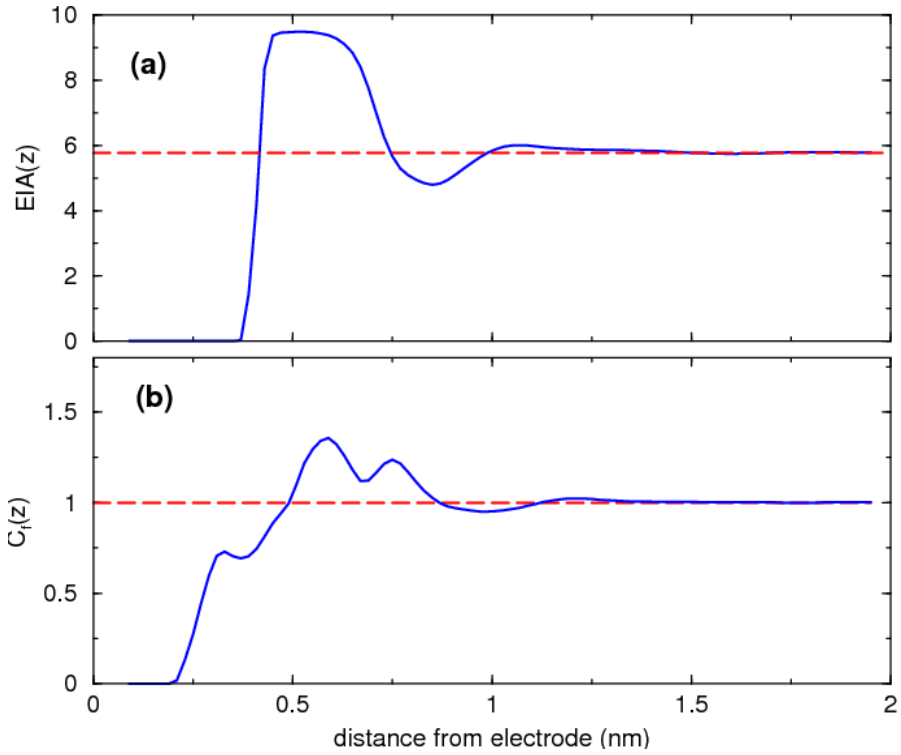

Figure 5.9: Variation of the effective ion accumulation (EIA) factor (panel a) and the charge screening factor (C_f) (panel b) near an electrode with $\sigma = -0.105$ C/m^2.

The dense packing of TEA^+ cations near the electrode can potentially lead to changes in the solvation of the interfacial ions, i.e., some TEA^+ cations might lose more of their solvation shell due to their small separation with other TEA^+ cations adsorbed on the electrode. To determine to what extent the contact adsorbed TEA^+ cations lose their solvation shell in the direction parallel to the electrode, we compute the average distance between the contact-adsorbed TEA^+ cations by assuming that these ions are packed hexagonally on the electrode. The average distance between these TEA^+ cations were

found to be 1.32 nm and 1.04 nm for $\sigma = -0.04$ and -0.105 C/m^2, respectively. Since these separations are smaller than the diameter of solvated TEA^+ cations (1.58 nm, see Figure 5.2a), we conclude that, for the electrode charge densities studied, TEA^+ cations contact-adsorbed on the electrode shed part of their solvation shell. This is not only due to the geometrical confinement by the electrode, but also due to the lateral confinement by other TEA^+ cations. In particular, at $\sigma = -0.105$ C/m^2, there are few ACN molecules between the TEA^+ cations adsorbed on the electrode.

The adsorption of counter-ions on the electrode also changes the structure of interfacial solvents. Figure 5.10a shows the concentration profiles of ACN molecules near the electrodes with $\sigma = 0$, -0.04, and -0.105 C/m^2. The first ACN peak decreases significantly as the electrode charge density increases. This is caused by displacement of ACN molecules by the bulky TEA^+ cations adsorbed on the electrode. Note that the sharp ACN concentration peak at $\sigma = 0$ and -0.04 C/m^2 is broadened and has a much lower peak when σ increases to -0.105 C/m^2. This is partly due to the large change in ACN orientation. Figure 5.10b shows the orientation of the NC vector of ACN molecules within 0.56 nm from the electrode with respect to the normal direction of the electrode, at different electrode charge densities. We observe that, as σ becomes more negative, the ACN molecules orient their methyl group closer to the electrode than their nitrogen atom. At $\sigma = -0.105$ C/m^2, *ca.* 50% of the ACN molecules in the first ACN layer are oriented with their NC vector pointing at an angle equal to or larger than 120 ^{o}with respect to the normal direction of the electrode, consistent with that inferred from the SFG measurements.[106] Compared to the situations at $\sigma = 0$ or $\sigma = -0.04$ C/m^2, such an

orientation of the ACN molecules reduces the overall non-electrostatic attraction exerted on the ACN molecules by the electrode, and leads to a less sharp but wider span of the first ACN peak compared to those when $\sigma = 0$ and -0.04 C/m^2. The orientational ordering of the NC vectors of ACN molecules becomes weak for $z > 0.56$ nm and thus are not shown.

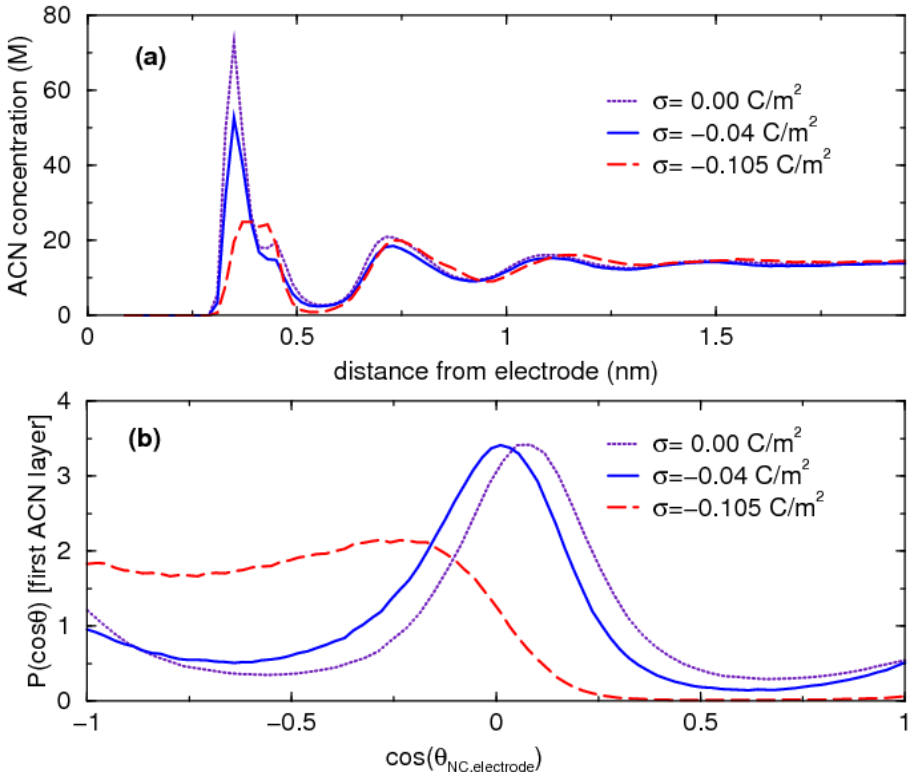

Figure 5.10: (a) Concentration distribution of ACN molecules near electrodes with various charge densities. (b) Orientation distribution of the NC vector (defined in the caption of Figure 5.3) of ACN molecules within 0.56 nm of the electrode with respect to the normal direction of electrodes.

5.3.3 Structure of EDLs near Positive Electrodes

Figures 5.11a and 5.11b show the concentration distribution of TEA^+ and BF_4^- ions near electrodes with σ = +0.040 and +0.105 C/m^2. The trends of the counter-ion and co-ion distribution, such as significant contact adsorption of the counter-ion on the electrode, alternating counter-ion/co-ion concentration peaks, and over-screening of the electrode charge, are similar to those observed near the negative electrode.

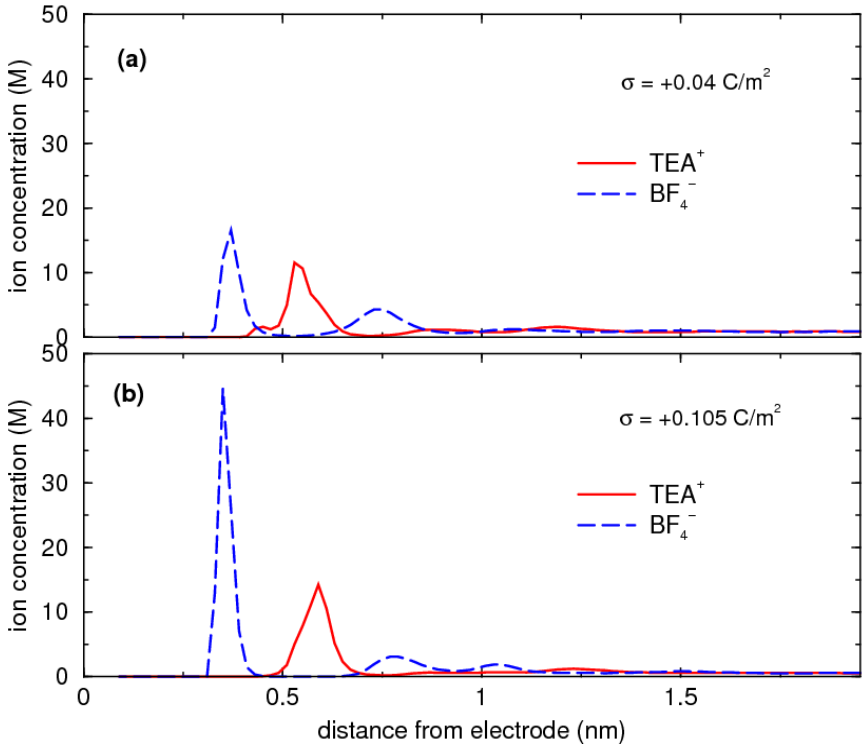

Figure 5.11: Concentration distribution of TEA^+ and BF_4^- ions near electrodes with charge densities of +0.04 C/m^2 (panel a) and +0.105 C/m^2 (panel b).

The primary difference between the EDL structures near the positive and negative electrodes lies in the solvation of the counter-ions contact-adsorbed on the electrodes. The average lateral spacing between the BF_4^- anions adsorbed on electrodes with σ =

+0.040 and +0.105 C/m^2 was found to be 1.43 nm and 0.98 nm, respectively. Since the diameter of solvated BF_4^- anion in bulk is 1.2 nm (cf. Figure 5.2a), we conclude that, the solvation of contact adsorbed BF_4^- anions is hardly perturbed by their neighbors near electrodes with σ = +0.040 C/m^2, but becomes moderately perturbed when σ = +0.105 C/m^2. As expected,[106] the structure of ACN, near the electrodes becoming more positively charged, changes as well as those of ions.

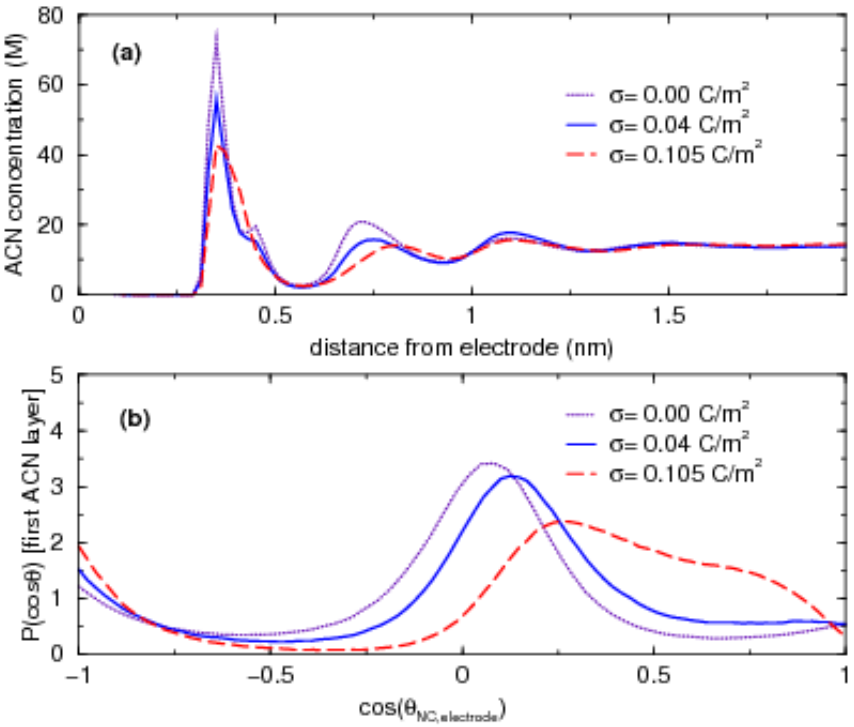

Figure 5.12: (a) Concentration distribution of ACN molecules near electrodes with various charge densities, (b) Orientation distribution of the NC vector of ACN molecules within 0.56nm of the electrode with respect to the normal direction of electrodes.

Figure 5.12a shows the concentration profiles of ACN molecules near the electrodes with σ = 0, +0.04, and +0.105 C/m^2. Near positive electrodes, the evolution of the ACN concentration profile near the electrode as the magnitude of electrode charge

density increases is similar to that observed near the negative electrode (cf. Figure 5.10). Figure 5.12b shows the orientation of the NC vector of ACN molecules within 0.56 nm from the positive charged electrode with respect to the normal direction of the electrode, at different electrode charge densities. In contrast to the EDLs near negative electrodes (cf. Figure 5.10), when the electrode charge density becomes more positive, the NC vectors of the interfacial ACN molecules become more aligned with the normal direction of the electrode.

5.3.4 EDL Capacitance

Since the electrical potential in the central portion of the MD system is constant, the potential drop across the EDLs near each of the electrodes, ϕ_{EDL}, can be computed separately. Using Equation 5.1, we computed ϕ_{EDL} for EDLs near the positive and negative electrodes as the potential differences between the two electrodes increases from 0 to 2.7 V (Figure 5.13a). To compute the capacitance C_{edl} of the EDLs, we first fitted the $\phi_{EDL} - \sigma$ correlation to a fourth-order polynomial and then computed C_{edl} by Equation 3.1. In the literature, C_{edl} is often computed by $C_{\text{edl}} = \sigma / \phi_{EDL}$, which is a good approximation to the exact definition given by Equation 3.1 only when $C_{\text{edl}} >> PZC$. In the present study, ϕ_{EDL} is less than 1.5 V and PZC = 0.168 V, hence it is necessary to use Equation 3.1 to accurately compute C_{edl}. Figure 5.13b shows C_{edl} as a function of the electrode charge density and the magnitude of the capacitance is similar to that found in experiments, e.g., the capacitance of planar carbon electrode immersed in $TEABF_4$/ACN electrolyte extrapolated from capacitance of carbon mesoporous pores is 0.09 F/m^2.[15]

We observe that C_{edl} is relatively insensitive to the electrode charge density – C_{edl} remains nearly a constant between $\sigma = 0$ to $+0.105$ C/m^2 and C_{edl} for EDLs near negative electrodes decreases moderately (*ca.* 27%) as σ increases from 0 to -0.105 C/m^2. The weak dependence of C_{edl} is consistent with the experimental observation in the galvanostatic charge/discharge, where the slope of cell voltage versus time is nearly independent of voltage window.[84] Near electrodes with $|\sigma| = 0.105$ C/m^2, C_{edl} is 27% higher when the BF_4^- anions are the counter-ions compared to when TEA^+ cations are the counter-ions. This is due to the smaller size of the BF_4^- anions compared to that of the TEA^+ cations, which allows them to approach closer to the electrode.

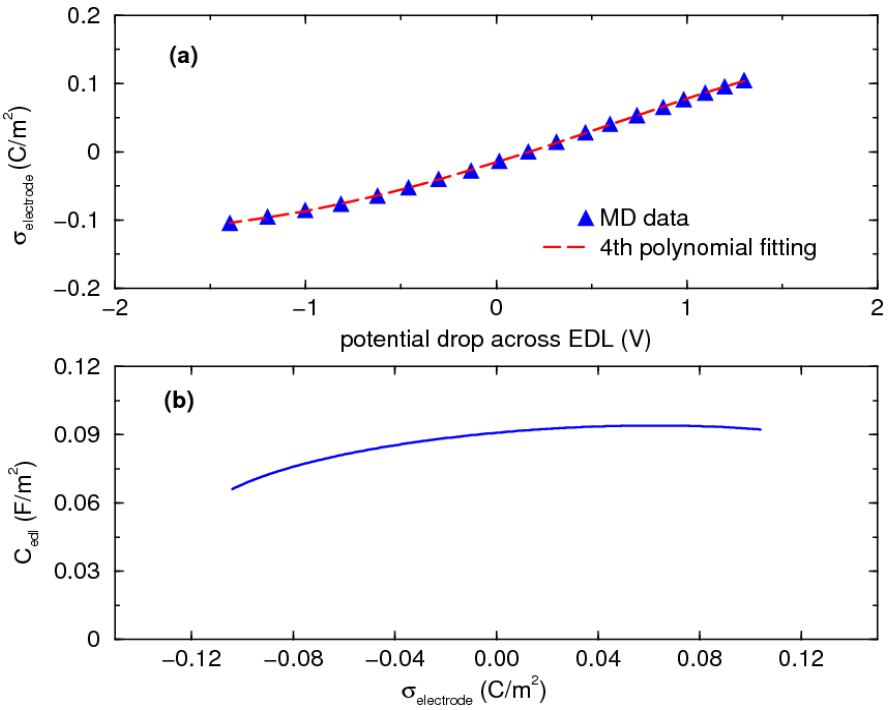

Figure 5.13: (a) Relation between electrode charge density and potential drop across the EDLs adjacent to the electrodes, (b) Capacitance C_{edl} of the EDLs adjacent to the electrodes with different surface charge densities.

The good agreement between the capacitance predicted by MD simulations and that inferred from experimental studies suggests that the key aspects of the EDLs are captured. However, we note that many aspects of the EDLs have yet to be incorporated with sufficient details. Most importantly, the electronic degrees of freedom of the electrode have largely been neglected in the existing literature. In our simulations, the electrode is modeled as an object of uniform potential and the electrostatic interactions between the electrode and charges inside the system are treated classically. In addition, the quantum nature of the electrode is only considered via the concept of electrode image plane, positioned 0.08 nm away from the electrode. However, the effective location of the image plane of an electrode is known to shift as its surface charge density changes.[110] Therefore, the dependence of the capacitance on the electrode charge density should be taken as semi-quantitative. A more accurate modeling of the EDLs and calculation of the capacitance should take into account the coupling between the electronic degrees of freedom of the electrode and the solvent/ion structure on the electrolyte side. Simulations of this type have been attempted for EDLs in aqueous electrolyte[111] but have not been reported for EDLs in organic electrolytes.

5.4 Dynamics of EDLs

5.4.1 Solvent Rotational Dynamics

The electrochemical decomposition of organic solvents is closely related to the translational and rotational dynamics of the interfacial solvents. Here we first quantify the

rotational dynamics of ACN molecules by computing the dipole autocorrelation function d_{ACF}

$$d_{ACF}(t) = \langle \boldsymbol{p}_i(0)\, \boldsymbol{p}_i(t) \rangle / \langle \boldsymbol{p}_i(0)\, \boldsymbol{p}_i(0) \rangle \qquad (5.4)$$

where $\boldsymbol{p}_i$ is the dipole moment of an ACN molecule *i*.

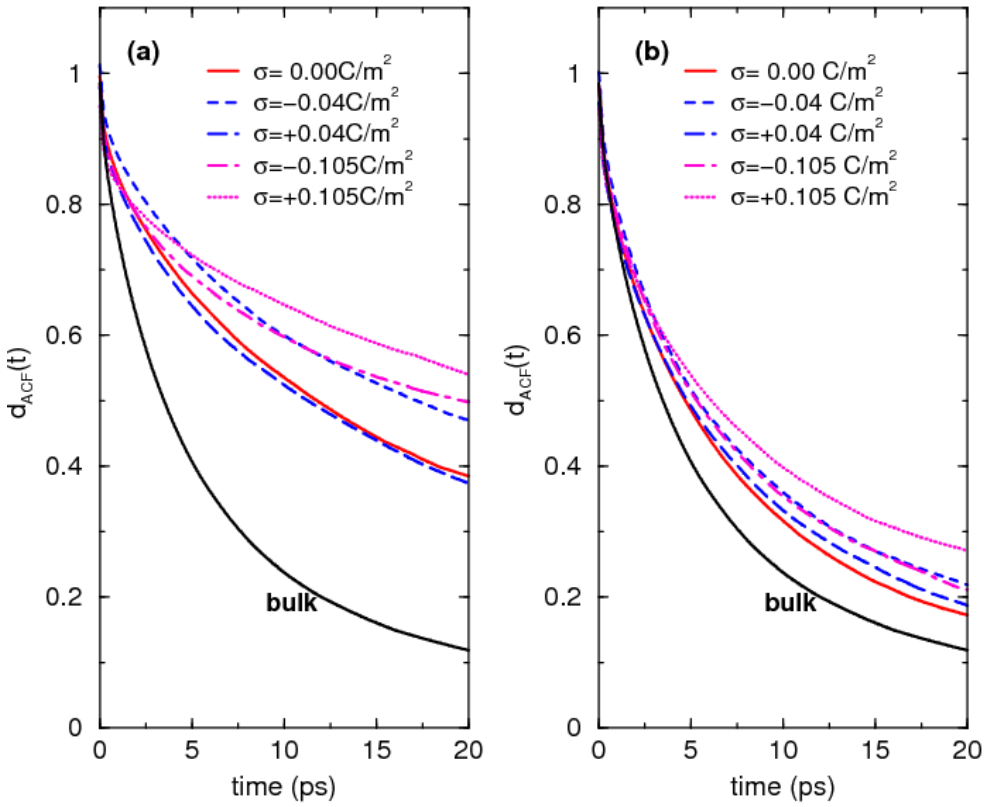

Figure 5.14: Dipole autocorrelation function for ACN molecules at different locations from the electrodes. (a): ACN molecules in region z < 0.56 nm; (b): ACN molecules in region 0.56 nm < z < 1.12 nm.

A faster decay of $d_{ACF}(t)$ corresponds to a more free rotation of the molecule. Figure 5.14a shows $d_{ACF}(t)$ for the ACN molecules in the regions of z < 0.56 nm (i.e., the first ACN layer). We observe that the rotation of the ACN molecules in the first ACN

layer is significantly retarded compared to that in the bulk, even at zero electrode charge density. As the electrode becomes electrified, the rotation of these ACN molecules, are generally more hindered. For same magnitude of electrode charge density, the rotation has an asymmetric dependence on the sign of the electrode charge. Interfacial ACN molecules rotate more freely near electrodes with $\sigma = +0.04$ C/m^2 than that near electrodes with $\sigma = -0.04$ C/m^2, and the opposite trend is observed when $|\sigma| = 0.105$ C/m^2. To understand these observations, we note that compared to that of the ACN molecules in bulk, the rotation of interfacial ACN molecules is retarded by several additional mechanisms: (1) hindrance by the electrode, and (2) interference by the ions adsorbed on the electrode. As the electrode becomes electrified, hindrance of ACN rotation by the electrode and by the ions adsorbed on the electrodes increases simultaneously since the ACN−electrode interactions become stronger and more counter-ions are adsorbed on the electrode. Consequently the quasi-free rotation of ACN molecules decreases. At $|\sigma| = 0.04$ C/m^2, the average distance between the TEA^+ cations adsorbed on the negative electrode (1.32 nm) is smaller than that between the BF_4^- anions adsorbed on the positive electrode (1.43 nm). This fact, along with the larger size of the TEA^+ cations, indicates that the interfacial ACN molecules occupying the space between TEA^+ cations adsorbed on negative electrodes are more confined in the lateral direction. Hence their rotation is more difficult than that of the ACN molecules adjacent to positive electrodes. At $|\sigma| = 0.105$ C/m^2, the geometrical confinement created by the TEA^+ cations adsorbed on the negative electrode is still stronger compared to that of BF_4^- anions adsorbed on the positive electrode. However, since the ACN−BF_4^- interactions are

stronger than the ACN−TEA^+ interactions (see Figure 5.2), the rotation of ACN molecules adjacent to the positive electrodes slows down slightly more than those adjacent to the negative electrodes.

Figure 5.14b shows $d_{ACF}(t)$ for the ACN molecules in region 0.56 nm < z < 1.12 nm. The decay of these dipole autocorrelation functions is similar to that in the bulk and is not strongly affected by the electrification of the electrodes. This shows that the influence of the electrode on the ACN rotation dynamics is limited primarily to the first ACN layers adjacent to the electrode. This is consistent with the observation that ACN structure (e.g., concentration and orientation) becomes nearly homogeneous beyond the first ACN layer adjacent to the electrode.

5.4.2 Solvent and Ion Diffusion

The self diffusion coefficients of TEA^+, BF_4^- and ACN molecules in our MD system were determined by integrating their velocity autocorrelation functions. We found that the diffusion coefficients deviate from bulk values primarily in the region within 0.56 nm from the electrode. Therefore, only the diffusion coefficients in this region are shown in Table 5.1. For the ACN molecules adjacent to the electrodes, we observed that their diffusion coefficients show several features: (1) the diffusion is strongly anisotropic: near the same electrode, the diffusion coefficients in directions parallel to the electrode ($D_{//}$) are *ca.* 2.6-2.9 times larger than those in the direction normal to the electrode ($D_{\perp}$), (2) $D_{//}$ near the electrodes is always smaller than that in the bulk and decreases moderately as the

electrodes become electrified, (3) there is an asymmetry in the dependence of $D_{//}$ on the sign of electrode charge.

Table 5.1: Self diffusion coefficients of molecules (in unit of 10^{-9} m^2/s) in the region of 0.56 nm from the electrode.

$\sigma_{electrode}$ (C/m^2)	ACN		TEA^+		BF_4^-	
	$D_{//}$	$D_{\perp}$	$D_{//}$	$D_{\perp}$	$D_{//}$	$D_{\perp}$
0	1.92 ± 0.18	0.68 ± 0.06	0.87 ± 0.13	0.15 ± 0.02	1.00 ± 0.13	0.17 ± 0.03
−0.04	1.66 ± 0.10	0.63 ± 0.03	0.79 ± 0.11	0.13 ± 0.02	NA	NA
+0.04	1.90 ± 0.13	0.65 ± 0.07	NA[a]	NA	0.89 ± 0.05	0.23 ± 0.04
−0.105	1.53 ± 0.04	0.52 ± 0.02	0.80 ± 0.08	0.09 ± 0.03	NA	NA
+0.105	1.25 ± 0.10	0.46 ± 0.07	NA	NA	0.74 ± 0.09	0.19 ± 0.01
In bulk	2.34 ± 0.06		0.96 ± 0.02		0.82 ± 0.05	

[a] NA indicates that $D_{//}$ and $D_{\perp}$ cannot be accurately computed due to the scarcity of molecules in the region.

Similar asymmetry can also be observed for $D_{\perp}$, but it is much weaker. Observation 1 can be rationalized by the geometrical confinement imposed on the ACN molecule by the electrode, and similar anisotropy has long been observed for other interfacial fluids.[112] Observation 2 is related to the fact that as the electrodes become electrified, they interact stronger with the ACN molecules and more counter-ions become contact-adsorbed on the electrodes, both of which restrict the diffusion of ACN molecules. Observation 3 has the same origin with the asymmetric dependence of rotational motion on the sign of electrode charge as discussed in Section 5.2. Specifically, at $|\sigma| = 0.04$ C/m^2, the slower diffusion of ACN molecules near electrode with $\sigma = -0.04$ C/m^2 is due to the weaker lateral confinement imposed by the TEA^+ cations adsorbed on

the electrode. At $|\sigma| = 0.105$ C/m^2, the slower diffusion of ACN molecules near electrodes with $\sigma = +0.105$ C/m^2 is due to their stronger interactions with the BF_4^- anions adsorbed on the positive electrode. As these mechanisms primarily constrain the motion of ACN molecules in the direction parallel to the electrode, the asymmetrical dependence of $D_\perp$ on the sign of electrode charge is much weaker.

The diffusion of TEA^+ and BF_4^- ions show similar features as those of the ACN molecules, e.g., anisotropy and decrease of $D_\perp$ as the electrode charge density increases. An interesting difference is that, $D_{//}$ of interfacial ions is only weakly affected by the electrode. For TEA^+ cations, $D_{//}$ near all electrodes is only slightly smaller than that in the bulk, and their dependence on the electrode charge is negligible. For BF_4^- anions, $D_{//}$ near electrodes with $\sigma = 0$ and $+0.04$ C/m^2 are even larger than that in the bulk. To understand these phenomena, we note that TEA^+ and BF_4^- ions form contact ion pairs in bulk electrolytes, which significantly deteriorate their diffusion. When these ions are adsorbed on the electrodes, the number of ion pairs that they participate in is reduced by the electrode and thus, their diffusion is much less constrained. While the ion diffusion in directions parallel to electrode is made more difficult by the electrode−ion interactions, this effect is less important because of the atomically smooth electrodes used in this study. Therefore, the lateral diffusion of ions near moderately charged electrodes is comparable to, or faster than, that in the bulk. In addition to the above mechanism, the diffusion of interfacial ions is also hindered by other interfacial ions. The diffusion coefficient of interfacial ions is a result of the competition between these mechanisms. The results collated in Table 5.1 show that, for larger TEA^+ cations or BF_4^- anions near

highly charged electrodes, the latter mechanism dominates; for smaller BF_4^- anions near neutral or moderately charged electrode, the first mechanism dominates.

5.5 Conclusions

The solvation of TEA^+ and BF_4^- ions in bulk ACN was studied using MD simulations. The solvation of TEA^+ and BF_4^- ions [113] were found to be much weaker than those of typical small inorganic ions. The ACN molecules in the solvation shell of both ions show impotent packing and orientational ordering, which are caused by the large size, charge delocalization, and irregular shape (in the case of TEA^+ cation) of these ions. TEA^+ and BF_4^- ions form contact ion pairs in bulk ACN solution.

The structure and capacitance of the EDLs at the interface of organic electrolytes consisting of $TEABF_4$/ACN and model electrodes were also studied using MD simulations. The results indicate that:

1. Near neutral electrodes, the double-layer structure in the organic electrolyte is not a homogeneous mixture of ions and solvent as expected from classical continuum theories, but exhibits a number of notable features: the solvent shows strong layering and orientational ordering, ions are significantly contact-adsorbed on the electrode, and alternating layers of cations/anions penetrate about 1.1 nm into the bulk electrolyte. Although some of these features can also be observed in aqueous electrolytes, the significant contact-adsorption of ions and the alternating layering of cation/anion are new features found for EDLs in organic electrolytes. These features essentially originate from

the fact that van der Waals interactions between the organic ions and electrode are strong and the partial desolvation of these ions occurs easily, both of which stems from the large size of the organic ions.

2. Near charged electrodes, distinct counter-ion concentration peaks, corresponding to the contact adsorption of counter-ions, are observed and the alternating layering of counter-ion/co-ion remains. The ion distribution cannot be described by the Helmholtz or Helmholtz + PB models, because the number of counter-ions adsorbed on the electrode exceeds the electron charge on the electrode, and electrode is over-screened in part of the EDL. At $\sigma = \pm 0.105$ C/m^2, the counter-ions adsorbed on the electrode are partly desolvated in directions parallel to the electrode. The orientation of ACN molecules in the first ACN layer adjacent to the electrode is consistent with that expected from simple electrostatic theories, and the orientational ordering of ACN molecules becomes weak beyond the first ACN layer. The capacitance of the EDLs was determined to vary from 0.065 F/m^2 to 0.092 F/m^2 as the electrode charge density changes from −0.105 C/m^2 to +0.105 C/m^2, in good agreement with that inferred from experimental measurements.

The rotation of interfacial ACN molecules is slowed down and this becomes more significant as the electrode is electrified. Retardation of the rotation of interfacial ACN molecules shows an asymmetric dependence on the sign of the electrode charge and was understood as a result of different ACN−ion interactions near electrodes with different signs of surface charge density. The diffusion of interfacial ACN, TEA^+, and BF_4^- ions is strongly anisotropic with the diffusion in directions parallel to the electrode ($D_{//}$) much

larger than that in the direction normal to the electrode ($D_{\perp}$). $D_{//}$ of the interfacial ACN generally decreases as the magnitude of the electrode charge density increases. Similar to the rotation motion, the translational diffusion of interfacial ACN molecules also shows asymmetrical dependence on the sign of electrode charge. $D_{//}$ of interfacial ions has much less dependence on the magnitude of the electrode charge density. For BF_4^- anions adsorbed on the positive electrode, their diffusion coefficient is higher than that in the bulk because their motion near the charged electrode is less constrained by their pairing formed with TEA^+ cations. The rotation/diffusion of ACN and the diffusion of ions in the region beyond the first ACN or ion layer differ only weakly from those in the bulk.

CHAPTER 6

EDLS IN IONIC LIQUIDS NEAR PLANAR ELECTRODES

Chapter 5 reveals that the layering of cation/anion and the charge overscreening are key features of EDLs in electrolytes containing polyatomic ions, which would be rationally anticipated to occur in ILs since the cations and/or anions in ILs are also polyatomic. Therefore, we studied the microstructure and capacitance of the EDLs at the interface of ILs and planar electrodes by modeling the electrode and ILs with full chemical details using a classical MD method. The objective of this chapter is to explore (1) what's the role of the "ionic" nature and "liquid" nature of ILs in shaping EDLs near planar electrodes, (2) to what extent the charge delocalization of ions could influence the EDL structure, (3) whether the capacitance-potential ($C-V$) curves obtained in MD simulation agree with those in the literature, (4) what's the origin of the trend of $C-V$ curves, and (5) whether there is a direct connection between the microstructure and macroscopic capacitance of an EDL.

6.1 MD Simulation Setup

We performed molecular dynamics simulations of [BMIM][NO_3] liquids enclosed between two oppositely charged channel walls to exploit EDLs in ILs near the open solid surface. Each wall was modeled as a slab of α-quartz oriented in the [100] direction. The channel width was set as 6.63 nm (measured between the innermost layers of the opposing channel walls) to produce a bulklike behavior in the channel center. Thirteen

cases with surface charge densities (σ) ranging from 0.00, ±0.01 to ±0.12 C/m^2 were studied. To produce a given wall charge density, a small charge was added to the atoms in the innermost wall layers. To evaluate the dependence of EDL observables on the IL density in the channel center, we performed additional simulations for the channel system with surface charge densities of ±0.10 C/m^2 by reducing/increasing the number of IL molecules in the system by 2.38%. The simulation results on the EDL structure and electrical potential inside EDL were found to vary only marginally as the number of IL molecules inside the system changed, thus indicating that the result obtained in this work is insensitive to the precise value of the IL density at the channel center. To compute the electrostatic interactions in the two-dimensionally periodic geometry adopted here, the slab-PME method was used.

6.2 EDL Microstructure

Figure 6.1a and b shows the number density of $[NO_3]^-$ and $[BMIM]^+$ ions near positively charged electrodes. The location of cations and anions are computed on the basis of the geometrical center of the imidazolium ring and the entire anion, respectively. Figure 6.1a indicates that as the surface charge density (σ) increases, the $[NO_3]^-$ ion density near the electrode increases dramatically, and the location of the first peak moves toward the electrode. At σ = 0.09 C/m^2, a single $[NO_3]^-$ ion layer can be clearly delineated in the region z = 0.15−0.41 nm, which seems to support the Helmholtz model for the EDL. However, the MD results also point to several new features unavailable in

the Helmholtz model. First, a distinct Helmholtz layer is difficult to delineate at relatively low electrode charge densities; for example, $\sigma < 0.03$ C/m^2. Second, there is a significant accumulation of $[BMIM]^+$ ions within the first counter-ion layer, particularly at low σ. As σ increases, the $[BMIM]^+$ density peak becomes lower and moves away from the electrode, but a significant $[BMIM]^+$ ion accumulation can still be observed in the region of $z = 0.27 - 0.45$ nm, even at $\sigma = 0.09$ C/m^2 (see Figure 6.1b). Third, the thickness of the EDL is much larger than that of the first counter-ion layer. This is seen clearly from the space charge density profile near the electrode, as shown in Figure 6.1c, where charge separation is observed at a position as far as $z = 1.0$ nm from the electrode. Finally, ILs exhibit a rich structure at positions much beyond the first counter-ion layer. For example, rather than being a constant, the density of the IL near a neutral electrode exhibits significant oscillation at a position within 1.0 nm from the electrode. The IL structure is also quantified by computing the order parameter of the ions $P_2(\cos\theta) = <(3\cos^2\theta - 1)/2>$, where θ is defined as the angle formed by the normal vector of the electrode and the normal vector of the imidazolium ring of the $[BMIM]^+$ ion or the plane formed by the three oxygen atoms of the $[NO_3]^-$ ion. Figure 6.1d and e shows the distribution of $P_2(\cos\theta)$ near the electrode for the $[NO_3]^-$ and $[BMIM]^+$ ions, respectively. We observe that at a position very close to the electrode, both $[BMIM]^+$ and $[NO_3]^-$ ions orient nearly parallel to the electrode and become more random as they move away from the electrode. However, the orientational ordering disappears only at a position about 1.1 nm from the electrode.

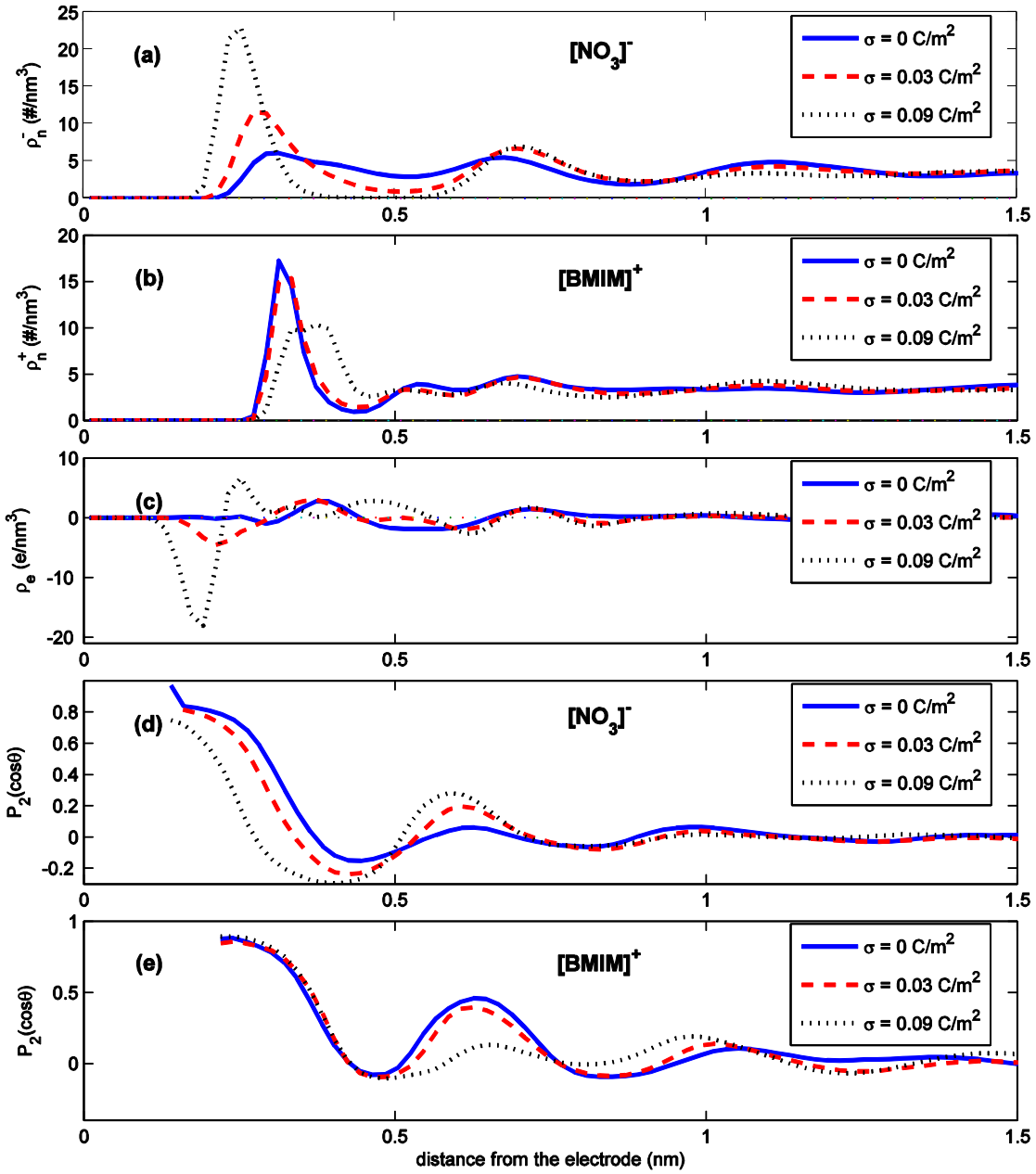

Figure 6.1: Number density of the $[NO_3]^-$ (panel a) and $[BMIM]^+$ (panel b) ions near neutral and negatively charged electrodes. (c) Space charge density profiles near the electrodes. (d, e) Orientational order parameter $P_2(\cos\theta)$ of $[NO_3]^-$ (panel d) and $[BMIM]^+$ (panel e) ions near neutral and negatively charged electrodes.

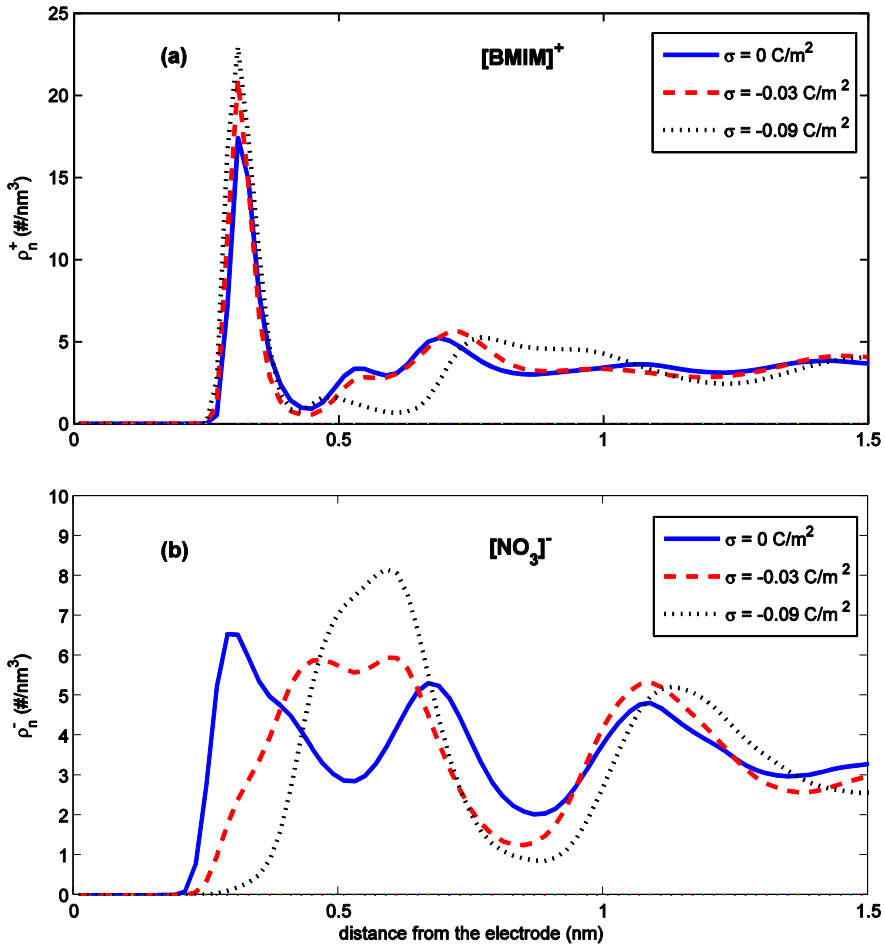

Figure 6.2: Number density of $[BMIM]^+$ (panel a) and $[NO_3]^-$ (panel b) ions near neutral and negatively charged electrodes.

Figures 6.2a and 6.2b show the number density profiles of the $[BMIM]^+$ and $[NO_3]^-$ ions near negatively charged electrodes. We observe that the $[BMIM]^+$ ions exhibit a distinct peak at a position of 0.31 nm from the electrode, and the height of the peak increases weakly as σ becomes more negative. Unlike the $[NO_3]^-$ ions near positively charged electrodes, the $[BMIM]^+$ layer near negative electrodes can be delineated even at very low charge densities. We also observe that as σ becomes more negative, although the first density peak of the $[NO_3]^-$ ion moves away from the

electrode, its magnitude increases notably. At $\sigma = -0.09$ C/m^2, the density of the $[NO_3]^-$ ion at its first peak (z = 0.59 nm) is 2.4 times of that in the bulk. Such a phenomenon is not only rarely observed in aqueous electrolytes and high-temperature molten salts but also difficult to explain by the recent EDL models developed for ILs. The orientational ordering of the $[BMIM]^+$ and $[NO_3]^-$ ions shows a feature similar to that near positively charge electrodes and is not shown.

Although the above results are obtained for a specific type of IL, they can provide useful insights into the generic picture of the EDLs in ILs.

First of all, the liquid nature of ILs and short-range interactions play a key role in shaping the EDL structure. The "ionic" nature of the ILs (i.e., IL molecules carry net charges) is clearly important in determining the long-range electrostatic interactions and, thus, the EDL structure. But we also note that, as far as the molecular structure at the IL-electrode interface is concerned, ILs are also "liquids", and the interfacial structure of the ILs near electrodes (i.e., the structure of the EDLs) should at least partly observe the generic theory for the molecular structure at liquid−solid interfaces. Specifically, the short-range (electrostatic or non-electrostatic) IL−IL and IL−electrode interactions (or, equivalently, the short-range ion−ion and ion-electrode correlations) play an important role in determining the structure of the ILs near the electrode.[29] We expect that the effects of these interactions and correlations on the EDL structure to be particularly significant at low surface charge densities and should remain important at high surface charge densities. These expectations are confirmed by the results shown in Figure 6.1 and Figure 6.2. First, as shown in Figures 6.1a and 6.1b, near neutral electrodes, ILs exhibit

significant density oscillation that is a characteristic of the interfacial liquid structure,[29] and such oscillation penetrates about 1.0 nm into the ILs. Since the electrode is electrically neutral, such rich structure is induced mainly by the short-range interactions and correlations. At $\sigma = \pm 0.03$ C/m^2, these density oscillations persist, and the shape of the space charge density profile near the electrode remains similar to that near neutral electrodes (see Figure 6.1c). This suggests that the EDL structure is still strongly affected by the short-range IL−IL and IL−electrode interactions. Similar conclusions have also been reached for the EDLs in high-temperature molten salts.[114-117] However, in high-temperature molten salts, the density oscillation penetrates much deeper (about 2 nm) into the bulk salts.[114-116] Such a difference is most likely caused by the fact that the short-range correlation between the smaller ions in molten salts is much stronger as compared to that between bulky ions in ILs, and thus, the structuring of liquids caused by such short-range correlations extends deeper into the bulk liquids of molten salts. In addition, as indicated by the high density peak at $z = 0.31$ nm (see Figure 6.1b), $[BMIM]^+$ ions are adsorbed persistently on the electrodes, even when they are positively charged. Such a phenomenon appears to be consistent with the experimental observation[118] [119] and has also been observed in the MD simulation of [DMIM][Cl] near structureless electrodes[120]. Such adsorption, although unfavorable from a long-range electrostatic interactions perspective, is favorable, considering the van der Waals interactions between the cation and the electrode. In fact, for a cation ring oriented parallel to the electrode, the non-electrostatic interaction energy between the ring and the electrode is $-2.42\ k_BT$ (k_B is the Boltzmann constant, and $T = 360$ K) at a ring−electrode separation of 0.31 nm, which

can induce significant $[BMIM]^+$ adsorption on the electrode. Finally, as shown in Figure 6.2, the peak of the $[NO_3]^-$ density profile near negatively charged electrodes increases as σ becomes more negative. Such a phenomenon is caused by the strong interactions between the $[BMIM]^+$ and $[NO_3]^-$ ions. Specifically, as the σ becomes more negative, more $[BMIM]^+$ ions are adsorbed onto the electrode, and they bring more anions toward the electrode.

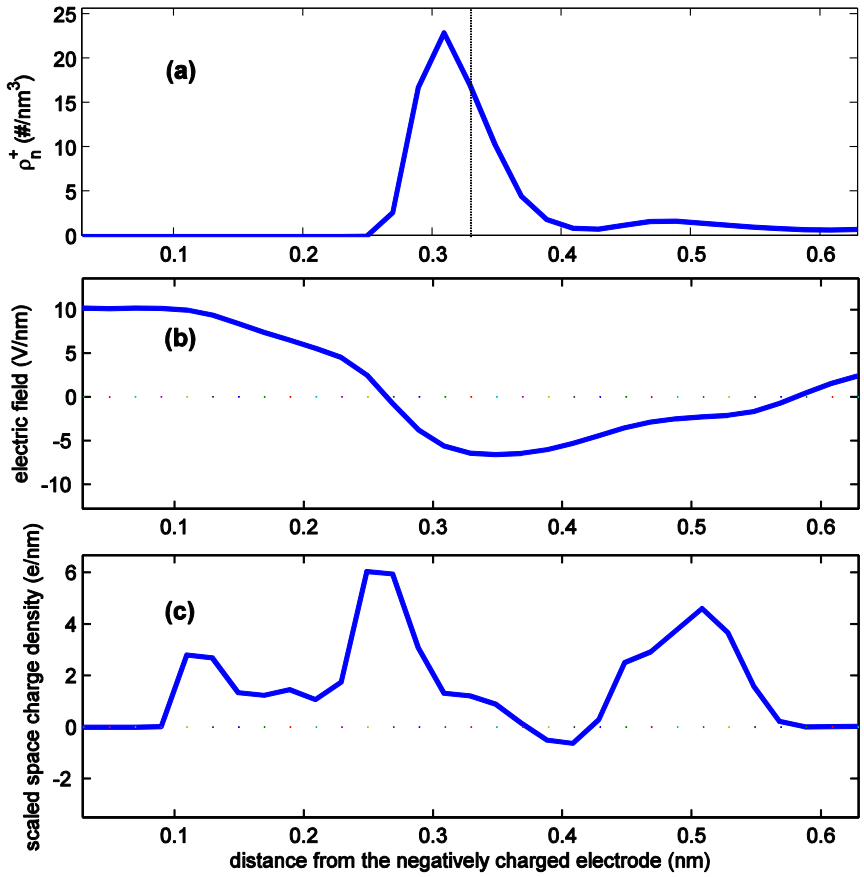

Figure 6.3: (a) Number density profiles of the $[BMIM]^+$ ions near the negatively charged electrode with a surface charge density of −0.09 C/m^2. (b) Mean electrical field near the electrode. (c) The space charge density due to the presence of a $[BMIM]^+$ ion centered at a position 0.34 nm away from the electrode (this position is indicated by a vertical dash line in panel a).

Second, the charge delocalization can play an important role in determining the EDL structure. Unlike in simple electrolytes, the charge of the ions in ILs is distributed among many atoms. Since the characteristic length of such delocalization is on the order of 3−5 Å, which is comparable to the thickness of the EDLs in ILs, the charge delocalization can potentially have profound impact on the long-range electrostatic interactions in EDLs. Specifically, the mean electrostatic force acting on an ion centered at position r, which affects heavily the EDL structure, depends not only on the electrical field at position r but also on the electrical field in the vicinity of r and the ion orientation. To appreciate this, we consider the mean electrostatic force acting on a $[BMIM]^+$ ion located at position 0.33 nm from an electrode with $\sigma = -0.09$ C/m^2 (the position of this ion is marked by the vertical dash line in Figure 6.3a). The total mean force acting on the $[BMIM]^+$ ion located here can be computed by $f_{tot} = -k_B T \, \mathrm{d}\ln\rho(z)/\mathrm{d}z = 25.5 k_B T$/nm, where k_B is the Boltzmann constant and T is the temperature. Figure 6.3b shows the mean electrical field near the electrode (the calculation of the mean electrical potential and field will be discussed in the Section 6.3). On the basis of Figure 6.3b, a naive calculation without considering the charge delocalization indicates that the mean electrostatic force acting on the $[BMIM]^+$ ion centered at $z = 0.33$ nm is $-207.7\ k_B T$/nm, which differs qualitatively from the total mean force computed above. Figure 6.3c shows the distribution of the space charge density due to the $[BMIM]^+$ ion centered at $z = 0.33$ nm, and we observe that the charge of this ion is distributed in the broad region of 0.1−0.58 nm from the channel wall. Using the mean electrical field in Figure 6.3b and the space charge density profile in Figure 6.3c, the mean electrostatic force acting on the

$[BMIM]^+$ ion is found to be 19.6 k_BT/nm, which is close to the total mean force calculated above. Although a firm conclusion on the effects of charge delocalization on EDL structure cannot yet be drawn without further detailed study, the above results do suggest that charge delocalization can play an important role in affecting the mean electrostatic force acting on the ions in ILs and, thus, the ion distribution in EDL.

These insights point to important directions for improving the theoretical models for the EDLs in ILs. For example, it is important to account for the effects of short-range IL−IL and IL−electrode interactions and charge delocalization on the ion distribution inside the EDL, which are neglected in most EDL models. These insights also open up new avenues for controlling the microstructure and macroscopic properties of the EDLs in ILs. For example, since the short-range IL−electrode interactions depend strongly on the surface chemistry of the electrode, it is possible to manipulate the structure and properties of the EDL (e.g., capacitance) by tuning the surface functionalization of the electrodes.

6.3 EDL Capacitance

For each case studied, the electrical potential distribution, $\phi(z)$, inside the channel is computed by solving Equation 3.4 based on the total space charge density shown in Figure 6.1c. With the corresponding boundary conditions: (1) $\phi(0) = 0$ and (2) $\left.\frac{d\phi}{dz}\right|_{bulk} = 0$, we obtain the solution of Equation 3.4 as

$$\phi(z) = -\frac{1}{\varepsilon_0}\int_0^z (z-u)\rho_e(u)du - \frac{\sigma}{\varepsilon_0}z \qquad (6.1)$$

This formula is suitable for EDLs near planar electrodes carrying surface charge density of σ, i.e., no electrode curvature effects on EDLs (e.g., the electrodes shown in Figure 1.3a and c and the EDL structures shown in Figure 6.1 and Figure 6.2).

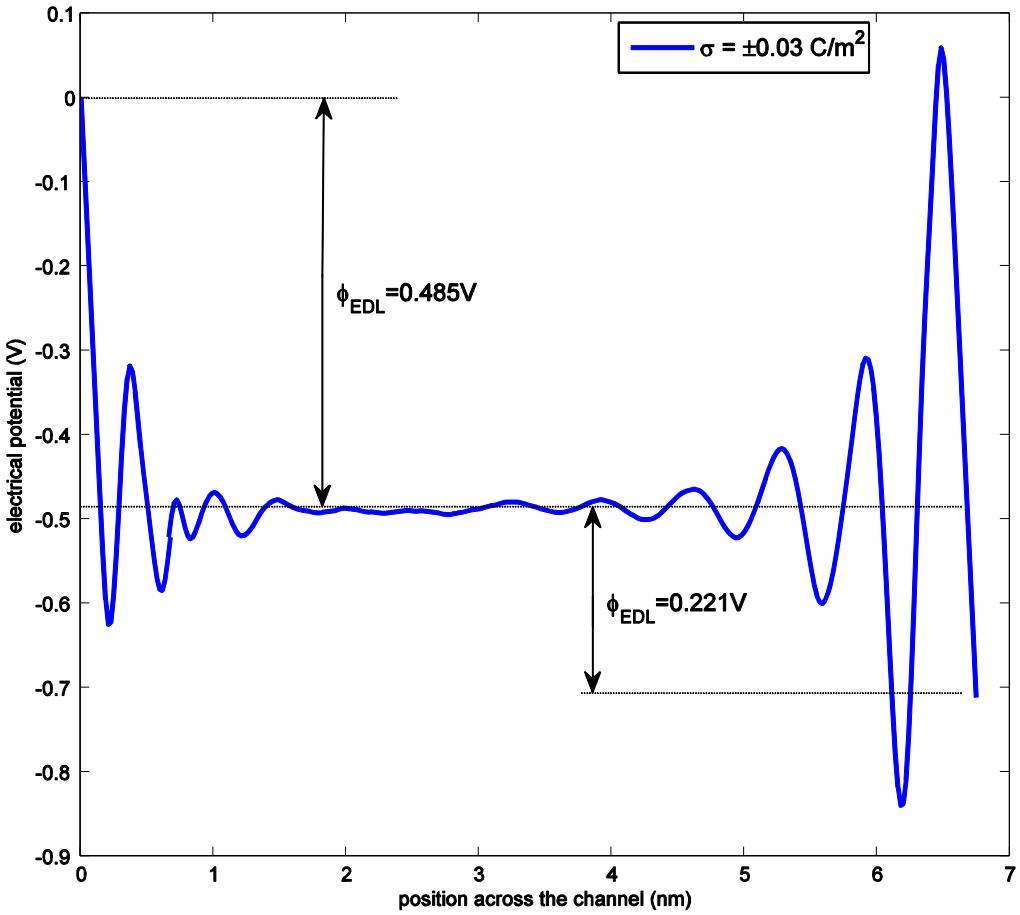

Figure 6.4: Distribution of the electrical potential across the channel (channel wall charge density: ±0.03 C/m^2). Because the electrical potential in the central portion of the channel is flat, the potential drop across the EDLs, ϕ_{EDL}, near the upper and lower channel walls can be evaluated from the electrical potential profile shown here.

Figure 6.4 shows the electrical potential distribution when the surface charge density on the two opposite channel walls is ±0.03 C/m^2. Similar to that in high-temperature molten salts, significant oscillation of the electrical potential is observed near the electrified surface.[114, 116] Since the electrical potential in the central portion of the channel is constant, the potential drop across the EDLs, ϕ_{EDL}, near each of the channel walls was then identified as shown in Figure 6.4. Using this procedure, ϕ_{EDL} for EDLs near channel walls with a surface charge density ranging from −0.12 to +0.12 C/m^2 was obtained.

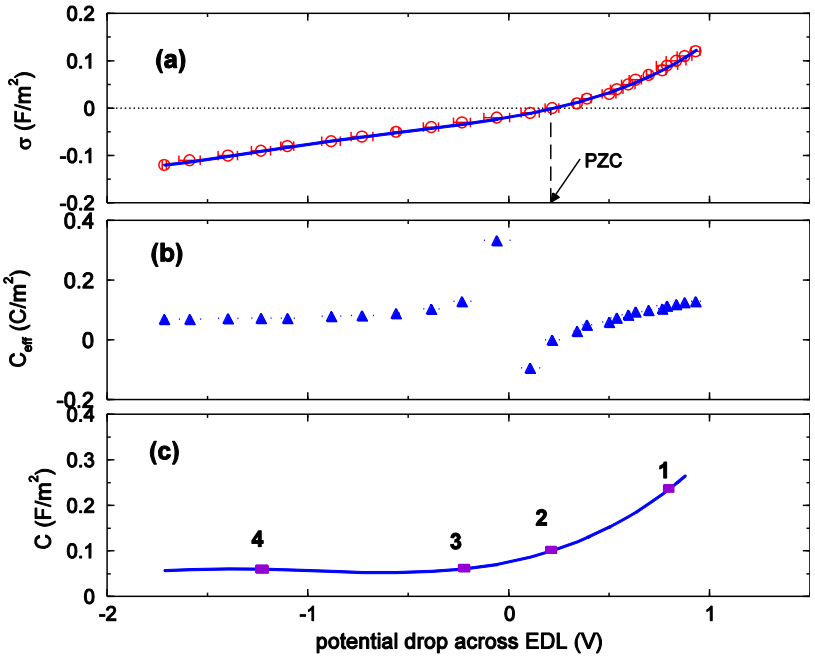

Figure 6.5: (a) Correlation between the electrode charge density and the electrical potential drop across the EDLs at the interface of [BMIM][NO_3] and planar electrodes. (b) Correlation between the effective EDL capacitance, $C_{\text{eff}} = \sigma / \phi_{EDL}$, and the electrical potential drop across the EDL for systems studied in this paper. (c) Correlation between the EDL differential capacitance, $C = d\sigma / d\phi_{EDL}$, and the electrical potential drop across the EDL.

Figure 6.5a shows the computed $\phi_{EDL} - \sigma$ correlation. In the literature, the EDL capacitance has been computed in two different ways. An effective EDL capacitance, C_{eff}, can computed by using $C_{\text{eff}} = \sigma/\phi_{EDL}$,[114] and a differential EDL capacitance, C, can be computed by using $C = d\sigma / d\phi_{EDL}$. Here, we computed the EDL capacitance using both approaches. When computing the differential capacitance, the $\phi_{EDL} - \sigma$ correlation was first fitted to a fourth-order polynomial, and the differential capacitance was then obtained by analytically differentiating the polynomial. Figure 6.5b and c shows the dependence of the effective capacitance, C_{eff}, and the differential capacitance, C, on the potential drop across the EDL, respectively. The effective capacitance, C_{eff}, shown in Figure 6.5b shows a trend similar to that reported for the EDL in high-temperature molten salts; that is, C_{eff} exhibits a discontinuity near the potential of zero charge (*PZC*) and decreases as the potential increases from *PZC* and increases as the potential decreases from the *PZC*.[114] We note that the negative capacitance near *PZC* is caused by the definition of C_{eff} and should not be confused with the negative differential capacitance discussed in the literature.[121] Since the differential capacitance has more detailed information on the charge storage capability of the EDL, we will focus on the differential capacitance in the rest of our discussion. An examination of the capacitance−potential (C−V) correlation shown in Figure 6.5c shows that (1) at positive electrode polarization, the EDL capacitance increases sharply as the electrode potential becomes more positive, and (2) at negative electrode polarization, the EDL capacitance varies only weakly as the electrode potential becomes more negative. These trends agree very well with those observed experimentally at the interface of [EMI][BF_4] and mercury

electrodes,[55] although they differ qualitatively from the bell-shaped and camel-like *C*−*V* curves obtained at the interface of [BMIM][Cl] and glassy carbon electrodes.[54] Below, we explore the molecular origins of trends of the *C*−*V* correlation shown in Figure 6.5c. To this end, we first establish the connection between the structure and the capacitance of an EDL and then investigate the dependence of the differential capacitance on positive and negative electrode polarizations.

6.3.1 Relation between EDL Structure and Capacitance

The differential capacitance is a macroscopic manifest of how the structure of the EDL near an electrode responds to a change of the electrode potential or surface charge density. To obtain a mathematical model for this, we consider the EDL near an open planar electrode with a surface charge density of σ and take a deeper examination on the potential distribution across the EDL based on Equation 6.1. As the boundary conditions show that the potential on the electrode is set to zero, the potential drop across the EDL should be

$$\phi_{EDL} = \phi(0) - \phi(L) = -\frac{1}{\varepsilon_0}\int_0^L z\rho_e(z)dz \qquad (6.2)$$

Here, the potential drop is obtained *always* by subtracting the potential in the bulk electrolyte from that on the electrode (one can image that, as the surface charge density on the electrode becomes more positive, the potential in the bulk will become smaller, i.e., the potential drop becomes larger, and vice versa). When the charge density of the electrode changes by a small amount, Δσ, there will be a corresponding change in the

space charge density (thereafter denoted as $\Delta\rho_e(z)$) inside the EDL. Because of the linearity of Equations 3.4 and 6.2 with respect to the space charge density, the change in the potential drop across EDL as the electrode surface charge density increases from σ to σ + Δσ ($\Delta\phi_{EDL}$) is

$$\Delta\phi_{EDL} = \phi_{EDL}|_{\sigma+\Delta\sigma} - \phi_{EDL}|_{\sigma} = -\frac{1}{\varepsilon_0}\int_0^L z\Delta\rho_e(z)dz \tag{6.3}$$

Since $C = \Delta\sigma / \Delta\phi_{EDL}$ and $\Delta\sigma = \int_0^L -\Delta\rho_e(y)dy$,

$$C = \frac{\varepsilon_0}{\int_0^L z(-\Delta\rho_e(z))dz / \int_0^L (-\Delta\rho_e(z))dz} = \frac{\varepsilon_0}{d_{eff}} \tag{6.4}$$

Equation 6.4 provides a connection between the differential capacitance of an EDL and how its microstructure changes as the charge density on the electrode changes. Interestingly, it shows that the differential capacitance of an EDL can always be casted into a form similar to the capacitance of the EDLs observing the Helmholtz model. However, there are distinct differences between this general model and the Helmholtz model. Specifically, in the Helmholtz model, $C = \varepsilon/d$, where ε is the permittivity inside the EDL and d is the distance between the counter-ion layer and the electrode. In the present model, which is more useful when the EDL is explicitly resolved at the atomistic scale, the vacuum permittivity is used, and d_{eff} is an effective separation. Mathematically, d_{eff} can be interpreted as the mean separation between points in EDL and the electrode weighted by the *variation of space charge density* ($-\Delta\rho_e(z)$) at these points when a

small charge is added to the electrode. Therefore, in the present model, the capacitance is not *directly* controlled by the separation between the counter-ion and the electrode, as in the Helmholtz model, but is directly controlled by how the variation of space charge density is distributed as a change in electrode charge density is introduced. For a given $\Delta\sigma > 0$, the $\Delta\rho_e(z)$ will be predominately negative in order to screen the increased electrode charge. In principle, the EDL capacitance can only be determined by using the distribution of $\Delta\rho_e(z)$. However, typically, the capacitance will be higher if the increased electrode charge $\Delta\sigma$ is screened at a shorter distance from the electrode by $\Delta\rho_e(z)$, since the integral $\int_0^L -z\Delta\rho_e(z)dz$ in Equation 6.4 tends to be smaller in such a case.

6.3.2 Capacitance at Positive Electrode Polarization

To understand the molecular mechanisms of the trends of the *C*−*V* correlation shown in Figure 6.5c, we selected two representative points on the *C*−*V* curve (point 1, with ϕ_{EDL} = 0.80 V and σ = 0.09 C/m^2, and point 2, with ϕ_{EDL} = 0.21 V and σ = 0 C/m^2) and investigate why the capacitance at point 1 is higher than that at point 2. To this end, we study the response of the EDL structure at these points as the electrode charge density σ increases. We will first show how and why the change of the ion number density is different at these operating points when the same small $\Delta\sigma$ is introduced. We next show how the different change in ion number density leads to different changes in space charge density and, thus, different capacitance at these two operating points.

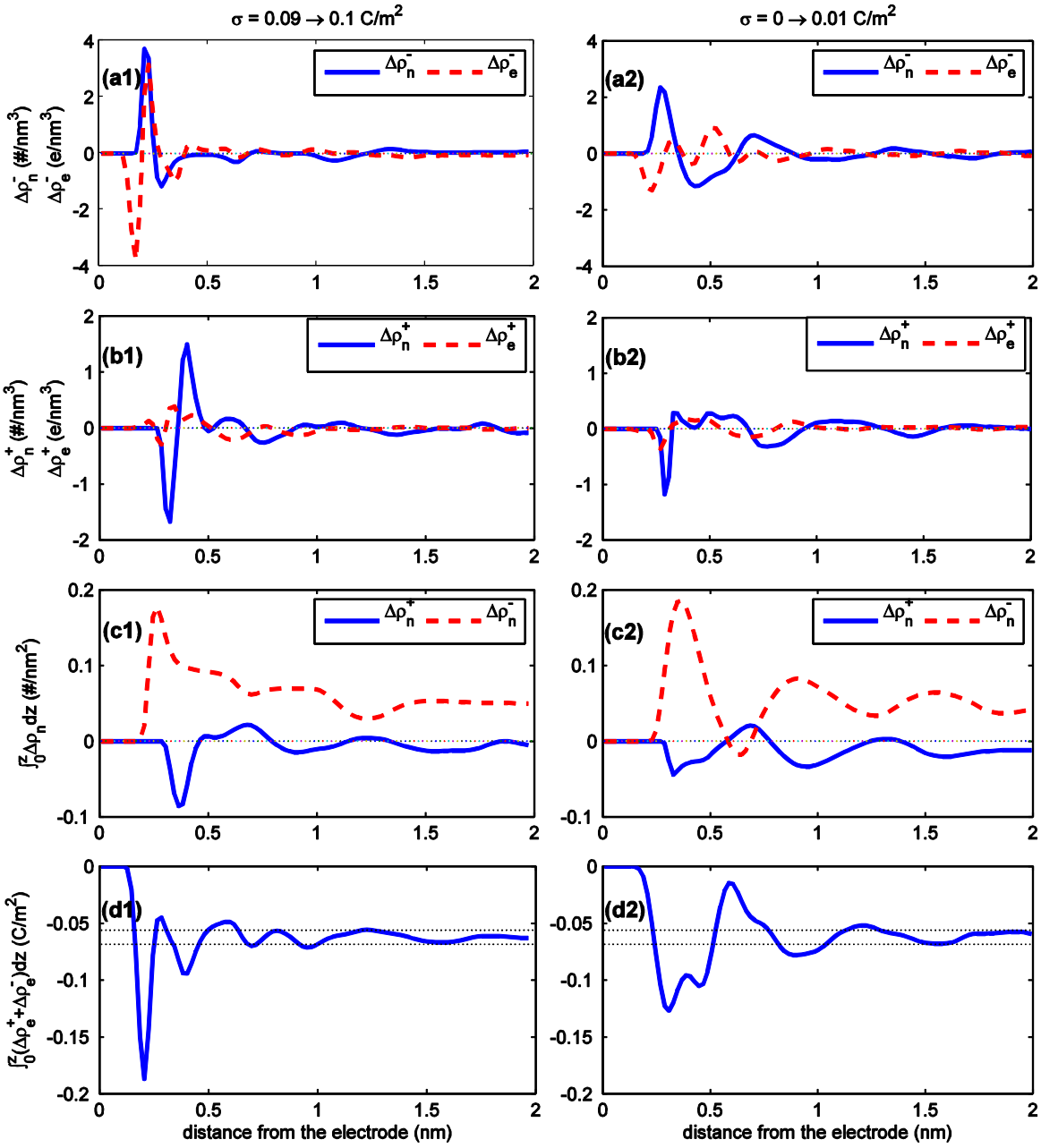

Figure 6.6: Response of the EDL structure at operating points 1 and 2 (see Figure 6.5c) as the electrode charge density increases by 0.01 C/m^2.

Figures 6.6a1 and a2 shows the variation of $[NO_3]^-$ density ($\Delta\rho_n^-$) at operating points 1 and 2 when σ increases by 0.01 C/m^2. Both figures show similar trend in $\Delta\rho_n^-$: a

distinct peak is observed next to the electrode, followed by alternating valleys and peaks; that is, as the electrode charge density increases, a large number of $[NO_3]^-$ ions are added to the region next to the electrode; meanwhile, some $[NO_3]^-$ ions are added/removed in other regions. The appearance of alternating peaks and valleys beyond the first $\Delta\rho_n^-$ peak is caused by the correlation between $[NO_3]^-$ ions. For example, the first $\Delta\rho_n^-$ valley appears because as more $[NO_3]^-$ ions accumulate in the first $[NO_3]^-$ layer near the electrode, their repulsive interactions with the $[NO_3]^-$ ions located at positions near the first $[NO_3]^-$ layer tend to deplete $[NO_3]^-$ ions at these positions. Such a depletion process is observed clearly by comparing the $[NO_3]^-$ ion density in the region 0.30 nm < z < 0.55 nm at different electrode charge densities (see Figure 6.1a). A key difference between the $\Delta\rho_n^-$ profiles at operating points 1 and 2 is that the first $\Delta\rho_n^-$ peak is closer to the electrode at operating point 1. This is mainly due to the stronger $[NO_3]^-$–electrode interaction at operating point 1. The accumulation of $[NO_3]^-$ ions in the region next to the electrode is favored by their electrostatic interactions with the electrode but is also hindered by the "desolvation effects"; that is, as a $[NO_3]^-$ ion moves toward the electrode, it becomes less "solvated" by the $[BMIM]^+$ ions due to geometrical confinement. We note that the importance of such "desolvation effects" has long been recognized in the study of high-temperature molten salts.[114] At point 1, where σ is higher, the first factor dominates, and thus, the added ions accumulate at nearly the closest approach to the electrode. At point 2, where σ is small, the second factor becomes important. Thus, ions accumulate at positions further away from the electrode. To further quantify how the

$[NO_3]^-$ ions are added into the EDL, we integrate the $\Delta\rho_n^-$ profile from the electrode toward the bulk IL. The results are shown in Figures 6.6c1 and c2. At operating point 1, we observe that the $[NO_3]^-$ ion added to the first $\Delta\rho_n^-$ peak and valley (0.2 nm < z < 0.60 nm) is nearly 100% of the total amount of the $[NO_3]^-$ ion added into the EDL. However, at operating point 2, the $[NO_3]^-$ ion added to the first $\Delta\rho_n^-$ peak and valley (0.2 nm < z < 0.61 nm) is close to zero; that is, effectively, no $[NO_3]^-$ ion is added into the region 0.2 nm < z < 0.61 nm. Such a difference is mainly caused by the desolvation effect, which significantly hinders the accumulation of $[NO_3]^-$ ion within a distance of ~0.68 nm from the electrode surface. Specifically, on the basis of the $[BMIM]^+$–$[NO_3]^-$ pair correlation function, the solvated radius of $[NO_3]^-$ ion is ~0.68 nm.[122] Therefore, a $[NO_3]^-$ ion will start to lose its "solvation" ions when it approaches the electrode surface closer than 0.68 nm. Figures 6.6b1 and b2 shows the variation of $[BMIM]^+$ density ($\Delta\rho_n^+$) at points 1 and 2 when σ increases by 0.01 C/m^2. Both parts of the figure show a $\Delta\rho_n^+$ valley near the electrode, followed by alternating $\Delta\rho_n^+$ peaks and valleys. Integrations of the $\Delta\rho_n^+$ profiles are shown in Figures 6.6c1 and c2. Comparison of the integration of $\Delta\rho_n^+$ and $\Delta\rho_n^-$ profiles indicates that, for both operating points 1 and 2, the change in the number of $[NO_3]^-$ ions inside the EDL is more than 3.75 times larger than that of the $[BMIM]^+$ ion. This suggests that the response of the EDL structure to a change in the electrode charge is dominated by the $[NO_3]^-$ ions.

Figures 6.6a1, a2 and b1, b2 also shows the changes of space charge density ($\Delta\rho_e^-$ and $\Delta\rho_e^+$) associated with the change in $[NO_3]^-$ and $[BMIM]^+$ ion density when the electrode charge increases by 0.01 C/m^2 at points 1 and 2. We observe that although the overall trends of $\Delta\rho_e$ profiles are similar to that of the $\Delta\rho_n$ profiles, these profiles do not match exactly. This is caused by the charge delocalization of the IL ions. Specifically, $\Delta\rho_e$ at a position *z* depends on the $\Delta\rho_n$ in its vicinity and the orientation of IL ions. For example, the positive $\Delta\rho_e^-$ in 0.2 nm < *z* < 0.29 nm is mainly a result of the positive $\Delta\rho_n^-$ in 0.17 nm < *z* < 0.25 nm and the fact that positively charged nitrogen atoms of the $[NO_3]^-$ ions centered in this region are located in 0.2 nm < *z* < 0.29 nm.

Since the total variation of space charge density is $\Delta\rho_e = \Delta\rho_e^+ + \Delta\rho_e^-$, using the $\Delta\rho_e^-$ and $\Delta\rho_e^+$ obtained above and Equation 6.4, one can prove mathematically that the EDL capacitance at point 1 is higher than that at point 2. However, to obtain a more intuitive, albeit qualitative, understanding of how these different $\Delta\rho_e$ profiles lead to different capacitance, we adopt a different approach here. As mentioned earlier, the EDL capacitance is typically higher if the increased electrode charge, $\Delta\sigma$, is screened at a shorter distance from the electrode by $\Delta\rho_e(z)$. To quantify this screening, we integrate the $\Delta\rho_e$ profiles from the electrode surface toward the bulk ILs. The results are shown in Figures 6.6d1 and d2. Figure 6.6d1 and d2 shows that the increased electrode charge ($\Delta\sigma$ = 0.01 C/m^2 = 0.0625 *e*/nm^2) is essentially screened at a position about 0.65 and 1.0 nm from the electrode at point 1 and point 2, respectively, thus confirming that the capacitance at point 1 is higher than that at point 2. To trace the molecular origins of the

different screening of $\Delta\sigma$ (and, thus, the capacitance) at these points, we first note that the screening of $\Delta\sigma$ is dominated by the addition of $[NO_3]^-$ ions into the EDL at both points 1 and 2. By correlating Figure 6.6 part d1 with parts c1 and a1, we next note that the effective screening of $\Delta\sigma$ at a small distance from the electrode at point 1 is mainly due to the closeness of the first $\Delta\rho_n^-$ peak to the electrode and the fact that nearly all $[NO_3]^-$ ions necessary to screen the increased surface charge are added to the region $z < 0.60$ nm. In contrast, at point 2, the effective screening of $\Delta\sigma$ is achieved at a larger distance from the electrode because the first $\Delta\rho_n^-$ peak is farther away from the electrode, and essentially, no additional $[NO_3]^-$ ion is added to the region $z < 0.61$ nm as the electrode charge density increases from 0.09 to 0.10 C/m^2.

To summarize, the response of EDL structure at positive electrode polarization to a change of electrode charge is dominated by the addition of $[NO_3]^-$ ions into the EDL. The addition of $[NO_3]^-$ ions into the EDL is controlled by both electrode−ion interactions and the desolvation effects. At high surface charge density (polarization), the electrode−ion interactions dominate, and many $[NO_3]^-$ ions are introduced at their closest approach to the electrode, and almost all $[NO_3]^-$ ions needed to screen the increased surface charge are introduced within 0.60 nm from the electrode, thus leading to a high capacitance. At low surface charge, the desolvation effects dominate, and the net number of $[NO_3]^-$ ions added to the region $z < 0.61$ nm, in which $[NO_3]^-$ ion experiences desolvation, is nearly zero. As such, a low capacitance is observed.

6.3.3 Capacitance at Negative Electrode Polarization

Here, we select two representative points on the *C*−*V* curve shown in Figure 6.5c, point 3 with $\phi_{EDL} = -0.20$ V and $\sigma = -0.03$ C/m^2 and point 4 with $\phi_{EDL} = -1.24$ V and $\sigma = -0.09$ C/m^2. We investigate why the capacitance at these points is similar by studying the response of the EDL structure to a change in the electrode charge.

Figures 6.7a1 and a2 shows the variation of $[BMIM]^+$ density ($\Delta\rho_n^+$) at operating points 3 and 4 when σ decreases by 0.01 C/m^2. Both parts of the figure show trends similar to those observed for the $[NO_3]^-$ ion in Figures 6.6a1 and a2. Figures 6.7b1 and b2 shows the variation of $[NO_3]^-$ density at operating points 3 and 4 under the same conditions. Both parts show a significant valley (i.e., removal of ions) in the region 0.2 nm ≤ *z* ≤0.5 nm because of the increased electrostatic repulsion by the electrode. This is followed by a peak (0.50 nm ≤ *z* ≤0.7 nm), which is caused by the increase of $[BMIM]^+$ ion near the electrode and the strong $[BMIM]^+$−$[NO_3]^-$ correlations. This peak induces another valley in the region (0.70 nm ≤ *z* ≤1.1 nm) due to the correlations between $[NO_3]^-$ ions. To quantify how many ions are added to (or removed from) the EDL as the electrode charge decreases by Δσ, we again integrate the $\Delta\rho_n$ profiles from the electrode toward the bulk IL; the results are shown in Figures 6.7c1 and c2. We observe that, at both operating points, (1) the total number of $[NO_3]^-$ ions removed from the EDL is much larger than the number of $[BMIM]^+$ ions added into the EDL, and (2) the total number of $[NO_3]^-$ ions removed in the first $\Delta\rho_n^-$ peak and valley is only a small fraction of the total number of $[NO_3]^-$ ions removed from the EDL. Observation 1 suggests that

the response of EDL structure to a change in electrode charge is dominated by the $[NO_3]^-$ ions, even at negative electrode polarization, which is different from the situations in aqueous electrolytes, in which the response of the EDL structure to a change in the electrode charge is typically dominated by the counter-ions. This phenomenon is caused by (1) unlike the EDLs in aqueous electrolyte, in which the co-ion density is low, there are a large number of co-ions inside the EDLs in ILs available for removal, and (2) a large number of $[BMIM]^+$ ions pack closely near the electrode at zero charge (see Figure 6.7a1). Therefore, as the electrode becomes more negatively charged, it is much more difficult to insert a bulky $[BMIM]^+$ ion into the densely packed EDL than removing a smaller $[NO_3]^-$ ion. Observation 2 is mainly caused by the strong correlations between $[NO_3]^-$ and $[BMIM]^+$ ions. Specifically, the removal of $[NO_3]^-$ ions from the region $z <$ 0.7 nm is hindered by the attractive forces exerted on these ions by the large number of $[BMIM]^+$ ions accumulated near the electrode. Such attractive forces do not depend strongly on the electrode charge density since the $[BMIM]^+$ ion accumulation near the electrode varies weakly with the electrode charge (see Figure 6.2a).

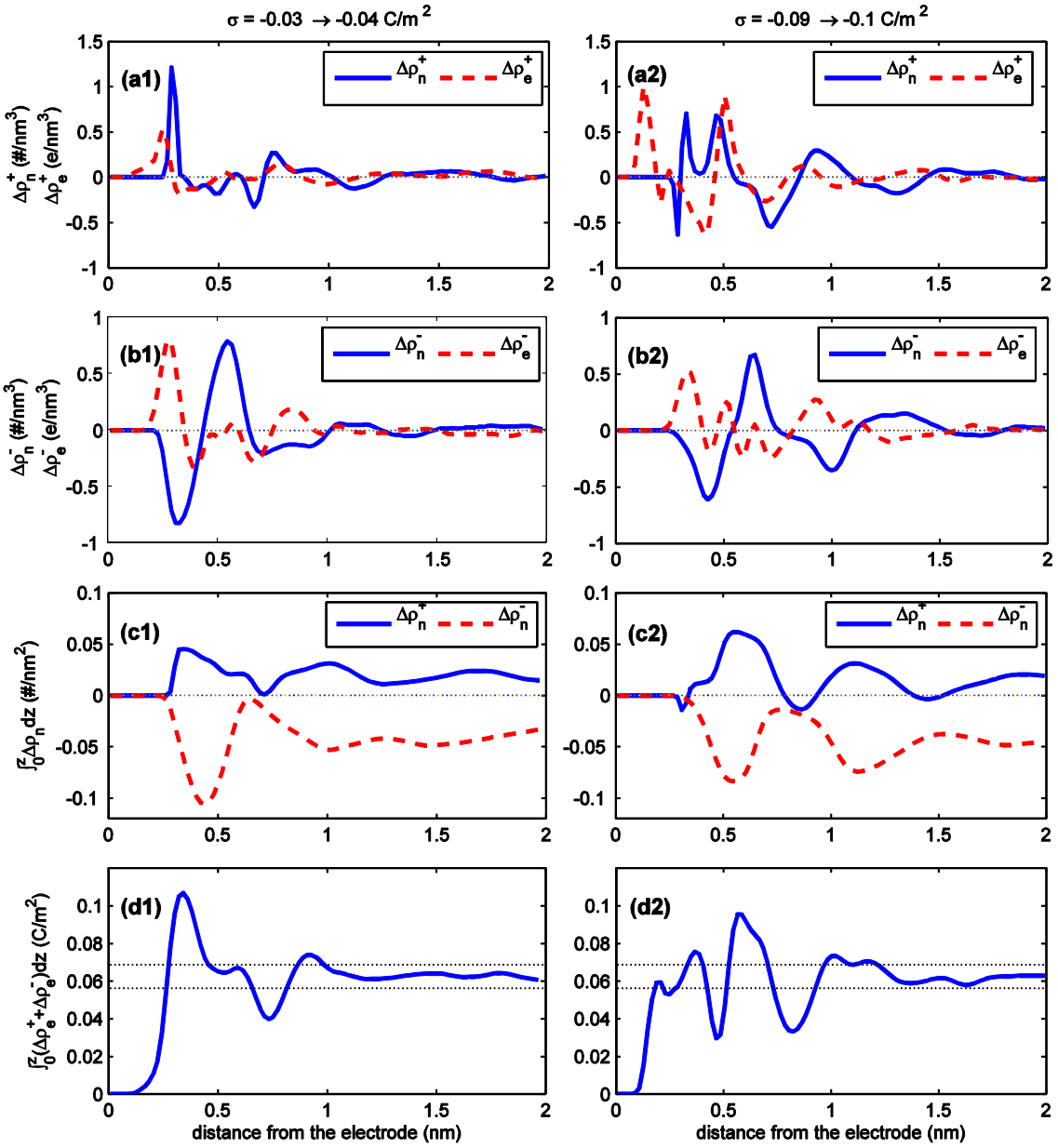

Figure 6.7: Response of the EDL structure at operating points 3 and 4 (see Figure 6.5c) as the electrode charge density decreases by 0.01 C/m^2.

Figures 6.7a1, a2 and b1, b2 also shows the changes of space charge density ($\Delta\rho_e^+$ and $\Delta\rho_e^-$) associated with the change in $[BMIM]^+$ and $[NO_3]^-$ ion density when the electrode charge decreases by 0.01 C/m^2 at points 3 and 4. Integration of these profiles

from the electrode surface toward the bulk ILs provides information on how the increased negative charge ($\Delta\sigma$) is screened by the variation of the space charge density ($\Delta\rho_e = \Delta\rho_e^+ + \Delta\rho_e^-$) inside the EDL. The results are shown in Figures 6.7d1 and d2. We observe that the $\Delta\sigma$ is effectively screened at a position ≈1.05 nm from the electrode at both operating points, which suggests that the capacitance at these two operating points is similar. By correlating Figure 6.7, parts d1, d2 with parts b1, b2 and a1, a2, we note that the effective screening of $\Delta\sigma$ at such a relatively large distance from the electrode originates from the fact that very few $[NO_3]^-$ ions are removed from the region z<0.7 nm due to the strong attractive force exerted on these ions by the $[BMIM]^+$ ions adsorbed on the electrode.

To summarize, the response of the EDL structure at negative electrode polarization to a decrease in the electrode charge is dominated by the removal of $[NO_3]^-$ ions from the EDL. Because the removal of $[NO_3]^-$ ions from the region near the electrode is hindered by their attractive interactions with the large number of $[BMIM]^+$ ions accumulated near the electrode, $[NO_3]^-$ ions are mainly removed from the region away from the electrode. Consequently, the capacitance is small. Since the aforementioned attractive interactions depend weakly on the electrode charge, the capacitance is insensitive to the electrode charge density.

6.3.4 Discussion

Although the differential capacitance of an EDL is one of its most important macroscopic properties, its current understanding is limited. The above results provide

new insights into this problem and point out possible directions to improve the current EDL models. First of all, the EDL capacitance in ILs does not depend simply on the closest approach between the counter-ion and electrode, as often assumed in the literature. For example, the closest approach between the $[NO_3]^-$ ion and the electrode reduces by 17% as the electrode potential increases from 0.21 to 0.80 V, but the capacitance increases by 140%. In addition, the results near a negatively polarized electrode suggest that the co-ion also plays a critical role in determining the EDL capacitance. Second, the cation−anion correlations and the significant adsorption of cations on the electrode at zero electrode charge can strongly affect the EDL capacitance. It will be worthwhile to systematically study these effects and incorporate them into theoretical EDL models. An exciting possibility with these effects is that they may explain the very diverse trends of *C*−*V* curves observed experimentally. For example, since the adsorption of ions on electrodes (and thus, the capacitance) depends strongly on their surface chemistry and the surface chemistry of electrodes made of even the same materials can differ significantly due to different fabrication details, it is possible that the diverse *C*−*V* correlations observed by different research groups originate from the different surface chemistries of the electrodes used by them.

Another important property of the EDL is the potential of zero charge of the electrode. On the basis of the data shown in Figures 6.5a and c, it was determined that the *PZC* of the present electrode is 0.21 V, whereas the potential at which the EDL capacitance reaches minimum is −0.5 V. This differs from the typical expectation that the *PZC* coincides with the minimum of the *C*−*V* curve. However, since not all physical

processes (e.g., the specific adsorption of ions on the electrodes) are accounted for in the present simulations, further studies are needed to clarify the relation between the *PZC* and the minimum of *C*−*V* curves in ILs.

6.4 Conclusions

The structure and capacitance of the EDLs at the interface of an IL [BMIM][NO_3] and planar electrodes were studied at various electrode surface charge densities by using classical MD simulations. The complex shape of the ions and their delocalized charge distribution are modeled explicitly, and the non-electrostatic interactions between ions and the electrodes are also accounted for.

The study of EDL structure near electrodes with different surface charge densities indicates that a Helmholtz-like interfacial counter-ion layer exists when the electrode charge density is negative or strongly positive but becomes not well-defined when the electrode charge density is weakly positive. However, regardless of the presence of a distinct Helmholtz layer, the charge separation (i.e., nonzero space charge locally) and orientational ordering of the ions persist to a depth up to 1.1 nm into the bulk ILs. These results support the composite EDL structure proposed in the literature.[50-51] Further analysis of these results suggests that structure of the EDL is affected strongly by the liquid nature of the IL and the short-range ion-electrode and ion−ion interactions, especially at low electrode charge densities. In addition, the charge delocalization is

found to affect the mean force experienced by the bulky ions near the electrode and, thus, can play an important role in shaping the EDL structure.

For the specific system studied here, the EDL capacitance is nearly constant under negative electrode polarization but increases dramatically with the electrode potential under positive electrode polarization. The capacitance is interpreted as a response of the EDL structure to a change in the electrode charge. It is found that the $[NO_3]^-$ ion dominates the response of EDL structure to the change in the electrode charge under both positive and negative electrode polarization. Detailed analysis shows that the cation−anion correlations and the strong adsorption of $[BMIM]^+$ ions on the electrode are responsible for the capacitance−potential correlation observed here.

CHAPTER 7

EFFECTS OF ION SIZE AND ELECTRODE CURVATURE ON EDLS IN IONIC LIQUIDS

As Chapter 6 shows, the nature of cations/anions ultimately plays a key role in determining the physicochemical properties of ILs and consequentially affects the structure and capacitance of EDLs in ILs near the planar electrodes. However, some questions are still not answered clearly. For instance, how would the ion size influence EDLs in ILs? What's the difference between the EDLs near planar electrodes and those on cylindrical surfaces? In addition, Figure 6.6d and Figure 6.7d both reveal that the electrode surface charge is overscreened by the charge inside the EDLs rather than compensated equivalently as the classical EDLs predicted. To deeper understand the fundamentals of the structure and capacitance of EDLs in ILs, we use classical MD to model ILs near planar/cylindrical electrodes with chemical details to gain the insights on the importance of ion size and electrode curvature on the EDLs in ILs.

7.1 Simulation System and Methods

We performed MD simulations of ILs in contact exohedrally[15] with planar and cylindrical electrodes modeled by graphene sheets and carbon nanotubes (CNTs), respectively. In the planar electrode simulations, ILs are enclosed between two planar electrodes (see Figure 7.1a), and the gap between two electrodes was set to 6.0 nm to produce a bulk-like behavior in the channel center. The size of the simulation box was

5.94 nm in both x- and y-directions. The coordinate system is defined such that z = 0 corresponds to the geometrical plane of the lower electrode. In the cylindrical electrode simulations, a (5,5) CNT with a diameter of 0.67 nm was placed at the center of a box of ILs (see Figure 7.1b). The length of CNT is 6.1 nm, pointing along z, and the size of simulation box along x- and y-directions was set to 6.0 nm, which is large enough to obtain a bulk-like behavior at positions far from the CNT. Three different surface charge densities (0, 0.112, and -0.112 C/m^2) were studied by assigning a net partial charge to the atoms of the electrode. [BMIM][Cl] and [BMIM][PF_6] were chosen as ILs due to their different anion size (the diameter of the Cl^- and PF_6^- ions are 3.62 Å and 5.10 Å, respectively[123]). The force field for the electrode atoms (carbon) was taken from Ref. [71]. The force fields for the $BMIM^+$ and PF_6^- ions were taken from Ref. [122], and the force field for the Cl^- ions was taken from Ref. [124]. Periodic boundary conditions were applied in x- and y-directions for simulations with planar electrodes, and in all three dimensions for simulations with CNT electrodes.

For each MD simulation, the number of ions in the system was tuned such that the ion concentration of the bulk-like region in the simulation with electrodes matched that of the pure bulk ILs. The PME method was used to compute the electrostatic interactions. Specifically, an FFT grid spacing of 0.12 nm and cubic interpolation for charge distribution were used to compute the electrostatic interactions in reciprocal space. A cutoff distance of 1.0 nm was used in the calculation of electrostatic interactions in the real space. The non-electrostatic interactions were computed by direct summation with a cutoff length of 1.0 nm. The LINCS algorithm[98] was used to maintain the bond length

and bond angles of the $BMIM^+$ and PF_6^- ions. In each simulation, we first heated the system to 1000 K, and then annealed to 365.15 K in 3 ns. The system was then allowed to equilibrate for another 6 ns to obtain an equilibrium state. Finally, a 50 ns production run was performed. To ensure statistical accuracy, each simulation case was repeated five times with different initial configurations.

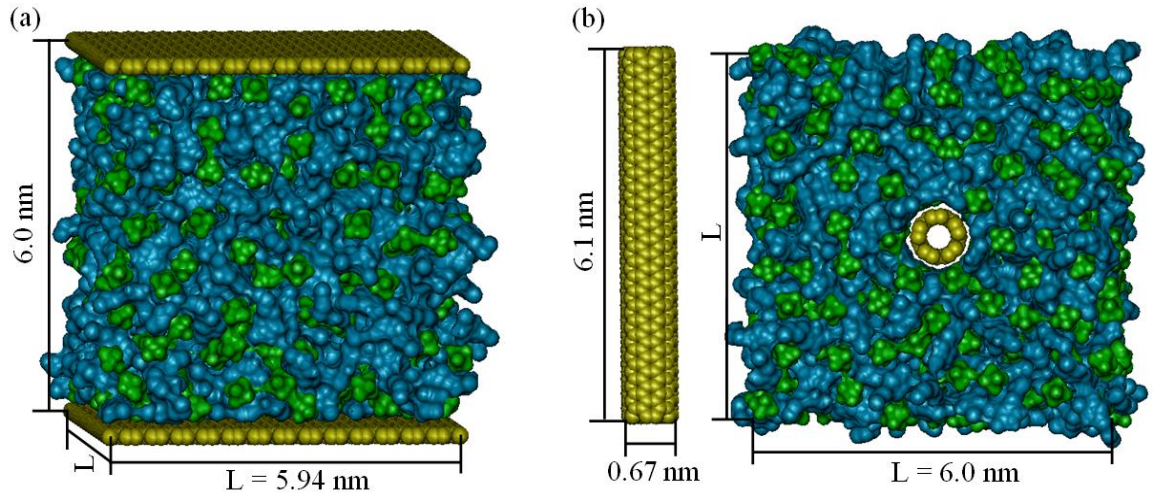

Figure 7.1: Snapshots of simulation system with graphene sheets (panel a) and CNT (panel b) as electrodes. The blue, green, and yellow spheres represent $BMIM^+$ ions, PF_6^- ions, and electrode atoms.

The microstructure of the EDL, e.g. ion number density and space charge density profiles, was obtained using the binning method. The capacitance of the EDL was computed by Equation 3.1 with attaining the potential distribution across the EDL. With space charge density obtained from simulations, the potential distribution near the planar electrode was calculated by Equation 6.1. Similarly, in the cylindrical electrode simulations, the space charge density, $\rho_e(r)$, in the radial direction can also be obtained from MD simulations. The boundary conditions for Equation 3.4 are considered as: (1)

the potential on the electrode surface was set as zero, i.e., $\phi(0) = 0$; (2) the derivative of potential is zero in bulk electrolytes far from the cylindrical electrodes when the EDL forms near the exohedral cylindrical surface (cf. Figure 7.1b or Figure 1.3e), i.e., $\left.\frac{d\phi}{dr}\right|_{bulk} = 0$. Then, the potential distribution can be calculated by solving Equation 3.4 as

$$\phi(r) = -\frac{1}{\varepsilon_0}\left[\int_R^r u\rho_e(u)\ln\frac{r}{u}du + R\sigma\ln\frac{r}{R}\right] \tag{7.1}$$

where R is the radius of exohedral cylindrical electrode surface. If the EDL formed inside a cylindrical pore with its inner surface having a radius of R (e.g., pores in Figure 1.3b and d), the second boundary condition will be $\frac{d\phi}{dr} = 0$ at the pore axis, and then the potential distribution between the inner surface and the pore axis along radial direction can be computed by

$$\phi(r) = -\frac{1}{\varepsilon_0}\int_R^r u\rho_e(u)\ln\frac{r}{u}du \tag{7.2}$$

Using Equations 6.1 and 7.1, in this work, the *PZC*s of the planar and cylindrical electrodes in contact with [BMIM][Cl] were found to be 414 mV and 458 mV, respectively. The former *PZC* value is very close to the value of 420 mV reported in a recent experimental study.[54] The *PZC*s of the planar and cylindrical electrodes in contact with [BMIM][PF_6] are both nearly zero, and the *PZC* at planar electrode is consistent with that reported for graphite surface in a recent MD simulation study.[125]

7.2 Ion Distribution at EDLs

For the distribution of $BMIM^+$, Cl^-, and PF_6^- ions and the orientation of $BMIM^+$ ions near neutral and electrified electrodes, we found trends similar to those reported earlier, regardless of the electrode curvature. For example, (1) $BMIM^+$ ions adsorb significantly on neutral and negatively charged electrodes.[62, 125-126] The first peak of their concentration profile is systematically located ~0.35 nm from the electrode surface. From the DFT calculations, a $BMIM^+$-surface distance of 3.44 Å was determined for a (9,0) CNT and 3.40 Å inside a defect-free graphene slit,[127] in remarkable agreement with MD results. This agreement provides evidence that the image charge model and potentials used in the classical MD simulations adequately capture the interactions at the interface. (2) MD simulations indicate that the cations and anions form alternating layers due to the strong cation-anion correlations, and the layering penetrates about 1−1.5 nm into the IL bulk.[29, 62] The strong ion-ion correlations also manifest from the co-adsorption of cations and anions on the electrode surface. We note that the co-adsorption of a cation and an anion onto a neutral CNT leads to a packing where the PF_6^- anion associates to the C2 position of the $BMIM^+$ cation. This leads to a "staggered-pair" packing at the nanotube surface that repeats both around the circumference and along the nanotube axis to give complete coverage, which agrees with the existence of the hydrogen bonding between anions and C2 atom of the imidazolium ring.[128-129] (3) The imidazolium ring of $BMIM^+$ ion becomes more parallel to the electrode, as the electrode charge density (σ) becomes more negative, and tends to be more vertical to the

electrode, as σ becomes more positive.[57, 126] With confirming above relatively generally characteristics of EDLs in ILs, below we focus on how the anion size and electrode curvature affect the EDL structure and capacitance.

7.2.1 Ion Size Effects

In Figure 7.2 we compare the density distribution (ρ_n) of ions in [BMIM][Cl] and [BMIM][PF_6] near neutral planar electrodes. We observe the following trends: (1) Comparing the Cl^- and PF_6^- ion density profiles adjacent to the first peak of the $BMIM^+$ ion profile, Cl^- ions spread in a wider region, but with a lower peak, and the Cl^- ion density peak is closer to the electrode than that of the PF_6^- ions. (2) The second peak of $BMIM^+$ ion profile is closer to the electrode, when the anion is Cl^-. These observations are closely related to the smaller size of Cl^- ions compared to PF_6^- ions. To understand observation 1, we note that the Cl^- ions adsorbed on the electrode (signified by the first peak of Cl^- ion profile) can approach the electrode closer than the PF_6^- ions due to their smaller size. However, the adsorption of PF_6^- ions is much stronger because the van der Waals force between the electrode atoms and ions, a key driving force for ion adsorption, is stronger for the polyatomic PF_6^- ion than for the monoatomic Cl^- ion. The densely packed PF_6^- ions adsorbed on the electrode prevent more PF_6^- ions approaching them. It follows that we observe a near depletion of PF_6^- ions in region 0.54 to 0.68 nm from the electrode, and such a phenomenon doesn't occur for the loosely packed Cl^- ions adsorbed on the electrode. Observation 2 is caused by the different size of the anions, i.e., the

densely packed PF_6^- ions in the first layer adjacent to the electrode prevent the second $BMIM^+$ layer from approaching too closely to the electrode.

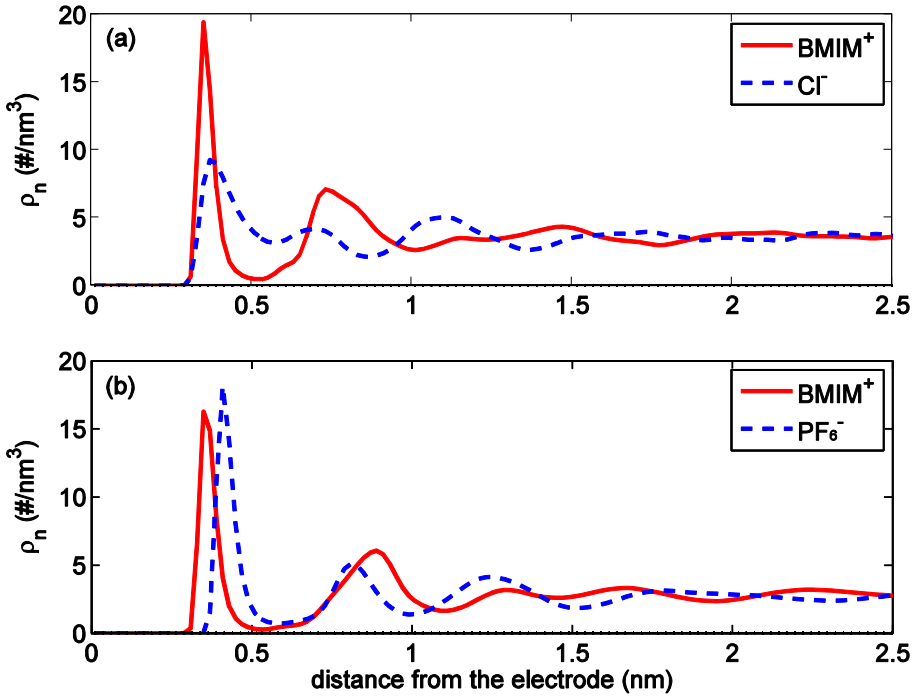

Figure 7.2: Ion number density profile in [BMIM][Cl] (panel a) and [BMIM][PF_6] (panel b) near neutral planar electrodes. The position of the cation and the anion are represented by the geometrical center of the imidazolium ring and the entire anion, respectively.

Figures 7.3a and 7.3b show the density distribution of ions near planar electrodes with $\sigma = 0.112$ C/m^2. A distinct $BMIM^+$ ion layer, located at z = 0.35 nm, follows closely the first Cl^- layer (see Figure 7.3a). However, such a $BMIM^+$ ion layer is not observed near the first PF_6^- layer in [BMIM][PF_6] (see Figure 7.3b). The smaller size of Cl^- ions is responsible for this difference. Specifically, although the adsorption of $BMIM^+$ ions is reduced by the electrostatic repulsion from the electrode, it is facilitated by the strong attraction between the anions and $BMIM^+$ ions. Such attraction is stronger for the smaller

Cl^- ions. In addition, because of their smaller size, Cl^- ions leave more space near the positive electrodes for the $BMIM^+$ ions.

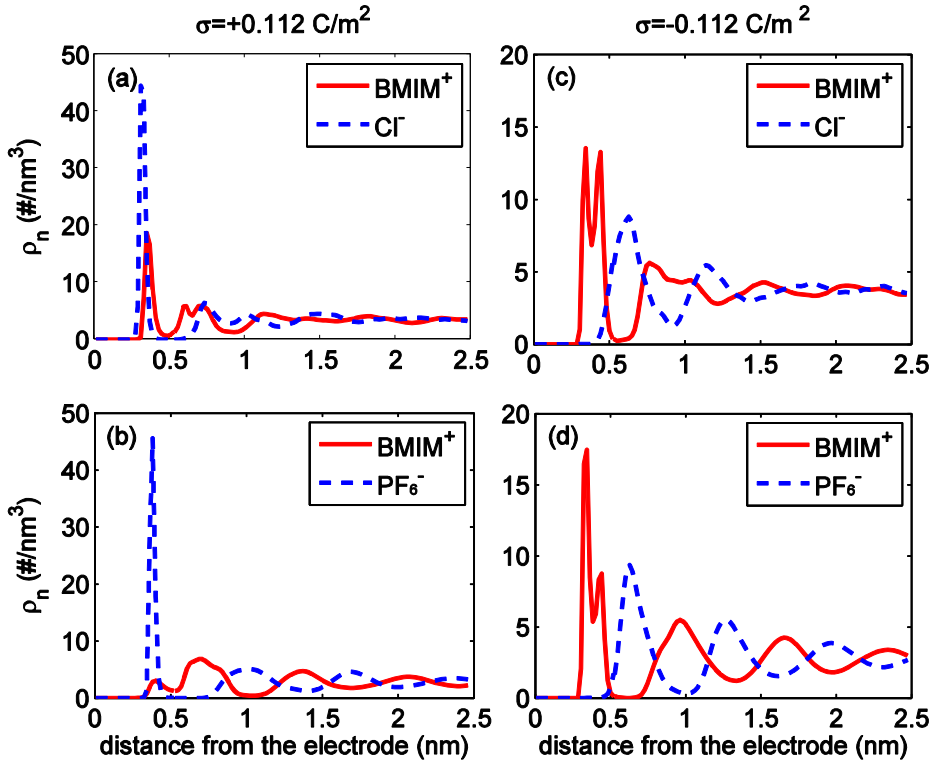

Figure 7.3: Ion number density profile in [BMIM][Cl] (panels a and c) and [BMIM][PF_6] (panels b and d) near positive and negative planar electrodes.

Figures 7.3c and 7.3d show the number density distribution of ions near planar electrodes with σ = -0.112 C/m^2. We observe that (1) the density profile of $BMIM^+$ ions shows two peaks (a doublet) at z = 0.35 nm and z = 0.45 nm from the planar electrodes in both Figures 7.3c and 7.3d, and (2) when Cl^- ion is the anion, the two peaks have similar height. However, when PF_6^- ion is the anion, the second peak becomes much lower than the first peak. To understand observation 1, we analyzed the molecular structure for the

systems of Figures 7.3c and 7.3d and found that the $BMIM^+$ ions in both peaks are contact-adsorbed on the electrode.

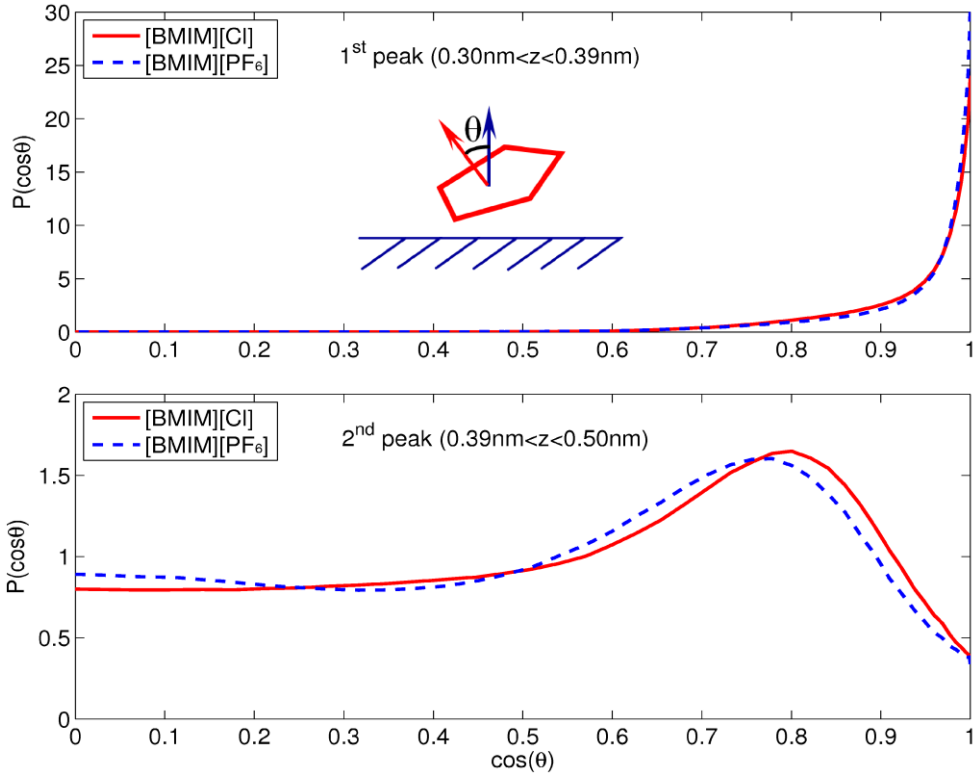

Figure 7.4: Distribution of the angle θ formed between the normal of imidazolium ring in the twin-peaks of $BMIM^+$ ion (see Figures 7.3c and 7.3d) and the normal direction of the electrode with $\sigma = -0.112 C/m^2$.

As shown in Figure 7.4, the imidazolium rings of $BMIM^+$ ions in the first peak are almost parallel to the electrode, while those of $BMIM^+$ ions in the second peak become more random. The formation of the doublet, or equivalently the different orientation of contact-adsorbed $BMIM^+$ ions, mainly arises from the incommensurate shape of the "flat" $BMIM^+$ ions and spherical Cl^-/PF_6^- ions. Specifically, the nearly spherical anions accumulated near the first $BMIM^+$ peak can't be packed effectively with

the $BMIM^+$ ions adsorbed on the electrode if all $BMIM^+$ ions lie parallel to the electrode. The second observation follows from the fact that more Cl^- ions accumulate in the region (0.44nm < z < 0.89 nm) very close to the negatively charged electrode, which forces more contact-adsorbed $BMIM^+$ ions to orient less parallel to the electrode to achieve a better packing with the Cl^- ions. The larger accumulation of Cl^- ions in this region is caused by its stronger attraction to the $BMIM^+$ ions than the larger PF_6^- ions.

The above results indicate that the size of anions affects the distribution of cations near both negatively and positively charged electrodes. At the most fundamental level, these effects originate from the different attractions between cations and anions with different size, which plays a key role in determining the ion distribution in EDLs inside ILs.

7.2.2 Curvature Effects

Figures 7.5a to 7.5d show the ionic density profiles in [BMIM][Cl] and [BMIM][PF_6] near CNT electrodes with $\sigma = \pm 0.112$ C/m^2, i.e., the same as for the planar electrodes used in Figures 7.3a to 7.3d. At $\sigma = 0.112$ C/m^2, the peaks of the anion concentration profiles (Cl^- ion in Figure 7.5a and PF_6^- ion in Figure 7.5b) are much lower than those shown in Figures 7.3a and 7.3b. In addition, the cation layer near the first peak of anion layer becomes higher (this is especially obvious in Figure 7.5b). Near the negative CNT electrodes, the doublet-peaks of $BMIM^+$ ions are replaced by a single peak, and the height of the first anion peak (Cl^- ion in Figure 7.5c and PF_6^- ion in Figure 7.5d) is not substantially changed. The reduced first counter-ion peak and enhanced first

co-ion peak are both caused by the reduced electrical field near exohedral cylindrical electrodes, compared with those near planar electrode with the same σ. Specifically, Gauss' law predicts that at the same distance from the electrode with the same σ, the electric field is weaker near cylindrical electrodes than near planar electrodes. This leads to reduced driving force for the counter-ion adsorption and co-ion desorption on the electrode, which in turn leads to the above observations.

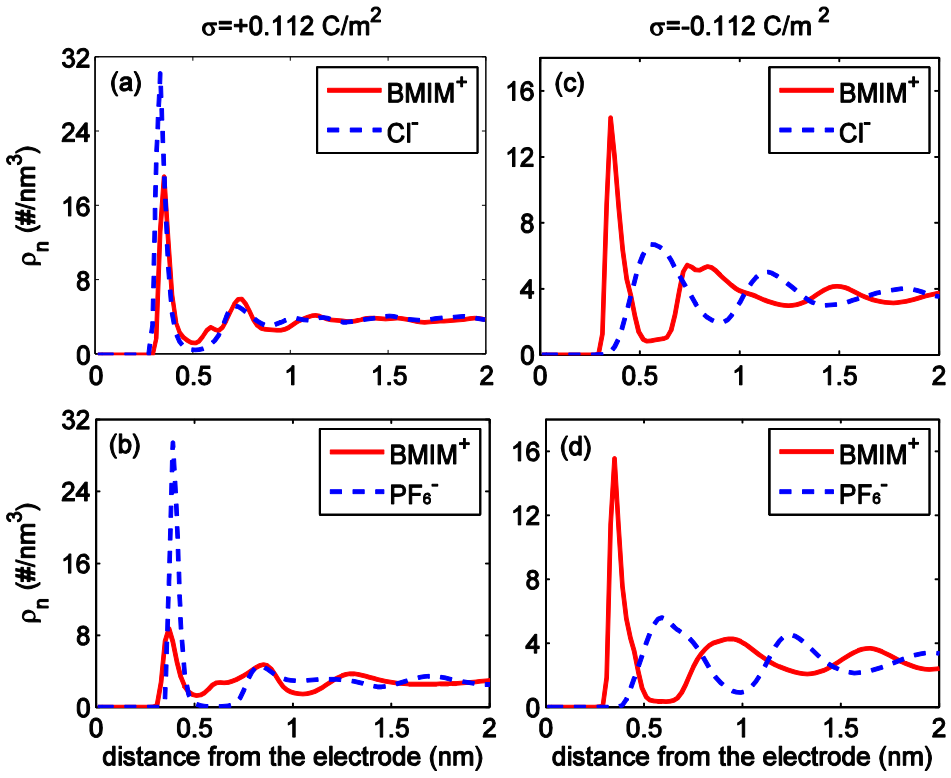

Figure 7.5: Ion number density profile in [BMIM][Cl] (panels a, c) and [BMIM][PF_6] (panels b, d) near positive (panels a, b) and negative (panels c, d) CNT electrodes.

7.3 Ion Size and Curvature Effects on EDL Capacitance

7.3.1 Results of EDL Capacitance

Figure 7.6 shows the capacitances of EDLs with different counter-ion/co-ion near planar/cylindrical electrodes with surface charge densities of $\sigma = \pm 0.112$ C/m^2. We note that the capacitance of EDLs in [BMIM][PF_6] is similar to that reported in Ref. [126]. We observe that near planar electrodes, the EDL capacitance as a function of the counter-ion type follows the order Cl^- > PF_6^- ≈ $BMIM^+$ (PF_6^- as co-ion) ≈ $BMIM^+$ (Cl^- as co-ion). Such an order is consistent with the expectation based on the classical Helmholtz model, i.e., EDL capacitance decreases as the counter-ion size increases.

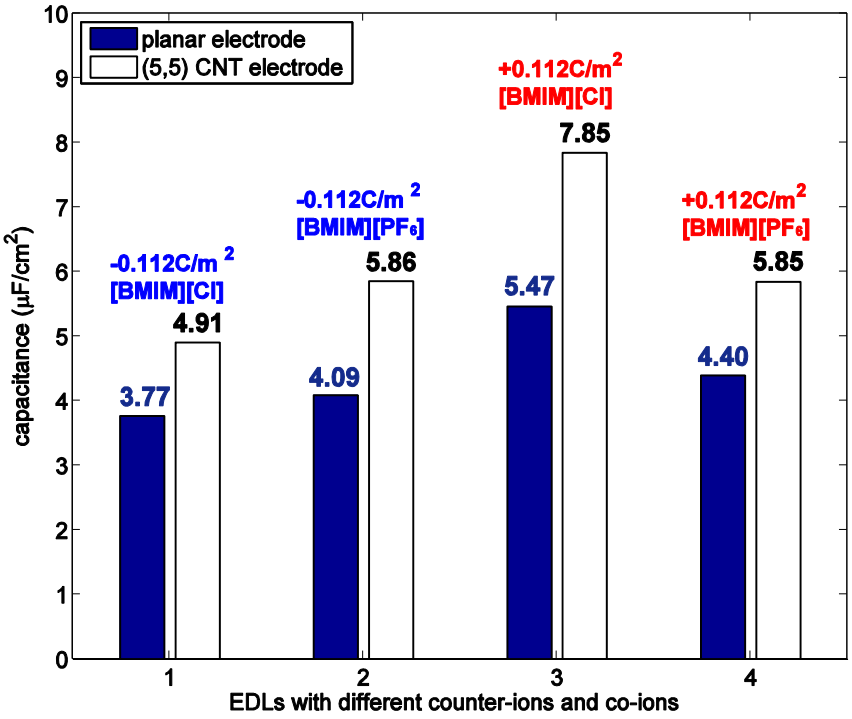

Figure 7.6: The capacitance of EDLs near planar and CNT electrodes with $\sigma = \pm 0.112$ C/m^2 in contact with different ILs.

Figure 7.6 also shows that for EDLs with the same counter-ion and co-ion, the capacitance increases by 30% − 44% as the electrode shape changes from planar to cylindrical. This enhancement of capacitance due to the electrode curvature is consistent with the prediction by the exohedral electrical double-cylinder capacitor (xEDCC) model,[130] i.e., for the same EDL thickness, the capacitance increases with increased electrode curvature. The above results demonstrate that the dependence of EDL capacitance on the ion size and electrode geometry is in qualitative agreement with available theories. However, to use these models to guide the optimization of EDL capacitance by exploiting ion specificity and electrode curvature effects, the accuracy of these models must be examined quantitatively. Below, we use the data from Figure 7.6 to examine the Helmholtz and xEDCC models.

7.3.2 Quantitative Examination of Helmholtz and xEDCC Models

Based on the Helmholtz model, the capacitance of an EDL near a planar electrode, C_∞, is given by

$$C_\infty = \frac{\varepsilon_\infty}{d_\infty} \tag{7.3}$$

where ε_∞ and d_∞ are the permittivity and thickness of the Helmholtz layer. Based on the xEDCC model, the capacitance of an exohedral EDL near an cylindrical electrode, C_c, is given by[131]

$$C_c = \frac{\varepsilon_c}{R\ln(1+\frac{d_c}{R})} \tag{7.4}$$

where, ε_c is the permittivity in the EDL, d_c is the separation between the counter-ion layer and the electrode surface, and R is the radius of the exohedral surface of the cylindrical electrode.

In principle, the accuracy of Equations 7.3 and 7.4 can be studied by comparing their prediction of C_∞ and C_c with simulation data. In practice, such comparison is not straightforward. Specifically, although d_∞ and d_c can be measured in MD simulations or experiments, ε_∞ and ε_c are difficult to obtain. In fact, the permittivity in EDLs at the interface of IL/electrode in the direction normal to the electrode is extremely difficult to compute.[132] At present, only the static dielectric constant in bulk ILs can be measured with accuracy,[131, 133] and experimental measurement of the dielectric constant of interfacial ILs has not been reported yet. Hence, it's unclear whether the dielectric constant in the EDL is the same as that in the bulk ILs. However, it is well-known that, for the EDLs in aqueous electrolytes, the dielectric constant in the Helmholtz layer can be 5 to 10 times smaller than that in bulk electrolytes.[82, 134-136] The direct evaluation of Equations 7.3 and 7.4 is difficult since it requires a precise permittivity value in the EDL. To avoid this difficulty, we test these models by examining the enhancement of EDL capacitance (η) due to the increased electrode curvature, i.e., we compute η as

$$\eta = C_c / C_\infty = \frac{\varepsilon_c}{\varepsilon_\infty} \frac{d_\infty}{R \ln(1 + d_c / R)} \tag{7.5}$$

Here we assume that $\varepsilon_c \approx \varepsilon_\infty$, i.e., the dielectric permittivity is the same for ILs near electrodes with different curvature but the same surface charge density. Although this

assumption is not ideal, it's far less restrictive than other assumptions such as assuming $\varepsilon_c \approx \varepsilon_{bulk}$. With this proviso, we obtain

$$\eta = C_c / C_\infty = d_\infty / R \ln(1 + d_c / R) \tag{7.6}$$

Testing the accuracy of Equation 7.6 requires the thickness of the EDL, i.e., d_∞ and d_c, as input parameters. However, d_∞ and d_c can be identified without ambiguity only when three conditions are met simultaneously, i.e., (a) the electrode charge is screened exactly by a single layer of counter-ions, (b) the electric charge of each counter-ion is centralized on a single atom, and (c) there is no charge separation in the electrolyte near neutral electrodes. However, the ion concentration profiles (see Figures 7.2, 7.3, and 7.5) and the delocalized nature of ion's charge in ILs indicate that none of these conditions is rigorously satisfied for the EDLs in ILs. Consequently, there are several possible choices when evaluating EDL thickness from MD data. Specifically, if the number density profiles of counter-ions and net charge density profiles near electrodes with a surface charge density of σ, i.e., $\rho^{\sigma}_{n,counter-ion}$ and ρ^{σ}_{e}, are given, then the EDL thickness near a charged electrode may be obtained from the following three choices:

1. the distance between the first peak of $\rho^{\sigma}_{n,counter-ion}$ and the electrode surface, i.e., the EDL thickness is based on ρ^{σ}_{n};
2. the distance between the first peak of the profile $\Delta\rho^{\sigma}_{n,counter-ion} = \rho^{\sigma}_{n,counter-ion} - \rho^{0}_{n,counter-ion}$ to the electrode surface, i.e., the EDL thickness is based on $\Delta\rho^{\sigma}_{n}$;

3. or the distance between the first peak of the profile $\Delta\rho_e^\sigma = \rho_e^\sigma - \rho_e^0$ to the electrode surface, i.e., the EDL thickness is based on $\Delta\rho_e^\sigma$.

Choice 1 is the most frequently adopted choice in the literature. It amounts to neglecting the ion charge delocalization, the ion adsorption on neutral electrodes, and the charge separation beyond the first counter-ion layer. With choice 2 the ion charge delocalization and the charge separation beyond the first counter-ion layer are ignored. Choice 3 is equivalent to neglecting the charge separation beyond the first space charge density peak. The capacitance predicted by Equation 7.6 using EDL thickness following choices 1 and 2 are similar. For brevity, we present the examination of Equation 7.6 using EDL thickness defined with choices 2 and 3. Figures 7.7a-d show $\Delta\rho_n^\sigma$ and $\Delta\rho_e^\sigma$ for [BMIM][Cl] adjacent to planar electrodes with $\sigma = \pm 0.112$ C/m^2. In these figures, z = 0 corresponds to the electrode surface. We retrieve d_∞ using the $\Delta\rho_n$ and $\Delta\rho_e$ profiles shown in Figure 7.7, and the results are listed in Table 7.1. Note that when the $\Delta\rho_e$ has two closely-spaced peaks (e.g., in Figure 7.7d), the position of an "effective" first peak of the $\Delta\rho_e$ profile is taken as geometrical center of such peaks. Using similar method, d_c for the EDLs in [BMIM][Cl] adjacent to CNT electrodes and d_∞ (d_c) in [BMIM][PF_6] adjacent to planar (CNT) electrodes were retrieved and listed in Table 7.1. Ultimately, η can be computed using Equation 7.6, and the results are summarized in Table 7.1.

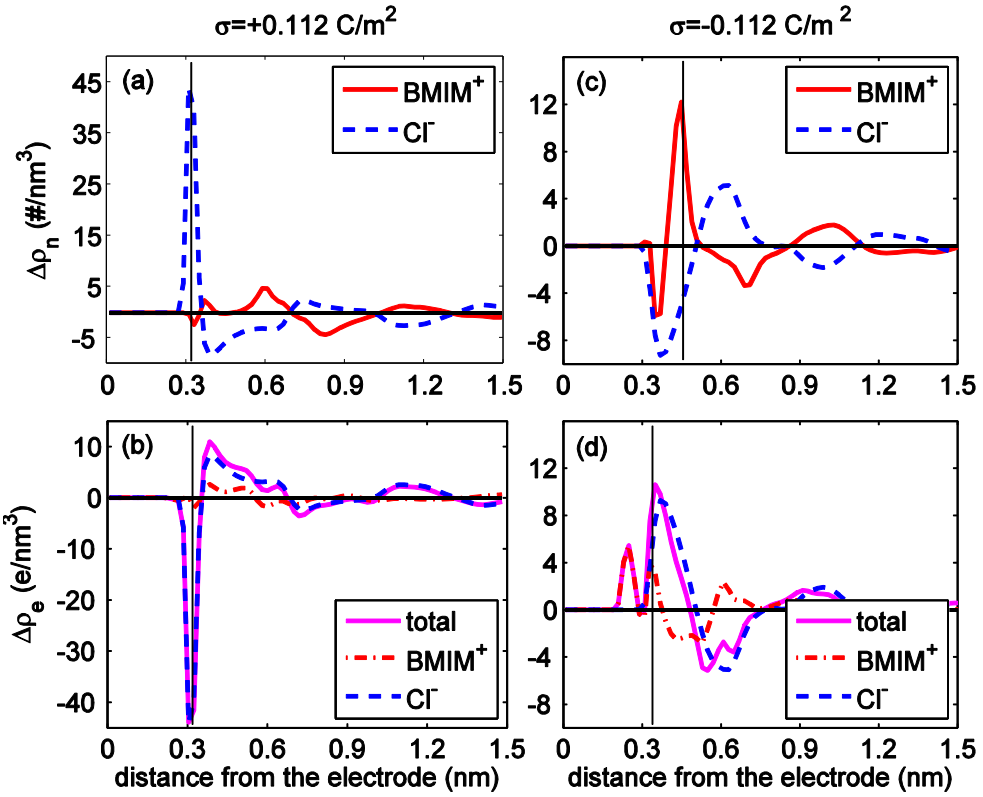

Figure 7.7: Change of ion number densities (panels a and c) and space charge densities (panels b and d) in [BMIM][Cl] near planar electrodes as the electrode charge density is changed from zero to ± 0.112 C/m^2.

Table 7.1: The EDL thickness based on different choices described in the text and comparison of curvature-induced capacitance enhancement predicted by Equation 7.6 and MD simulations.

Counter-ion	**$BMIM^+$**		**$BMIM^+$**		**Cl^-**		**PF_6^-**	
Co-ion	**Cl^-**		**PF_6^-**		**$BMIM^+$**		**$BMIM^+$**	
$d_\infty(d_c)$ based on:	$\Delta\rho_n$	$\Delta\rho_e$	$\Delta\rho_n$	$\Delta\rho_e$	$\Delta\rho_n$	$\Delta\rho_e$	$\Delta\rho_n$	$\Delta\rho_e$
d_∞ (nm)	0.44	0.34	0.41	0.33	0.31	0.31	0.39	0.29
d_c (nm)	0.39	0.35	0.39	0.33	0.33	0.33	0.39	0.29
$\eta = C_c / C_\infty$ **(Equation 7.6)**	1.70	1.42	1.58	1.44	1.35	1.35	1.51	1.39
$\eta = C_c / C_\infty$ **(MD)**	1.30		1.43		1.44		1.33	

We observe that the relative error in η predicted by Equation 7.6 using $\Delta\rho_n^\sigma$-based d_∞ and d_c is about 6%-31%, while the error in η predicted by Equation 7.6 using $\Delta\rho_e^\sigma$-based d_∞ and d_c is about 1%-10%. These results suggest that EDL thickness based on $\Delta\rho_n^\sigma$ and $\Delta\rho_e^\sigma$ can both provide a moderately accurate prediction of η, although the accuracy is better if an EDL thickness based on $\Delta\rho_e^\sigma$ is used. The fact that EDL thickness based on $\Delta\rho_n^\sigma$ gives a poorer prediction of η is expected, because EDL capacitance is most directly related to the change of space charge density rather than ion number density as the electrode is electrified. Another more subtle reason is as follows. $\Delta\rho_e^\sigma$ shown in Figure 7.7 is significantly affected by the change in anion concentration as the electrode is electrified even near electrodes with negative surface charge density (similar phenomenon has also been found in our earlier studies[62]). Hence, $\Delta\rho_{n,counter-ion}$ profile is a poorer identification of the change of EDL structure than $\Delta\rho_e^\sigma$, as an electrode is electrified, which in turn leads to poorer prediction of the EDL capacitance.

In summary, the above discussions suggest that, despite the rich structure of EDLs in ILs, if the EDL-thickness is suitably parameterized (in particular, if the EDL thickness is based on the change of space charge density as the electrode is electrified), the Helmholtz and xEDCC models can predict the EDL capacitance within reasonable accuracy.

7.4 A New Capacitance Model for EDLs in ILs

Although the Helmholtz and xEDCC models can predict EDL capacitance values with reasonable accuracy, they constitute quite crude simplifications of the actual EDLs in ILs. The fundamental assumption of these models is that the electrode charge is screened by a single layer of counter-ions adsorbed on the electrode surface and the electrolytes beyond this single layer are structureless. This assumption is in contradiction with the alternating layering of counter-ion/co-ions observed in ILs. It is therefore desirable to develop more elaborate models for the EDLs in ILs. Prior studies have led to interesting models for EDLs in ILs from mean-field theories. However, due to the complicated nature of EDLs in ILs, a number of assumptions had to be made in a mean-field approach, e.g., ion-ion correlations are neglected to a large extent. Consequently, some important features of the EDLs cannot be described by these models. Here we take a more phenomenological approach with the objective of capturing key features of the EDLs observed in MD simulations.

As shown in Figures 7.2, 7.3, 7.5, and 7.7, the alternating layering of ions adjacent to the electrode is one key feature of the EDLs in ILs. The layer alternation becomes weaker as the position moves further from the electrode. The overscreening of electrode charge is another key feature of the EDLs in ILs. It is known that, in concentrated ionic systems, the strong ion-ion correlation can lead to overscreening of the electrode charge. The overscreening of electrode charge in ILs was perhaps first envisioned by Kornyshev and was subsequently observed in a model IL made of charged

Lennard-Jones spheres.[50, 58, 64] In our current simulations, in which the ILs are modeled with chemical details (e.g., complex shape and charge delocalization), we also observed the similar phenomena. To quantify the charge overscreening, similar as Equation 5.3, we take the charge screening factor as

$$\beta(z) = -\int_0^z \Delta\rho_e^\sigma(s)ds/\sigma \tag{7.7}$$

near planar electrodes, and

$$\beta(r) = -\int_R^r \frac{s}{R}\Delta\rho_e^\sigma(s)ds/\sigma \tag{7.8}$$

near cylindrical electrodes. At positions with $\beta >$ 1.0, the electrode charge is overscreened.

Figure 7.8 shows the charge screening factor β near planar and CNT electrodes with σ = 0.112 C/m^2. We observe that β always exceeds 1.0 at a position near the first counter-ion concentration peak (see Figures 7.3 and 7.5). Beyond this position, β oscillates around 1.0 and the oscillation becomes weaker as the distance from the electrode increases. Similar trends have also been observed in the simulations of IL [BMIM][NO_3].[137] Therefore, we conclude that the overscreening of electrode charge is a universal feature of the EDLs in ILs.

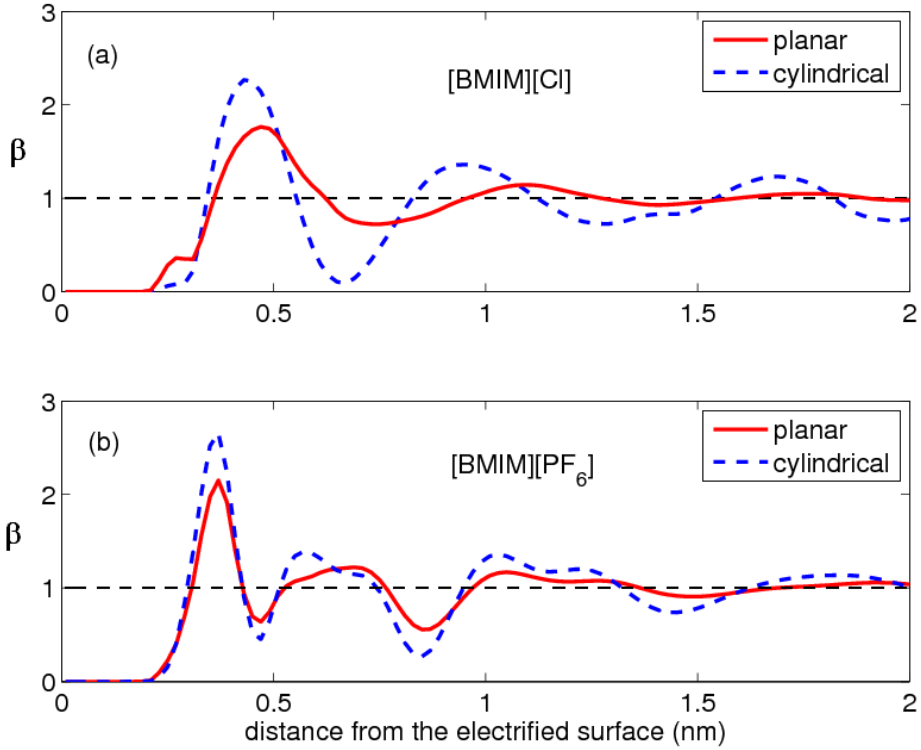

Figure 7.8: The charge screening factor β in [BMIM][Cl] (panel a) and [BMIM][PF_6] (panel b) near negative planar/cylindrical electrodes. The electrode charge density is -0.112C/m^2 in all cases.

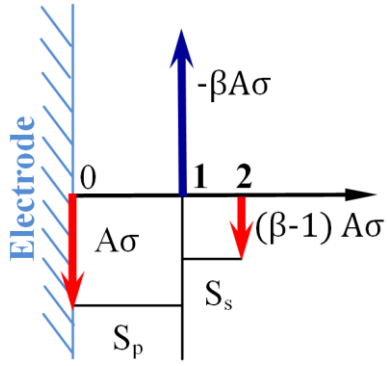

Figure 7.9: A schematic of the "multiple ion layers with overscreening" (MILO) model. The charge of the electrode (Aσ), the first counter-ion layer (-βAσ), and the adjacent co-ion layer ((β-1)Aσ) are assumed to be localized at positions 0, 1 and 2.

In this work, we propose a "Multiple Ion Layers with Overscreening" (MILO) model for the EDLs in ILs to take into account the alternating layering of ions adjacent to the electrode and the overscreening of the electrode charge. Figure 7.9 shows a schematic of the MILO model. In essence, we assume that the EDL consists of a counter-ion layer that overscreens the electrode charge and an adjacent co-ion layer. The counter-ion layer is located at a distance S_p from the electrode, and the net charge of this layer is $-\beta A\sigma$, where β is the charge overscreening factor at position S_p. σ and A are the charge density and area of the electrode surface, respectively. The excess charge of the counter-ion layer is balanced exactly by the adjacent co-ion layer located at position S_s from the counter-ion layer. Note that the layering of ions beyond the first two layers is much weaker and is therefore neglected. Using elementary electrostatic theory, the capacitance of EDLs near planar and CNT electrodes described by the MILO model is found to be

$$C_\infty = \frac{\varepsilon_\infty}{S_p^\infty - (\beta_\infty - 1)S_s^\infty} \tag{7.9}$$

$$C_c = \frac{\varepsilon_c}{R[\ln(1+\frac{S_p^c}{R}) - (\beta_c - 1)\ln(1+\frac{S_s^c}{R+S_p^c})]} \tag{7.10}$$

where the superscripts ∞ and c denote planar and cylindrical electrodes, respectively. Note that in the limit of β = 1, Equations 7.9 and 7.10 reduce to Equations 7.3 and 7.4, respectively. The parameters of Equations 7.9 and 7.10 include S_p, S_s and β. The values of S_p and S_s can be deduced from the size of the counter-ions and co-ions.

Determining β, however, is more difficult. In principle, β can be derived from more advanced models. In this work, we focus on the predicting power of Equations 7.9 and 7.10 for the EDL capacitance for a given value of β. To test Equations 7.9 and 7.10 based on the MILO model, we again adopt the approach used in Section 7.3 to circumvent the difficulty of obtaining precise value of dielectric constant in EDLs by studying the enhancement of EDL capacitance due to electrode curvature. Specifically, assuming $\varepsilon_c \approx \varepsilon_\infty$, Equations 7.9 and 7.10 predict that the enhancement of EDL capacitance by the electrode curvature follows

$$\eta = \frac{C_c}{C_\infty} = \frac{S_p^\infty - (\beta_\infty - 1)S_s^\infty}{R[\ln(1+\frac{S_p^c}{R}) - (\beta_c - 1)\ln(1+\frac{S_s^c}{R+S_p^c})]} \tag{7.11}$$

The predicted enhancement of EDL capacitance near a CNT electrode over that near a planar electrode, η, is compared to that computed directly from MD simulations in Table 7.2. We observe that relative error of prediction by Equation 7.11 is about 5% except for EDLs in [BMIM][Cl] adjacent to electrode with σ = -0.112 C/m^2, where the relative error is about 14%.

The agreement between the MD data and the prediction made with Equation 7.11 suggests that the MILO model is capable of capturing some of the essential physics of EDLs in ILs. Although the accuracy of the prediction by Equation 7.11 is comparable to that of the Helmholtz/xEDCC models, the new model can potentially explain other phenomena that are difficult to explain within the framework of these prior models. For example, Equation 7.11 predicts that charge overscreening tends to lead to an increase in

EDL capacitance. Since charge overscreening generally decreases as the electrode potential (or the electrode surface charge density) increases,[64] Equation 7.11 provides a possible way for understanding the decreased capacitance of EDLs as the electrode potential increases, which is hard to achieve using the classical Helmholtz model, since the EDL thickness is known to change little as the electrode potential changes.[62] The next step in developing the MILO model is to compute β self-consistently without using MD simulations, and work along this line is currently under way.

Table 7.2: Key parameters of the MILO model measured in MD simulations and comparison of curvature-induced capacitance enhancement predicted by Equation 7.11 and MD simulations.

Counter-ion	**$BMIM^+$**	**$BMIM^+$**	**Cl^-**	**PF_6^-**
Co-ion	**Cl^-**	**PF_6^-**	**$BMIM^+$**	**$BMIM^+$**
β_∞	1.76	2.08	2.26	1.86
β_c	2.25	2.60	2.73	2.56
S_p^∞ (nm)	0.47	0.37	0.36	0.33
S_s^∞ (nm)	0.16	0.06	0.15	0.04
S_p^c (nm)	0.45	0.37	0.37	0.34
S_s^c (nm)	0.10	0.06	0.17	0.03
$\eta = C_c / C_\infty$ **(Equation 7.11)**	1.48	1.49	1.38	1.39
$\eta = C_c / C_\infty$ **(MD)**	1.30	1.43	1.44	1.33
Relative error	13.8%	4.2%	4.2%	5.3%

7.5 Conclusions

We studied the structure and capacitance of the EDLs in ILs with $BMIM^+$ cations and Cl^-/ PF_6^- anions using MD simulations. The size of the anions is found to affect the position/height of the $BMIM^+$ ion concentration peak near both positive and negative electrodes. At the most fundamental level, these effects stem from the different attractions between cations and anions with different sizes. However, regardless of the anion size, overscreening of the electrode charge was observed in all the EDLs studied, suggesting that it is a universal feature of the EDLs in ILs. We note that the overscreening for ILs is also related to their efficiency in exfoliating carbon nanotube bundles and graphite. For EDLs with different counter-ions, we found that the capacitance of the EDLs follows the order: $BMIM^+$ (Cl^- as co-ion) ≈ $BMIM^+$ (PF_6^- as co-ion) ≈ PF_6^- < Cl^- near both planar and cylindrical electrodes. For the same counter-ion/co-ion and electrode charge density, the EDL capacitance is higher near cylindrical electrodes. These trends are consistent with the expectations from the Helmholtz and xEDCC models. Using the EDL structure and capacitance data obtained from the MD simulations, we examined the accuracy of the Helmholtz and xEDCC models, and found that, if the EDL thickness is suitably parameterized, these models can predict the EDL capacitance with good accuracy despite the dramatically simplified EDL structure assumed.

To account for the two critical features of the EDLs in ILs, namely, the alternating layering of cations and anions near the electrode and the overscreening of electrode

charge, we propose a “Multiple Ion Layers with Overscreening” (MILO) model for the EDLs in ILs. The capacitance computed from the MILO model agrees well with the MD prediction, although at present, some input parameters of the MILO model must be obtained from MD simulations. However, we emphasize that the MILO model provides a new framework for understanding many interesting and important aspects of EDLs in ILs, in particular, the dependence of EDL capacitance on the electrode potential, which is very difficult to rationalize using the classical EDL models.

CHAPTER 8

CONCLUSIONS

The fundamental understanding of EDLs in ECs is the key to design an EC with desired performance. To obtain such fundamentals by examining the structure, capacitance, and dynamics of EDLs, we used atomistic simulations methods to study the molecular physics of EDLs at the interfaces of different electrolytes and electrodes with different pores.

First, we studied the distribution of K^+ ions in electrified slit-shaped micropores with pore widths ranging from 9.36 Å to 14.7 Å using MD simulations. The ion distributions and their physical origins are found as follows.

1. In slit pores with widths larger than or equal to 14.7 Å, K^+ ions form separate layers near each slit wall and the ion distribution is in qualitative agreement with the prediction from the classical EDL theories, i.e., the long-range electrostatic ion-ion repulsion and the non-electrostatic ion-slit wall attractions, driving ions towards the two slit walls, are responsible for the ion accumulation on each wall.
2. In slit pores with pore widths between 10 Å and 14.7 Å, the K^+ ion distribution differs qualitatively from that described by EDL theories. In those pores most K^+ ions are fully hydrated and accumulate primarily in the central plane of the slit pores, which is caused majorly by the ion hydration effects.
3. In the pore with a width narrower than 10 Å, most K^+ ions are partially dehydrated and again form separate layers near each slit wall. In such a

transition, the electrostatic ion-ion repulsion plays a minor role. Instead, the enthalpic effects associated with the interactions between the hydration water molecules of a K^+ ion with their surrounding water molecules were found to lead to this interesting behavior.

Based on the observation that counter-ions form a single layer midway between the opposing walls in slit pores between 10 and 14.7 Å in width, we proposed a new sandwich capacitance model to describe the capacitance of EDLs formed by counter-ions enclosed in charged slit-shaped micropores. This model is capable of predicting the anomalous enhancement of capacitance experimentally observed in micropores.

Second, for the organic electrolyte of $TEABF_4$/ACN near planar electrodes, we examined the solvation of organic ions, and the structure, capacitance, and dynamics of the EDLs in the electrolyte using molecular dynamics simulations. The solvation of TEA^+ and BF_4^- ions is found to be much weaker than that of small inorganic ions, and the ACN molecules in the solvation shell of both types of ions show only weak packing and orientational ordering. These solvation characteristics are caused by the large size, charge delocalization, and irregular shape (in the case of TEA^+ cation) of the ions. Near neutral electrodes, the double-layer structures in the organic electrolyte exhibit a comprehensive organization: the solvent shows strong layering and orientational ordering, ions are significantly contact-adsorbed on the electrode, and alternating layers of cations/anions penetrate *ca.* 1.1 nm into the bulk electrolyte. The significant contact adsorption of ions and the alternating layering of cation/anion are new features found for EDLs in organic electrolytes. These features essentially originate from the fact that van

der Waals interactions between organic ions and the electrode are strong and the partial desolvation of these ions occurs easily, as a result of the large size of the organic ions. Near charged electrodes, distinct counter-ion concentration peaks form, and the ion distribution cannot be described by the Helmholtz model or the Helmholtz + Poisson−Boltzmann model. This is because the number of counter-ions adsorbed on the electrode exceeds the number of electrons on the electrode, and the electrode is over-screened in parts of the EDL. The computed capacitances of the EDLs are in good agreement with that inferred from experimental measurements. Both the rotations (ACN only) and translations of interfacial ACN and ions are found to slow down as the electrode becomes electrified. We also observed an asymmetrical dependence of these motions on the sign of the electrode charge. The rotation/diffusion of ACN and the diffusion of ions in the region beyond the first ACN or ion layer differ only slightly from those in the bulk.

Third, we investigated the EDLs in the IL of [BMIM][NO_3] near planar electrodes. MD simulations confirm that a Helmholtz-like interfacial counter-ion layer exists when the electrode charge density is negative or strongly positive, but the counter-ion layer is not well-defined when the electrode charge density is weakly positive. The thickness of the EDL, as inferred from how deep the charge separation and orientational ordering of the ions penetrate into the bulk ILs, is about 1.1 nm. The liquid nature of the IL and the short-range ion−electrode and ion−ion interactions are found to significantly affect the structure of the EDL, particularly at low electrode charge densities. Charge delocalization of the ions is found to influence the mean force experienced by the ions

and, thus, can play an important role in shaping the EDL structure. The differential capacitance of the EDLs is found to be nearly constant under negative electrode polarization but increases dramatically with the potential under positive electrode polarization. We showed that the differential capacitance is a quantitative measure of the response of the EDL structure to a change in electrode charge density. It is found that the $[NO_3]^-$ ion dominates the response of EDL structure to the change in electrode charge under both positive and negative electrode polarization, which is qualitatively different from that in aqueous electrolytes. Detailed analysis indicated that the cation−anion correlations and the strong adsorption of $BMIM^+$ ions on the electrode are responsible for the capacitance−potential correlation.

Finally, we studied the effects of ion size and electrode curvature on the EDLs in ILs of [BMIM][Cl] and [BMIM][PF_6]. The results presented three key characteristics of such EDLs:

1. The sizes of the counter-ion and co-ion affect the ion distribution and orientational structure of EDLs.
2. The EDL capacitances near both planar and cylindrical electrodes are found to follow the order: [BMIM][Cl] (near the positive electrode) > [BMIM][PF_6] (near the positive electrode) ≈ [BMIM][Cl] (near the negative electrode) ≈ [BMIM][PF_6] (near the negative electrode).
3. The EDL capacitance is found to increase as the electrode curvature increases.

We can fit the capacitance data well to the Helmholtz model and the recently proposed xEDCC model when the EDL thickness is properly parameterized, even though

key features of the EDLs in ILs are not accounted for in these models. To improve the existing models, we proposed an MILO model for the EDLs in ILs that takes into account two critical features of such EDLs, i.e., alternating layering of counter-ions/co-ions and charge overscreening. The capacitance computed from the MILO model agrees well with the MD prediction. Although some input parameters of the MILO model must be obtained from MD simulations, the MILO model provides a new framework for understanding many important aspects of EDLs in ILs (e.g., the variation of EDL capacitance with the electrode potential) that are difficult to interpret in the classical EDL models and experiments.

REFERENCES AND NOTES

[1] US Department of Energy, Basic research needs for electrical energy storage: report of the basic energy sciences workshop on electrical energy storage, 2007.

[2] Conway, B. E., *Electrochemical Supercapacitors: Scientific Fundamentals and Technological Applications*. Kluwer Academic/Plenum Publishers: New York, **1999**.

[3] Abruna, H. D.; Kiya, Y.; Henderson, J. C. Batteries and electrochemical capacitors. *Physics Today*, **2008**, 61 (12), 43-47.

[4] Christen, T.; Ohler, C. Optimizing energy storage devices using Ragone plots. *Journal of Power Sources*, **2002**, 110 (1), 107-116.

[5] Ue, M.; Takeda, M.; Takahashi, T.; Takehara, M. Ionic liquids with low melting points and their application to double-layer capacitor electrolytes. *Electrochemical and Solid State Letters*, **2002**, 5 (6), A119-A121.

[6] Nanjundiah, C.; McDevitt, S. F.; Koch, V. R. Differential capacitance measurements in solvent-free ionic liquids at Hg and C interfaces. *Journal of The Electrochemical Society*, **1997**, 144 (10), 3392-3397.

[7] Miller, J. R.; Simon, P. Materials science: Electrochemical capacitors for energy management. *Science*, **2008**, 321 (5889), 651-652.

[8] Simon, P.; Gogotsi, Y. Materials for electrochemical capacitors. *Nature Materials*, **2008**, 7 (11), 845-854.

[9] Zhang, L. L.; Zhao, X. S. Carbon-based materials as supercapacitor electrodes. *Chemical Society Reviews*, **2009**, 38 (9), 2520-2531.

[10] Pandolfo, A. G.; Hollenkamp, A. F. Carbon properties and their role in supercapacitors. *Journal of Power Sources*, **2006**, 157 (1), 11-27.

[11] Béguin, F.; Raymundo-Piñero; E.; Frackowiak, E., Electrical double-layer capacitors and pseudocapacitors. In *Carbons for Electrochemical Energy Storage and Conversion Systems*, Béguin, F.; Frackowiak, E., Eds. CRC Press: Boca Raton, FL, 2010; pp 329-375.

[12] Frackowiak, E. Carbon materials for supercapacitor application. *Physical Chemistry Chemical Physics*, **2007**, 9, 1774-1785.

[13] http://www.maxwell.com.

[14] Sing, K. S. W.; Everett, D. H.; Haul, R. A. W.; Moscou, L.; Pierotti, R. A.; Rouquerol, J.; Siemieniewska, T. Reporting physisorption data for gas/solid systems with special reference to the determination of surface area and porosity. *Pure and Applied Chemistry*, **1985**, 57 (4), 603-619.

[15] Huang, J.; Sumpter, B. G.; Meunier, V. A universal model for nanoporous carbon supercapacitors applicable to diverse pore regimes, carbon materials, and electrolytes. *Chemistry - A European Journal*, **2008**, 14 (22), 6614-6626.

[16] Lota, G.; Centeno, T. A.; Frackowiak, E.; Stoeckli, F. Improvement of the structural and chemical properties of a commercial activated carbon for its application in electrochemical capacitors. *Electrochimica Acta*, **2008**, 53 (5), 2210-2216.

[17] Ohno, H., *Electrochemical Aspects of Ionic Liquids*. Wiley-Interscience: New York, **2005**.

[18] Hiemenz, P. C.; Rajagopalan, R., *Principles of Collioid and Surface Chemistry*. Marcel Dekker, Inc.: New York, **1997**.

[19] Butt, H.-J.; Graf, K.; Kappl, M., *Physics and Chemistry of Interfaces*. WILEY-VCH: Weinheim, **2003**.

[20] Philpott, M. R.; Glosli, J. N.; Zhu, S. B. Molecular dynamics simulation of adsorption in electric double layers. *Surface Science*, **1995**, 335 (C), 422-431.

[21] Spohr, E. Molecular simulation of the electrochemical double layer. *Electrochimica Acta*, **1999**, 44 (11), 1697-1705.

[22] Dimitrov, D. I.; Raev, N. D.; Semerdzhiev, K. I. Molecular dynamics simulations of the electrical double layer at 1 M potassium halide solution/Hg electrode interfaces. *Physical Chemistry Chemical Physics*, **2001**, 3 (3), 448 - 452.

[23] Cagle, C.; Feng, G.; Qiao, R.; Huang, J.; Sumpter, B.; Meunier, V. Structure and charging kinetics of electrical double layers at large electrode voltages. *Microfluidics and Nanofluidics*, **2010**, 8 (5), 703-708.

[24] de Andrade, J.; Boes, E. S.; Stassen, H. Computational study of room temperature molten salts composed by 1-Alkyl-3-methylimidazolium cations-force-field proposal and validation. *The Journal of Physical Chemistry B*, **2002**, 106 (51), 13344-13351.

[25] Glosli, J. N.; Philpott, M. R. Molecular dynamics simulation of adsorption of ions from aqueous media onto charged electrodes. *The Journal of Chemical Physics*, **1992**, 96 (9), 6962-6969.

[26] Rajamani, S.; Ghosh, T.; Garde, S. Size dependent ion hydration, its asymmetry, and convergence to macroscopic behavior. *Journal of Chemical Physics*, **2004**, 120 (9), 4457-4466.

[27] Cui, S. T.; Cochran, H. D. Molecular dynamics simulation of interfacial electrolyte behaviors in nanoscale cylindrical pores. *Journal of Chemical Physics*, **2002**, 117 (12), 5850-5854.

[28] Qiao, R.; Aluru, N. R. Atomistic simulation of KCl transport in charged silicon nanochannels: Interfacial effects. *Colloids and Surfaces A: Physicochemical and Engineering Aspects*, **2005**, 267 (1-3), 103-109.

[29] Israelachvili, J. N., *Intermolecular and Surface Forces*. 2nd ed.; Academic Press: New York, **1992**.

[30] Bard, A. J.; Faulkner, L. R., *Electrochemical Methods: Fundamentals and Applications*. 2nd ed.; John Wiley & Sons: New York, **2001**.

[31] Freund, J. B. Electro-osmosis in a nanometer-scale channel studied by atomistic simulation. *Journal of Chemical Physics*, **2002**, 116 (5), 2194-2200.

[32] Qiao, R.; Aluru, N. R. Ion concentrations and velocity profiles in nanochannel electroosmotic flows. *Journal of Chemical Physics*, **2003**, 118 (10), 4692-4701.

[33] Dufrêche, J. F.; Marry, V.; Malíková, N.; Turq, P. Molecular hydrodynamics for electro-osmosis in clays: from Kubo to Smoluchowski. *Journal of Molecular Liquids*, **2005**, 118 (1-3), 145-153.

[34] Wang, M.; Liu, J.; Chen, S. Similarity of electroosmotic flows in nanochannels. *Molecular Simulation*, **2007**, 33 (3), 239-244.

[35] Chen, Y.; Ni, Z.; Wang, G.; Xu, D.; Li, D. Electroosmotic flow in nanotubes with high surface charge densities. *Nano Letters*, **2008**, 8 (1), 42-48.

[36] Yang, K. L.; Yiacoumi, S.; Tsouris, C. Monte Carlo simulations of electrical double-layer formation in nanopores. *Journal of Chemical Physics*, **2002**, 117 (18), 8499-8507.

[37] Shao, Q.; Zhou, J.; Lu, L.; Lu, X.; Zhu, Y.; Jiang, S. Anomalous hydration shell order of Na^+ and K^+ inside carbon nanotubes. *Nano Letters*, **2009**, 9 (3), 989-994.

[38] Song, C.; Corry, B. Intrinsic ion selectivity of narrow hydrophobic pores. *The Journal of Physical Chemistry B*, **2009**, 113 (21), 7642-7649.

[39] Kurzweil, P.; Chwistek, M. Electrochemical stability of organic electrolytes in supercapacitors: Spectroscopy and gas analysis of decomposition products. *Journal of Power Sources*, **2008**, 176 (2), 555-567.

[40] Nicotera, I.; McLachlan, G. D.; Bennett, G. D.; Plitz, I.; Badway, F.; Amatucci, G. G.; Greenbaum, S. G. Solid-state NMR characterization of electrolyte breakdown products in nonaqueous asymmetric hybrid supercapacitors. *Electrochemical and Solid-State Letters*, **2007**, 10 (1), A5-A8.

[41] Ding, M. S.; Xu, K.; Zheng, J. P.; Jow, T. R. γ-butyrolactone-acetonitrile solution of triethylmethylammonium tetrafluoroborate as an electrolyte for double-layer capacitors. *Journal of Power Sources*, **2004**, 138 (1-2), 340-350.

[42] Xu, K.; Ding, S. P.; Jow, T. R. Toward reliable values of electrochemical stability limits for electrolytes. *Journal of The Electrochemical Society*, **1999**, 146 (11), 4172-4178.

[43] Ue, M.; Ida, K.; Mori, S. Electrochemical properties of organic liquid electrolytes based on quaternary onium salts for electrical double-layer capacitors. *Journal of The Electrochemical Society*, **1994**, 141 (11), 2989-2996.

[44] Lust, E. J.; Lust, K. K.; Janes, A. A. J. Influence of the crystallographic structure of the electrode surface on the structure of the electrical double-layer and adsorption of organic-molecules. *Russian Journal of Electrochemistry* **1995**, 31 (8), 807-821.

[45] Lee, S. I.; Saito, K.; Kanehashi, K.; Hatakeyama, M.; Mitani, S.; Yoon, S. H.; Korai, Y.; Mochida, I. 11B NMR study of the BF_4^- anion in activated carbons at various stages of charge of EDLCs in organic electrolyte. *Carbon*, **2006**, 44 (12), 2578-2586.

[46] Yang, L.; Fishbine, B. H.; Migliori, A.; Pratt, L. R. Molecular simulation of electric double-layer capacitors based on carbon nanotube forests. *Journal of the American Chemical Society*, **2009**, 131 (34), 12373-12376.

[47] Kosmulski, M.; Tendaj, B. Low-temperature ionic liquids - a laboratory curiosity or technological revolution? Part 1 Physical and chemical properties. *Przemysl Chemiczny*, **2001**, 80 (7), 280-285.

[48] McEwen, A. B.; Ngo, H. L.; LeCompte, K.; Goldman, J. L. Electrochemical properties of imidazolium salt electrolytes for electrochemical capacitor applications. *Journal of The Electrochemical Society*, **1999**, 146 (5), 1687-1695.

[49] Welton, T. Room-temperature ionic liquids. Solvents for synthesis and catalysis. *Chemical Reviews*, **1999**, 99 (8), 2071-2083.

[50] Kornyshev, A. A. Double-Layer in ionic liquids: Paradigm change? *The Journal of Physical Chemistry B*, **2007**, 111 (20), 5545-5557.

[51] Oldham, K. B. A Gouy-Chapman-Stern model of the double layer at a (metal)/(ionic liquid) interface. *Journal of Electroanalytical Chemistry*, **2008**, 613 (2), 131-138.

[52] Baldelli, S. Surface structure at the ionic liquid-electrified metal interface. *Accounts of Chemical Research*, **2008**, 41 (3), 421-431.

[53] Baldelli, S. Probing electric fields at the ionic liquid-electrode interface using sum frequency generation spectroscopy and electrochemistry. *Journal of Physical Chemistry B*, **2005**, 109 (27), 13049-13051.

[54] Lockett, V.; Sedev, R.; Ralston, J.; Horne, M.; Rodopoulos, T. Differential capacitance of the electrical double layer in imidazolium-based ionic liquids: Influence of potential, cation size, and temperature. *The Journal of Physical Chemistry C*, **2008**, 112 (19), 7486-7495.

[55] Alam, M. T.; Islam, M. M.; Okajima, T.; Ohsaka, T. Measurements of differential capacitance at mercury/room-temperature ionic liquids interfaces. *The Journal of Physical Chemistry C*, **2007**, 111 (49), 18326-18333.

[56] Alam, M. T.; Mominul Islam, M.; Okajima, T.; Ohsaka, T. Measurements of differential capacitance in room temperature ionic liquid at mercury, glassy carbon and gold electrode interfaces. *Electrochemistry Communications*, **2007**, 9 (9), 2370-2374.

[57] Pinilla, C.; Del Pópolo, M. G.; Kohanoff, J.; Lynden-Bell, R. M. Polarization relaxation in an ionic liquid confined between electrified walls. *Journal of Physical Chemistry B*, **2007**, 111 (18), 4877-4884.

[58] Fedorov, M. V.; Kornyshev, A. A. Ionic liquid near a charged wall: Structure and capacitance of electrical double layer. *Journal of Physical Chemistry B*, **2008**, 112 (38), 11868-11872.

[59] Islam, M. M.; Alam, M. T.; Okajima, T.; Ohsaka, T. Electrical double layer structure in ionic liquids: An understanding of the unusual capacitance−potential curve at a nonmetallic electrode. *The Journal of Physical Chemistry C*, **2009**, 113 (9), 3386-3389.

[60] Sha, M.; Zhang, F.; Wu, G.; Fang, H.; Wang, C.; Chen, S.; Zhang, Y.; Hu, J. Ordering layers of [bmim][PF_6] ionic liquid on graphite surfaces: Molecular dynamics simulation. *Journal of Chemical Physics*, **2008**, 128 (13), article number 134504.

[61] Bhargava, B. L.; Balasubramanian, S. Layering at an ionic liquid-vapor interface: a molecular dynamics simulation study of [bmim][PF_6]. *Journal of the American Chemical Society*, **2006**, 128 (31), 10073-10078.

[62] Feng, G.; Zhang, J. S.; Qiao, R. Microstructure and capacitance of the electrical double layers at the interface of ionic liquids and planar electrodes. *The Journal of Physical Chemistry C*, **2009**, 113 (11), 4549-4559.

[63] Kornyshev, A. A.; Leikin, S.; Sutmann, G. "Overscreening" in a polar liquid as a result of coupling between polarization and density fluctuations. *Electrochimica Acta*, **1997**, 42 (5), 849-865.

[64] Fedorov, M. V.; Kornyshev, A. A. Towards understanding the structure and capacitance of electrical double layer in ionic liquids. *Electrochimica Acta*, **2008**, 53 (23), 6835-6840.

[65] Frenkel, D.; Smit, B., *Understanding Molecular Simulation*. Academic Press: California, **2002**.

[66] Allen, M. P., Introduction to molecular dynamics simulation. In *Computational Soft Matter: From Synthetic Polymers to Proteins*, Attig, N.; Binder, K.; Grubmüller, H.; Kremer, K., Eds. John von Neumann Institute for Computing, Jülich, NIC Series: 2004; Vol. 23, pp 1-28.

[67] Allen, M. P.; Tildesley, D. J., *Computer Simulation Of Liquids*. Oxford University Press: New York, **1987**

[68] Lindahl, E.; Hess, B.; van der Spoel, D. GROMACS 3.0: A package for molecular simulation and trajectory analysis. *Journal of Molecular Modeling*, **2001**, 7 (8), 306-317.

[69] Meunier, V.; Kalinin, S. V.; Shin, J.; Baddorf, A. P.; Harrison, R. J. Quantitative Analysis of Electronic Properties of Carbon Nanotubes by Scanning Probe Microscopy: From Atomic to Mesoscopic Length Scales. *Physical Review Letters*, **2004**, 93 (24), article number 246801.

[70] Lee, S. H.; Rasaiah, J. C. Molecular Dynamics Simulation of Ion Mobility. 2. Alkali Metal and Halide Ions Using the SPC/E Model for Water at 25 ^{o}C. *The Journal of Physical Chemistry*, **1996**, 100 (4), 1420-1425.

[71] Cornell, W. D.; Cieplak, P.; Bayly, C. I.; Gould, I. R.; Merz, K. M.; Ferguson, D. M.; Spellmeyer, D. C.; Fox, T.; Caldwell, J. W.; Kollman, P. A. A second generation force field for the simulation of proteins, nucleic acids, and organic molecules. *Journal of the American Chemical Society*, **1995**, 117 (19), 5179-5197.

[72] We also investigated the ion distribution in slit pores with the same widths studied here but with surface charge densities of ±0.014 and ±0.083 C/m^2. The ion distribution across these slit pores shows the same trend as reported here.

[73] If the electronic degree of freedom of the slit wall is also accounted for, additional factors will be at play. However, this is outside the scope of this work.

[74] As pointed out in Ref. 29, the electrostatic ion-slit wall interactions play no role in determining the ion distribution when co-ions are completely rejected from the slit pore.

[75] In principle, the interactions between the ion's hydration water and pore wall atoms should also be considered. However, these interactions are not detailed here because such interactions are much weaker than the water-water interactions and show little change as ion moves across the micro-slits considered here.

[76] Lo, W. Y.; Chan, K. Y.; Lee, M.; Mok, K. L. Molecular simulation of electrolytes in nanopores. *Journal of Electroanalytical Chemistry*, **1998**, 450 (2), 265-272.

[77] Lamperski, S.; Outhwaite, C. W. A non-primitive model for the electrode | electrolyte interface based on the Percus-Yevick theory. Analysis of the different molecular sizes, ion valences and electrolyte concentrations. *Journal of Electroanalytical Chemistry*, **1999**, 460 (1-2), 135-143.

[78] Burak, Y.; Andelman, D. Hydration interactions: Aqueous solvent effects in electric double layers. *Physical Review E*, **2000**, 62 (4), 5296.

[79] The potential of mean force (PMF) of a K^+ ion located at the peak adjacent to the slit was found to be 2.04 k_BT (k_B is the Boltzmann constant, T = 300 K) lower than that at the slit center. Since this PMF difference is larger than k_BT, the entropic effects alone are unlikely to cause K^+ ions to accumulate in the peaks adjacent to the slit wall.

[80] Frese, K. W. Calculation of Gibbs hydration energy with the ion-dielectric sphere model. *The Journal of Physical Chemistry*, **1989**, 93 (15), 5911-5916.

[81] Palmer, L. S.; Cunliffe, A.; Hough, J. M. Dielectric constant of water films. *Nature*, **1952**, 170 (4332), 796.

[82] Dzubiella, J.; Hansen, J. P. Electric-field-controlled water and ion permeation of a hydrophobic nanopore. *Journal of Chemical Physics*, **2005**, 122 (23), 1-14.

[83] Marcus, Y.; Rashin, A. A simple empirical model describing the thermodynamics of hydration of ions of widely varying charges, sizes, and shapes. *Biophysical Chemistry*, **1994**, 51 (2-3), 111-127.

[84] Chmiola, J.; Yushin, G.; Gogotsi, Y.; Portet, C.; Simon, P.; Taberna, P. L. Anomalous increase in carbon at pore sizes less than 1 nanometer. *Science*, **2006**, 313 (5794), 1760-1763.

[85] Lang, N. D.; Kohn, W. Theory of metal surfaces: Work function. *Physical Review B*, **1971**, 3 (4), 1215-1223.

[86] Raghunathan, A. V.; Aluru, N. R. Self-consistent molecular dynamics formulation for electric-field-mediated electrolyte transport through nanochannels. *Physical Review E*, **2007**, 76 (1), article number 011202.

[87] Portet, C.; Yang, Z.; Korenblit, Y.; Gogotsi, Y.; Mokaya, R.; Yushin, G. Electrical double-layer capacitance of zeolite-templated carbon in organic electrolyte. *Journal of The Electrochemical Society*, **2009**, 156 (1), A1-A6.

[88] Nishihara, H.; Itoi, H.; Kogure, T.; Hou, P. X.; Touhara, H.; Okino, F.; Kyotani, T. Investigation of the ion storage/transfer behavior in an electrical double- layer capacitor by using ordered microporous carbons as model materials. *Chemistry - A European Journal*, **2009**, 15 (21), 5355-5363.

[89] Rufford, T. E.; Hulicova-Jurcakova, D.; Fiset, E.; Zhu, Z.; Lu, G. Q. Double-layer capacitance of waste coffee ground activated carbons in an organic electrolyte. *Electrochemistry Communications*, **2009**, 11 (5), 974-977.

[90] Ruch, P. W.; Kötz, R.; Wokaun, A. Electrochemical characterization of single-walled carbon nanotubes for electrochemical double layer capacitors using non-aqueous electrolyte. *Electrochimica Acta*, **2009**, 54 (19), 4451-4458.

[91] Fernández, J. A.; Arulepp, M.; Leis, J.; Stoeckli, F.; Centeno, T. A. EDLC performance of carbide-derived carbons in aprotic and acidic electrolytes. *Electrochimica Acta*, **2008**, 53 (24), 7111-7116.

[92] Jänes, A.; Lust, E. Electrochemical characteristics of nanoporous carbide-derived carbon materials in various nonaqueous electrolyte solutions. *Journal of The Electrochemical Society*, **2006**, 153 (1), A113-A116.

[93] Wang, J.; Wolf, R. M.; Caldwell, J. W.; Kollman, P. A.; Case, D. A. Development and testing of a general amber force field. *Journal of Computational Chemistry*, **2004**, 25 (9), 1157-1174.

[94] Luzhkov, V. B.; Österberg, F.; Acharya, P.; Chattopadhyaya, J.; Åqvist, J. Computational and NMR study of quaternary ammonium ion conformations in solution. *Physical Chemistry Chemical Physics*, **2002**, 4 (19), 4640-4647.

[95] Wu, X.; Liu, Z.; Huang, S.; Wang, W. Molecular dynamics simulation of room-temperature ionic liquid mixture of [bmim][BF_4] and acetonitrile by a refined force field. *Physical Chemistry Chemical Physics*, **2005**, 7, 2771-2779.

[96] Lide, D. R.; Haynes, W. M. M., *CRC Handbook of Chemistry and Physics, 90th ed., Internet Version 2010*. CRC Press: Boca Raton, FL, **2009**.

[97] Yeh, I.-C.; Berkowitz, M. L. Ewald summation for systems with slab geometry. *The Journal of Chemical Physics*, **1999**, 111 (7), 3155-3162.

[98] Hess, B.; Bekker, H.; Berendsen, H. J. C.; Fraaije, J. G. E. M. LINCS: A linear constraint solver for molecular simulations. *Journal of Computational Chemistry*, **1997**, 18 (12), 1463-1472.

[99] Ue, M. Mobility and ionic association of lithium and quaternary ammonium salts in propylene carbonate and γ-butyrolactone. *Journal of The Electrochemical Society*, **1994**, 141 (12), 3336-3342.

[100] Jenkins, H. D. B.; Thakur, K. P. Reappraisal of thermochemical radii for complex ions. *Journal of Chemical Education*, **1979**, 56 (9), 576-577.

[101] Chmiola, J.; Largeot, C.; Taberna, P. L.; Simon, P.; Gogotsi, Y. Desolvation of ions in subnanometer pores and its effect on capacitance and double-layer theory. *Angewandte Chemie - International Edition*, **2008**, 47 (18), 3392-3395.

[102] Greberg, H.; Kjellander, R. Charge inversion in electric double layers and effects of different sizes for counterions and colons. *Journal of Chemical Physics*, **1998**, 108 (7), 2940-2953.

[103] Maroncelli, M. Computer simulations of solvation dynamics in acetonitrile. *The Journal of Chemical Physics*, **1991**, 94 (3), 2084-2103.

[104] Lynden-Bell, R. M.; Del Pópolo, M. G.; Youngs, T. G. A.; Kohanoff, J.; Hanke, C. G.; Harper, J. B.; Pinilla, C. C. Simulations of ionic liquids, solutions, and surfaces. *Accounts of Chemical Research*, **2007**, 40 (11), 1138-1145.

[105] Markovits, A.; Minot, C. Theoretical study of the acetonitrile flip-flop with the electric field orientation: Adsorption on a Pt(111) electrode surface. *Catalysis Letters*, **2003**, 91 (3-4), 225-234.

[106] Baldelli, S.; Mailhot, G.; Ross, P.; Shen, Y. R.; Somorjai, G. A. Potential dependent orientation of acetonitrile on platinum (111) electrode surface studied

by sum frequency generation. *Journal of Physical Chemistry B*, **2001**, 105 (3), 654-662.

[107] Schiffmann, F.; Hutter, J.; VandeVondele, J. Atomistic simulations of a solid/liquid interface: a combined force field and first principles approach to the structure and dynamics of acetonitrile near an anatase surface. *Journal of Physics: Condensed Matter*, **2008**, 20 (6), 064206.

[108] Meunier, V.; Kalinin, S. V.; Sumpter, B. G. Nonvolatile memory elements based on the intercalation of organic molecules inside carbon nanotubes. *Physical Review Letters*, **2007**, 98 (5), article number 056401

[109] Meunier, V.; Sumpter, B. G. Amphoteric doping of carbon nanotubes by encapsulation of organic molecules: Electronic properties and quantum conductance. *Journal of Chemical Physics*, **2005**, 123 (2), article number 024705.

[110] Schmickler, W.; Henderson, D. New models for the structure of the electrochemical interface. *Progress in Surface Science*, **1986**, 22 (4), 323-419.

[111] Halley, J. W. Studies of the interdependence of electronic and atomic dynamics and structure at the electrode-electrolyte interface. *Electrochimica Acta*, **1996**, 41 (14 SPEC. ISS.), 2229-2251.

[112] Pozhar, L. A., *Transport Theory of Inhomogeneous Fluids*. World Scientific Press: Singapore, **1994**.

[113] Feng, G.; Huang, J.; Sumpter, B. G.; Meunier, V.; Qiao, R. Structure and dynamics of electrical double layers in organic electrolytes. *Physical Chemistry Chemical Physics*, **2010**, 12, 5468-5479.

[114] Reed, S. K.; Lanning, O. J.; Madden, P. A. Electrochemical interface between an ionic liquid and a model metallic electrode. *Journal of Chemical Physics*, **2007**, 126 (8), article number 084704.

[115] Esnouf, R. M.; Smith, A. C. D.; Grout, P. J. The computer simulation of the metal-molten salt interface. *Philosophical Magazine A,* **1988**, 58 (1), 27 - 35.

[116] Lanning, O. J.; Madden, P. A. Screening at a charged surface by a molten salt. *Journal of Physical Chemistry B*, **2004**, 108 (30), 11069-11072.

[117] Heyes, D. M.; Clarke, J. H. R. Computer simulation of molten-salt interphases. Effect of a rigid boundary and an applied electric field. *Journal of the Chemical Society, Faraday Transactions 2: Molecular and Chemical Physics*, **1981**, 77 (7), 1089-1100.

[118] Fukushima, T.; Kosaka, A.; Ishimura, Y.; Yamamoto, T.; Takigawa, T.; Ishii, N.; Aida, T. Molecular ordering of organic molten salts triggered by single-walled carbon nanotubes. *Science*, **2003**, 300 (5628), 2072-2074.

[119] Fukushima, T.; Aida, T. Ionic liquids for soft functional materials with carbon nanotubes. *Chemistry - A European Journal*, **2007**, 13 (18), 5048-5058.

[120] Pinilla, C.; Del Pópolo, M. G.; Lynden-Bell, R. M.; Kohanoff, J. Structure and dynamics of a confined ionic liquid. Topics of relevance to dye-sensitized solar cells. *Journal of Physical Chemistry B*, **2005**, 109 (38), 17922-17927.

[121] Luo, H.; Yu, M. Y. A note on charged interfaces. *Physica Scripta*, **2006**, 74 (6), 670-672.

[122] Micaelo, N. M.; Baptista, A. M.; Soares, C. M. Parametrization of 1-butyl-3-methylimidazolium hexafluorophosphate/nitrate ionic liquid for the GROMOS force field. *Journal of Physical Chemistry B*, **2006**, 110 (29), 14444-14451.

[123] Berthod, A.; Kozak, J. J.; Ding, J. L.; Anderson, J. L.; Armstrong, D. W. Ionic liquid-alkane association in dilute solutions. *Theoretical Chemistry Accounts*, **2007**, 117 (1), 127-135.

[124] Canongia Lopes, J. N.; Deschamps, J.; Padua, A. A. H. Modeling ionic liquids using a systematic all-atom force field. *The Journal of Physical Chemistry B*, **2004**, 108 (6), 2038-2047.

[125] Wang, S.; Li, S.; Cao, Z.; Yan, T. Molecular dynamic simulations of ionic liquids at graphite surface. *The Journal of Physical Chemistry C*, **2010**, 114 (2), 990-995.

[126] Kislenko, S. A.; Samoylov, I. S.; Amirov, R. H. Molecular dynamics simulation of the electrochemical interface between a graphite surface and the ionic liquid [BMIM][PF_6]. *Physical Chemistry Chemical Physics*, **2009**, 11 (27), 5584-5590.

[127] Communications with our collaborators, Dr. Huang, J.; Dr. Sumpter, B. G.; and Dr. Meunier, V.

[128] Dong, K.; Zhang, S.; Wang, D.; Yao, X. Hydrogen Bonds in Imidazolium Ionic Liquids. *The Journal of Physical Chemistry A*, **2006**, 110 (31), 9775-9782.

[129] Raabe, G.; Köhler, J. Thermodynamical and structural properties of imidazolium based ionic liquids from molecular simulation. *The Journal of Chemical Physics*, **2008**, 128 (15), article number 154509.

[130] Huang, J.; Sumpter, B. G.; Meunier, V.; Yushin, G.; Portet, C.; Gogotsi, Y. *Journal of Materials Research*, **2010**, in press.

[131] Weingärtner, H.; Sasisanker, P.; Daguenet, C.; Dyson, P. J.; Krossing, I.; Slattery, J. M.; Schubert, T. The dielectric response of room-temperature ionic liquids: Effect of cation variation. *The Journal of Physical Chemistry B*, **2007**, 111 (18), 4775-4780.

[132] Ballenegger, V.; Hansen, J.-P. Dielectric permittivity profiles of confined polar fluids. *Journal of Chemical Physics*, **2005**, 122 (11), article number 114711.

[133] Singh, T.; Kumar, A. Static dielectric constant of room temperature ionic liquids: Internal pressure and cohesive energy density approach. *The Journal of Physical Chemistry B*, **2008**, 112 (41), 12968-12972.

[134] Conway, B. E.; Bockris, J. O. M.; Ammar, I. A. The dielectric constant of the solution in the diffuse and Helmholtz double layers at a charged interface in aqueous solution. *Transactions of the Faraday Society*, **1951**, 47, 756-766.

[135] Macdonald, J. R.; Barlow, C. A. Theory of double-layer differential capacitance in electrolytes. *Journal of Chemical Physics*, **1962**, 36 (11), 3062-3080.

[136] Teschke, O.; de Souza, E. F. Dielectric exchange: The key repulsive or attractive transient forces between atomic force microscope tips and charged surfaces. *Applied Physics Letters*, **1999**, 74 (12), 1755-1757.

[137] Feng, G.; Qiao, R., unpublished data.